Transport and dynamics of low-dimensional quantum spin systems

Von der Fakultät für Elektrotechnik, Informationstechnik, Physik

der Technischen Universität Carolo-Wilhelmina
zu Braunschweig
zur Erlangung des Grades eines

Doktors der Naturwissenschaften
(Dr. rer. nat.)

genehmigte
DISSERTATION

von
Yousef Rahnavard
aus
Shahrekord im Iran

eingereicht am: 23.06.2014

Disputation am: 29.07.2014

1. Referent: Prof. Dr. Wolfram Brenig

2. Referent: Prof. Dr. Patrik Recher

Druckjahr: 2014

Vorveröffentlichung der Dissertation

Teilergebnisse aus dieser Arbeit wurden mit Genehmigung der Fakultät für Elektrotechnik, Informationstechnik, Physik, vertreten durch den Mentor der Arbeit, in folgenden Beiträgen vorab veröffentlicht:

Publikationen

- Y. Rahnavard, and W. Brenig, *Statics and dynamics of anisotropic spin=1 chain in magnetic fields*, in preparation.

- Y. Rahnavard, and W. Brenig, *Spin diffusion in the XXZ chain: a quantum Monte-Carlo study*, in preparation.

- M. Arlego, W. Brenig, Y. Rahnavard, B. Willenberg, H. D. Rosales, and G.Rossini, *Quantum phases of a frustrated four-leg spin tube*, Phys. Rev. B. **87**, 014412 (2013).

Tagungsbeiträge

- Y. Rahnavard, and W. Brenig, *Using quantum Monte-Carlo for dynamical spin-conductivities*, 4th LOTHERM project meeting, 27.06.-29.06.2011, Dresden (talk and poster).

- Y. Rahnavard, and W. Brenig, *Study of parameters of dynamical spin-conductivity*, theory seminar of the research unit 912 of the German Science Foundation (DFG), 23.08.2011, Braunschweig (talk).

- Y. Rahnavard, and W. Brenig, *Spin diffusion in the Heisenberg chain: a quantum Monte Carlo*, 5th LOTHERM project meeting, 09.01.-10.01.2012, Paris (talk).

- Y. Rahnavard, B. Willenberg, and W. Brenig, *Spin diffusion in the Heisenberg chain: a quantum Monte Carlo study*, DPG Frühjahrstagung, 25.03.-30.03.2011, Berlin (poster).

- Y. Rahnavard, B. Willenberg, and W. Brenig, *Magnetism of four spin tube: results from quantum Monte Carlo*, 6th LOTHERM project meeting, 07.08.-08.08.2012, Ljubljana (talk).

- Y. Rahnavard, R. Steinigeweg, and W. Brenig, *Spin diffusion in the Heisenberg chain*, LOTHERM summer school, 04.08.-04.08.2012, Ljubljana (poster).

- M. Arlego, W. Brenig, Y. Rahnavard, B. Willenberg, H. D. Rosales, and G.Rossini, *Quantum phases of a frustrated four-leg spin tube*, DPG Frühjahrstagung, 10.03.-15.03.2013, Regensburg (poster).

- Y. Rahnavard, and W. Brenig, *Statics and dynamics of anisotropic spin-1 chains in magnetic fields*, 7th LOTHERM project meeting, 25.04.-26.04.2013, Nicosia (talk).

- Y. Rahnavard, and W. Brenig, *Dynamics of one dimensional spin systems: a quantum Monte Carlo approach*, LOTHERM final workshop, 09.09.-13.09.2013, Kolymbari (talk).

- M. Arlego, W. Brenig, Y. Rahnavard, B. Willenberg, H. D. Rosales, and G.Rossini, *Quantum phases of a frustrated four-leg spin tube*, LOTHERM final workshop, 09.09.-13.09.2013, Kolymbari (poster).

I dedicate this thesis to my wife, Vida,
for her constant support and unconditional love.

Contents

List of Figures

Abstract

In this thesis, I use a quantum Monte Carlo (QMC) method based on the stochastic series expansion (SSE) to study transport, quantum phase diagrams, and dynamics of several one- and quasi-one-dimensional spin systems, including spin-1/2 and spin-1 chains, a frustrated four-leg spin tube, and N-leg spin-1/2 ladders.

I establish a diffusive channel for the finite temperature spin transport of the spin-1/2 antiferromagnetic Heisenberg chain. Extensive finite size studies are detailed, allowing to extract the diffusion kernel in the thermodynamic limit. The diffusion is found to exhibit no anomalous exponent, moreover it is shown to survive for finite values of exchange anisotropy and magnetic fields, however with a strong suppression away from the isotropic point and for increasing magnetic fields.

In the case of the spin-1 chain, I obtain the quantum phase diagram and spin dynamics in the combined presence of finite single-ion anisotropies and external magnetic fields. I also prove the existence of magnon modes and multi-particle continua and determine their evolutions as a function of anisotropies and magnetic fields. Moreover, I calculate the magnetic field dependence of the nuclear magnetic relaxation as a function of the single ion anisotropy.

For the quasi-one-dimensional spin system of a frustrated four-leg tube, I investigate the regime of large rung coupling, where QMC is applicable. I evaluate the uniform spin susceptibility and the dynamic structure factor and show that in this regime the spin-tube exhibts a crossover from a gapped effective antiferromagnetic spin-2 chain behavior with massive magnons to a gapless Luttinger liquid phase with spinon excitations.

Finally, I investigate the spin dynamics of N-leg spin-1/2 ladders with spacially isotropic interactions for N=1,..,5. I obtain the low-lying excitations of the spin ladders as a function of the number of legs and show that they exhibt an even-odd oscillation which is consistent with Haldane's conjecture and other known results for the thermodynamics of spin ladders.

Zussammenfassung

In dieser Dissertation verwende ich eine Quanten-Monte-Carlo-Methode (QMC) auf der Grundlage von stochastischer Serienentwicklung für die Untersuchung des Transports, der Quantenphasendiagramme und der Dynamik verschiedener eindimensionaler und quasi-eindimensionaler Spinsysteme. Diese Systeme beinhalten Ketten mit Spinquantenzahl 1/2 oder 1, eine frustrierte vierbeinige Spinröhre und N-beinige Leitern mit Spinquantenzahl 1/2.

Ich weise einen diffusiven Kanal für Spintransport in der antiferromagnetischen Heisenberg-Kette bei endlichen Temperaturen nach. Detaillierte Untersuchungen endlicher Systemgrößen erlauben, den Diffusionskern im thermodynamischen Limes zu bestimmen. Die Diffusion zeigt keinen irregulären Exponenten und ist stabil gegenüber endlichen Werten der Austauschanisotropie und des Magnetfeldes. Sie ist jedoch stark unterdrückt außerhalb des isotropen Punktes und für wachsende Magnetfelder.

Im Fall der Kette mit Spinquantenzahl 1 bestimme ich das Quantenphasendiagramm und die Spindynamik in der simultanen Gegenwart endlicher Einzelionenanisotropien und äußerer Magnetfelder. Ich zeige außerdem die Existenz von Magnonenmoden und Vielteilchenkontinua und bestimme ihre Entwicklung als Funktion von der Anisotropie und des Magnetfeldes. Darüber hinaus berechne ich die Magnetfeldabhängigkeit der Kernspinrelaxation als Funktion der Anisotropie.

Für das quasi-eindimensionale System einer frustrierten vierbeinigen Spinröhre untersuche ich den Bereich starker Sprossenkopplung, in dem die QMC anwendbar ist. Ich berechne die gleichförmige Spinsuszeptibilität und den dynamischen Strukturfaktor. Dadurch zeige ich in diesem Bereich den bergang der Spinröhre von einer i) effektiv antiferromagnetischen Kette mit Spinquantenzahl 2, einem endlichen Energieunterschied zwischen Grundzustand und angeregten Zuständen und massiven Magnonen zu einer ii) Luttingerflüssigkeitsphase ohne dem obigen Energieunterschied und mit Anregungen in Form von Spinonen.

Schließlich untersuche ich die Spindynamik einer N-beinigen Leider mit Spinquantenzahl 1/2 und räumlich isotropen Wechselwirkungen für N=1,..,5. Ich ermittle die niederenergetischen Anregungen der Spinleiter als Funktion von N. Ich zeige, dass diese Anregungen eine Oszillation zwischen gerader und ungerader Platzzahl aufweisen, die konsistent mit Haldanes Vermutung ist und mit anderen bekannten Ergebnissen über die Thermodynamik von Spinleitern.

1. Introduction

When the scale U of the Coulomb interaction between electrons in condensed matter systems gets comparable to or larger than the energy scale t of their kinetic energy, such systems are called strongly correlated. In this field, many novel phenomena have been discovered which are absent in weakly correlated materials, such as high temperature superconductivity, Mott insulators and the fractional quantum Hall effect. It is probably one of the most active fields in solid state physics. Both theory and experiment have contributed equally strongly to these phenomena. This pertains e.g. to the discovery of spinons as excitations of spin-1/2 antiferromagnetic chains [1–3], experimental realizations [4, 5] of the Haldane conjecture [6] on the difference between excitations of chains with integer versus half-integer spins, or the upsurge of theories about Mott insulators in the context of high temperature superconductors.

Lattice models play an important role in the description of strongly correlated systems. Among them the Hubbard model [7] is a prominent one

$$H = \sum_{\langle i,j\rangle,\sigma} t_{i,j}(c^\dagger_{i,\sigma}c_{j,\sigma} + c^\dagger_{j,\sigma}c_{i,\sigma}) + U\sum_i n_{i\uparrow}n_{i\downarrow}, \tag{1.1}$$

where the operators $c^\dagger_{i,\sigma}$ and $c_{j,\sigma}$ are the fermionic creation and annihilation operators at sites i, j for electrons of spin σ. The matrix elements $t_{i,j}$ denote the hopping between i, j and U is the interaction energy due to the Coulomb repulsion between two electrons. Here, $n_{i\sigma}$ is the number operator for an electron with spin σ. For the case of one electron per site and in the limit $U \gg t_{i,j}$, this can be projected onto the Heisenberg model [8]

$$H = \sum_{\langle i,j\rangle} J_{i,j}\mathbf{S}_i \cdot \mathbf{S}_j. \tag{1.2}$$

Here, $\mathbf{S}_i = (S^x_i, S^y_i, S^z_i)$ is the spin vector at site i and $J_{i,j} = (t_{i,j})^2/U$ is the (super)exchange coupling constant. While in many cases it is realistic to simplify to only next-nearest neighbor exchange, other effects such as anisotropies and external magnetic fields are of interest

$$H = J\sum_{\langle i,j\rangle}[S^+_iS^-_j + S^-_iS^+_j + \Delta S^z_iS^z_j] + h\sum_i S^z_i + D\sum_i (S^z_i)^2, \tag{1.3}$$

where $S_j^{\pm} = S_j^x \pm iS_j^y$ are the raising and lowering operators and Δ is the exchange anisotropy. The two last terms in the Hamiltonian are respectively the Zeeman term due to an external magnetic field and the single-ion anisotropy term induced by the spin-orbit coupling. This thesis is concerned with theoretical studies of one dimensional versions of such models. While this may seem academic at first site, it is an experimental fact that many real materials exist which can be captured in this way and relate to parts of this thesis as e.g. $KCuF_3$ and Sr_2CuO_3 realized as spin-1/2 antiferromagnetic chains [9, 10], $CsNiCl_3$ and NENP known as spin-1 Heisenberg chains [4, 11], $Cu_2Cl_4{\cdot}D_8C_4SO_2$ which is an example of frustrated four-spin tube [12], and ladder material $SrCu_2O_3$ [13].

From the point of view of magnetism, the sign of J is essential. For ferromagnetic exchange ($J < 0$), the ground state of the Hamiltonian is a simple product state of all S_i^z. For antiferromagnetic J ($J > 0$), the third term in Eq. 1.3 suggests an antiferromagnetic Ising-like alignment of spins, while the first term introduces quantum fluctuations which destroy this alignment. This antagonism is one central aspect of quantum antiferromagnetism. The quantum fluctuations depend sensitively on the size of spin, the dimension and the connectivity of the underlying lattice. They are particularly strong in one dimension for spin-1/2.

From the point of view of interacting electrons, Eq. 1.3 in one dimension also allows for a different interpretation which is due to the fact that in that case, spin degrees of freedom can be mapped onto spinless fermions. The first two terms of Eq. 1.3 then resemble the kinetic energy of these fermions while the third term is an interaction. Obviously the energy scale of the kinetic energy J can be comparable to the energy scale of the interaction, ΔJ, for Δ of the order of one. While non-interacting electrons can be explained using the simple Fermi gas theory, the treatment of interactions can be pursued along various lines of approximations, such as perturbation theory or Landau Fermi liquid theory. Exact treatments of interactions are available only in rare cases. Remarkably such an exact treatment is available for certain parameter ranges of Eq. 1.3 by means of the Bethe ansatz [14], While Landau theory does not require interactions to be small, like in our spin systems mapped to spinless Fermi gases, it breaks down completely in one dimension and therefore can not be used to understand a spin-1/2 Heisenberg chain. In fact the elementary excitations of interacting one-dimensional spinless Fermi gases turn out to be collective density excitations which can be described in the context of the Luttinger liquid theory [15–17]. Spin dynamics in this theory can be understood in terms of deconfined multi spinon excitations which have fermionic character.

From the point of view of theoretical approaches, the study of low dimensional systems has brought up a large variety of analytical methods including different types of Bethe ansatz [18], quantum field theories [19], perturbative approaches such as high order series expansions [20] as well as numerical methods such as exact diagonalization (ED), density

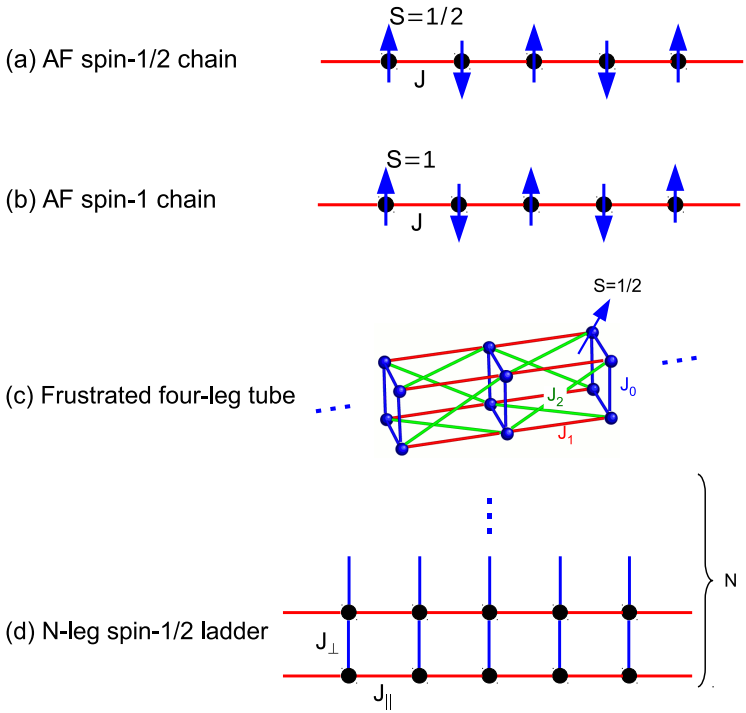

Figure 1.1.: The lattice structure and couplings of the antiferromagnetic (AF) spin-1/2 and spin-1 chains, a frustrated four-leg spin tube, and an N-leg spin ladder.

matrix renormalization group (DMRG) [21] and quantum Monte Carlo (QMC) calculations [22, 23] which have been applied to investigate different aspects of this class of solid state physics. The main results of this thesis have been obtained using a QMC approach, however in some special cases, other analytical and numerical methods have been used to establish the results.

In this thesis, we study transport and spin dynamics in the Heisenberg model for a variety of low-dimensional spin systems for each of which the lattice structure is demonstrated in Fig. 1.1. These comprise the antiferromagnetic spin-1/2 chain, Fig. 1.1(a), the anisotropic spin-1 chain, Fig. 1.1(b), the frustrated four spin tube, Fig. 1.1(c), and finally N-leg spin-1/2 ladders, Fig. 1.1(d). All of these systems differ by essential variables and parameters such as spin size, dimensionality, and ratio of exchange parameters. While for the first

of these models, we are concerned with the finite temperature spin transport and its dependence on different model parameters, for the second one, we study a quantum phase diagram and spin dynamics as a function of single-ion anisotropy and magnetic fields. In addition to spin chains, we are also interested in more complicated and also physically rich low-dimensional systems such as ladders and tubes. Here we confine ourselves to ladders and tubes with spin-1/2 sites that are antiferromagnetically coupled (see Fig. 1.1). Ladders are quantum spin systems consisting of N parallel spin chains which are connected via rung interactions. A ladder of N spin chains is called N-leg ladder. N-leg ladders have been studied using various theoretical and experimental methods for more than two decades [24]. In the study of ladders, many interesting questions have been posed: what happens on the way from one- to two-dimensional systems?, how do low energy properties of ladders depend on the number of legs?, are spin ladders good candidates for high-T_c superconductivity? These questions have been partially solved (see Ref. [24] and references therein), yet there exist many unknown aspects of ladders that need to be addressed. If we apply periodic boundary conditions in the transverse direction of an N-leg ladder, we have a tubelike lattice structure known as the N-leg spin tube. Due to these periodic boundary conditions, the spin tube holds quantum mechanical properties which are unique and different from those of ladders.

The organization of the thesis is as follows. In chapter 2, the general formulation of the quantum Monte Carlo (QMC) method based on a stochastic series expansion (SSE) [22], as well as details of its implementation are given. Then, it is shown how static quantities such as magnetic susceptibilities and correlation functions can be calculated. A key quantity to explore spin dynamics is the dynamical structure factor (DSF) of the system which is defined as a Fourier transform of the time-dependent spin-spin correlation functions. This quantity can also be accessed by the QMC method, however only at imaginary times. In order to access experimentally relevant quantities like inelastic neutron scattering (INS) data or nuclear magnetic resonance (NMR) spectra, such imaginary time results have to be transformed onto the real frequency domain. The way this is done will be discussed in detail for the transverse and longitudinal dynamical structure factors. The key technique in this context is the *maximum entropy method* [25] which will also be described in this chapter. Finally the chapter contains a discussion of how to efficiently estimate and improve the statistical errors of all quantities determined by QMC in this thesis [23].

After representing the methods and the requirements to obtain physical quantities in chapter 2, the main results of the thesis will be discussed in chapters 3, 4, 5 and 6. In chapter 3, we study the finite temperature spin transport of the antiferromagnetic spin-1/2 Heisenberg chain. Many questions on the nature of this transport, e.g. whether it is ballistic or diffusive, are under intense scrutiny. We address this question of spin diffusion by evaluating the dynamical susceptibility of the Heisenberg chain at finite temperature and in the long wavelength limit. This is motivated by the recent works, where a diffusive regime has been suggested for the spin transport of the spin-1/2 Heisenberg chain at finite

temperature using different methods including bosonization, transfer-matrix renormalization group [26, 27] and quantum Monte Carlo [28]. After a short review on relevant results in the literature and after highlighting some aspects currently controversial, we describe the method of treatment, which is a combination of the QMC data and the results form bosonization. This approach has been already used in Ref. [28] in order to calculate the spin current relaxation rate of the Heisenberg chain at the isotropic point. However the results of this paper are only limited to one system-size. We do a finite-size scaling at the isotropic point to study the size dependence. We perform consistency checks of our method by comparing QMC with the spectra from exact diagonalization at system-sizes and temperatures which are accessible to ED. We also check for signatures of possible anomalous diffusion by considering a potential power-law frequency dependence of the diffusion kernel. We go further by applying our approach to the Heisenberg chain subject to finite magnetic fields up to the saturation field and show how to manipulate the current relaxation rate using the magnetic field. Finally, we apply the approach to the anisotropic case, i.e. $0 < \Delta < 1$. As mentioned, for $\Delta = 0$ the system resembles non-interacting spinless fermions, which implies that the relaxation rate must be zero. As Δ is ranged from 0 to 1, we show the behavior of the relaxation rate.

In chapter 4, we study quantum phases and spin dynamics of a spin-1 chain. The main goal in this chapter is to investigate the evolution of the spin dynamics in the simultaneous presence of single-ion anisotropy (D) and external magnetic field (h). To start, we first uncover the quantum phase diagram of the system as a function of h and D. To this end, we study the spin gap of the system in order to distinguish between gapped and gapless phases. The spin gap of the system can be obtained by Padé-fitting of the low-temperature susceptibility of the chain. We find several gapped phases which are the Haldane, Néel, and large-D phases in addition to only one gapless regime which is the Luttinger liquid phase. In order to determine the transition points between the Néel and the Haldane phases, we analyze the long distance spin-spin correlations of the system. After studying the phase diagram of the chain, we evaluate the dynamics of different quantum phases by looking at the DSF of the chain at magnetic fields up to $h/J = 0.6$ and for a range of single-ion anisotropies, $D/J = 0, \pm 0.2, \pm 0.5$. We discuss the low-lying excitations of the model, including a single-magnon mode and multi-particle continua, and their evolution in terms of h and D. For the special case of $h = 0$ and $D = 0$, the spectrum of excitations has been already predicted by non-linear σ model and a time-dependent density matrix renormalization group (t-DMRG) method [29, 30]. We compare our results to the spectra of those methods and comment on their similarities and differences. Finally, we access the NMR relaxation rate from our DSF data and give its dependence of both parameters, i.e. D and h.

Switching to quasi-one dimensional systems, we turn to the lattice structures shown in Fig. 1.1(c),(d). Panel (c) of the figure depicts a frustrated four-leg spin-1/2 tube (FFST) with antiferromagnetic exchanges, where the nearest and the next nearest couplings are

labeled by $J_{0,1}$ and J_2, respectively. Panel (d) shows a ladder with an arbitrary number of legs, where the leg and rung couplings are labeled by $J_\parallel$ and $J_\perp$, respectively.

In chapter 5, we study the magnetism of FFST in the limit of large leg couplings where QMC can be used. This chapter is motivated by the recent experimental and theoretical surveys on the tube, where in the experimental case, an actual realization of a four-leg spin tube, $Cu_2Cl_4{\cdot}D_8C_4SO_2$, has been investigated by inelastic neutron scattering [12, 31, 32] and in the theoretical case, a restricted regime of the tube's phase diagram has been studied using a series expansion method [33]. Additional studies using various other methods including DMRG, ED, Schwinger boson mean field theory (SBMFT) have been performed for intermediate values of J_2/J_0 and J_1/J_0 [34]. Here, we focus on the limit $J_0 = 0$, where we explore thermodynamic properties as well as spin dynamics of the tube as a function of the ratio J_2/J_1. In the limit of $J_2 \sim J_1$, the classical arrangement of the spins is similar to that of a spin-2 antiferromagnetic chain, while in the limit of $J_2/J_1 \sim 0$, we would have four decoupled spin-1/2 chains. Thus, one expects a crossover from a gapped Haldane state to a gapless Luttinger liquid phase as the ratio J_2/J_1 varies from 1 to 0. We obtain evidence for such a crossover from the spin gap, and also the excitation spectrum of the system. We also show the temperature dependence of the dynamic structure factor of the tube for $J_2 \sim J_1 \gg J_0$. This might be of interest in the context of related experiments [31] on four-spin tube compound $Cu_2Cl_4{\cdot}D_8C_4SO_2$.

Finally, we address spin dynamics of N-leg ladders in chapter 6. The main topic of this chapter is to study the dynamics of such systems as a function of the number of legs. First, we give an overview of the known low-temperature susceptibility of N-leg ladders based on the QMC study of Ref. [35], where the clear difference between the energy gap of odd- and even-leg ladders has been detailed. We go beyond these studies and perform QMC calculations for the DSF of ladders with $N = 2, 3, 4, 5$ legs. We show that the spectrum of odd- and even-leg ladders can be clearly distinguished by the fact that the first one has a gapless spectrum similar to that of a single spin-1/2 chain while the latter displays magnon-like excitations with a gap which scales inversely exponential in the number of legs. At the end of the chapter, we also compare the DSF to some recent RIXS experiment on a potential five-leg ladder system $La_8Cu_7O_{19}$ [36].

2. Methods

In this chapter, the general formulation of the quantum Monte Carlo (QMC) method based on a stochastic series expansion (SSE) will be described. This method which is a generalization of Handscomb's algorithm [37] was first introduced by Sandvik and Kurkijrvi [38]. The implementation of the method was improved later on by developing the loop update [39] and the directed loops algorithm [22]. It is an exact method proposed for finite temperature QMC simulations of lattices for which the sign problem can be avoided [40]. The method can be however used down to very low temperatures near the ground state.

The outline of this chapter is as follows. First, a short overview of *Monte Carlo sampling* will be given in section 2.1. The idea of *importance sampling* and methods of applying this idea will be introduced in this section. In section 2.2, the general framework of the SSE method as an efficient method for QMC, will be discussed. In addition to the general formulation, tools and requirements for implementation of the method including the two concepts of *vertices* and *updating* will be addressed in this section. Then the static and dynamic quantities will be discussed in section 2.3 and how these quantities are obtained from the SSE method will be explained. One important issue when measuring the physical quantities is the estimation of statistical errors. What is the relation between statistical errors and the concept of *autocorrelation times*, and how to efficiently control the errors, is the topic of section 2.4. In section 2.5, different methods and efficient algorithms of analytical continuation are introduced and finally a short summary of the chapter is given in section 2.6.

2.1. Monte Carlo sampling

Monte Carlo methods are stochastic techniques based on random sampling to obtain numerical results for many problems for which deterministic algorithms fail or are not efficient (for a review see Refs. [41, 42]). In quantum mechanical problems with many degrees of freedom, Monte Carlo methods can be used to calculate expected values of observables. An essential concept in Monte Carlo sampling is *importance sampling* which will be explained in the following section.

2.1.1. Importance sampling

An example of Monte Carlo sampling is to numerically integrate a function especially in high dimensions where the usual integral methods are not efficient. We use this example to explain the concept of importance sampling. According to simple Monte Carlo sampling, the integral of a function $f(\mathbf{x})$ can be approximated by

$$\frac{1}{\Omega}\int f(\mathbf{x})d\mathbf{x} \approx \frac{1}{N}\sum_{i=1}^{N} f(\mathbf{x}_i), \tag{2.1}$$

where $\mathbf{x}_i$ are N random points uniformly distributed in the integration space and $\Omega = \int d\mathbf{x}$ is the total volume of integration. The uniform sampling of the function is practically ineffective, because it may happen that the contributions to the integral in different regions of the integration space are not comparable. This is the case for functions which are strongly peaked in some regions. To accurately obtain the integral of such functions in a more efficient way and a reasonable computational time, one uses importance sampling. The idea is to introduce a probability distribution function or a weight $w(\mathbf{x})$ where $\int w(\mathbf{x})d\mathbf{x} = 1$, and choose the points or the samples, $\mathbf{x}_i$, not uniformly but according to the function $w(\mathbf{x})$. Thus one can rewrite Eq. 2.1 as follows

$$\frac{1}{\Omega}\int \frac{f(\mathbf{x})}{w(\mathbf{x})}w(\mathbf{x})d\mathbf{x} \approx \frac{1}{N}\sum_{i=1}^{N} \frac{f(\mathbf{x}_i)}{w(\mathbf{x}_i)}. \tag{2.2}$$

By choosing a proper w function, ideally very similar to the function f, we have a rather constant ratio of f/w and consequently a more accurate approximation of the integration. The remaining question is how to select the w-distributed points $\mathbf{x}_i$. The answer of this question is given by introducing *Markov processes*, where the random points $\mathbf{x}_i$ are regarded as states or configurations of the system.

2.1.2. Markov processes

An important part of a Monte Carlo simulation is the generation of random states. A state can be any configuration of the system for example an arrangement of spins in a spin lattice model or random points $\mathbf{x}_i$ in the integration example. These random states can be generated using Markov processes. A Markov process is a mechanism in which, given a system in one state s_i, a new state of the system s_j is randomly generated. The next state is chosen using the transition probability $P(s_i \to s_j)$ satisfying the condition $\sum_j P(s_i \to s_j) = 1$ where the sum is over all accessible configurations. The transition probability should satisfy two conditions. Firstly, it should be independent of time and

secondly, it should only depend on the properties of the two states s_i and s_j and not on other system's states. It is worth mentioning that the probability $P(s_i \to s_i)$ does not necessarily need to be zero, i.e. the transition from a state to itself is also possible. These Markov processes are used subsequently to create a Markov chain of states. In addition to the already specified conditions on Markov processes, there are two more constraints on Markov chains, the so called *ergodicity* and *detailed balance*.

Ergodicity This condition states that it should be possible for a Markov chain to reach any state of the system from any other one in a finite number of Markov processes. In other words, the system should have the same behavior averaged over time as averaged over the space of all states of the system. Ergodicity condition guarantees that there must be at least one path with finite transition probabilities between any two system's states, even though there might exist some zero transition probabilities in the Markov processes.

Detailed balance Detailed balance implies that the rate at which the system makes transitions into and out of any state s_i must be equal. It means that if the transition probability $P(s_i \to s_j)$ is finite with the weights w_{s_i} and w_{s_j}, the reverse transition must also be possible with a finite probability $P(s_j \to s_i)$. Mathematically speaking, the detailed balance can be written as

$$P(s_i \to s_j) w_{s_i} = P(s_j \to s_i) w_{s_j}, \tag{2.3}$$

or alternatively

$$\sum_i P(s_i \to s_j) w_{s_i} = w_{s_j}. \tag{2.4}$$

One of the most common and simple Markov chain algorithms which can be applied to a wide class of Monte Carlo problems, is the Metropolis algorithm [43]. This algorithm can be described by the following steps:

1. Pick an arbitrary initial state s_i.

2. Propose a small change δ in the state by introducing a trial state $s_j = s_i + \delta$ and calculate the ratio of the weights $R = \frac{w_{s_i}}{w_{s_j}}$.

3. Pick a random number r between 0 and 1. If $r \leqslant R$, set $s_{i+1} = s_j$. Otherwise, set $s_{i+1} = s_i$.

4. Replace s_i by s_{i+1} and go to step 2.

Step (4) is repeated N times, where N should be large enough to satisfy the ergodicity condition.

Various Monte Carlo sampling can be applied to both classical and quantum mechanical systems. For quantum many-body systems, SSE is one of the methods which due to discrete nature of its configuration space, can be efficiently implemented in most cases.

2.2. Stochastic series expansion (SSE)

Here for the sake of simplicity, the stochastic series expansion (SSE) method will be first described for simulations of the anisotropic $S = 1/2$ Heisenberg model subject to a finite magnetic field

$$H = J \sum_{\langle i,j \rangle} [S_i^x S_j^x + S_i^y S_j^y + \Delta S_i^z S_j^z] - h \sum_i S_i^z, \tag{2.5}$$

where J is the coupling constant between pairs of interacting spins S_i, S_j on a lattice which can in principle have any number of dimensions. Δ denotes the uniaxial anisotropy and h is the external magnetic field. The SSE method can then be generalized to any lattices with arbitrary spins and dimensions. The starting point of the SSE method is a Taylor expansion of the partition function for a spin model

$$Z = \mathrm{Tr}\{\mathrm{e}^{-\beta H}\} = \sum_\alpha \sum_{n=0}^{\infty} \frac{(-\beta)^n}{n!} \langle \alpha | H^n | \alpha \rangle , \tag{2.6}$$

where β is the inverse temperature $\beta = 1/k_B T$ and $|\alpha\rangle$ is a Hilbert space basis of the Hamiltonian H. For our Hamiltonian, it is more convenient to choose the standard basis, i.e. the eigenstates of the z components of spin operator $\hat{S}$

$$|\alpha\rangle = |S_1^z, S_2^z, \ldots, S_N^z\rangle. \tag{2.7}$$

The Hamiltonian can then be decomposed into a sum of bond Hamiltonians H_b

$$H = -J \sum_{b=1}^{N_b} H_b, \qquad (J > 0), \tag{2.8}$$

where H_b is an operator on bond b which connects the two spins $i(b), j(b)$. Each bond operator can be also decomposed into two operators

$$H_b = H_{1,b} - H_{2,b}, \tag{2.9}$$

with $H_{1,b}$ ($H_{2,b}$) being the diagonal (off-diagonal) operator

$$H_{1,b} = C - \Delta S^z_{i(b)} S^z_{j(b)} + h_b[S^z_{i(b)} + S^z_{j(b)}], \tag{2.10}$$

$$H_{2,b} = \tfrac{1}{2}[S^+_{i(b)} S^-_{j(b)} + S^-_{i(b)} S^+_{j(b)}], \tag{2.11}$$

where C is a constant which is chosen such that it guarantees the positiveness of all $H_{1,b}$'s matrix elements and consequently the Metropolis weights in sampling procedure. One can simply take $C = \Delta/4 + h_b + \epsilon$ with a positive ϵ. For a d-dimensional lattice with L sites, the number of bonds is $N_b = dL$. The way the sites and the bonds of a lattice are labeled, is shown for a square lattice of 4 sites, as a sample, in Fig. 2.1. The contribution of the magnetic field to each bond is shown by h_b which, for our example, is $h/2Jd$. Taking all these considerations into account for the Hamiltonian of our model, the partition function in Eq. 2.6 is written as

$$Z = \sum_{\alpha} \sum_{n=0}^{\infty} \sum_{S_n} (-1)^{n_2} \frac{\beta^n}{n!} \left\langle \alpha \left| \prod_{i=1}^{n} H_{a_i,b_i} \right| \alpha \right\rangle, \tag{2.12}$$

where S_n denotes an operator-index sequence $S_n = [a_1, b_1], [a_2, b_2], \ldots, [a_n, b_n]$ in which $a_i \in \{1, 2\}$ corresponds to the type of operators (1=diagonal, 2=off-diagonal) and $b_i \in \{1, \ldots, N_b\}$ is the bond index. n_2 indicates the number of spin-flipping operators $H_{2,b}$. For bipartite (unfrustrated) lattices, there is always an even number of the spin-flipping operators and since the exchange coupling J is positive, the term $(-1)^{n_2}$ in Eq. 2.12 is equal to one, thus we have

$$Z = \sum_{\alpha} \sum_{n=0}^{\infty} \sum_{S_n} \frac{\beta^n}{n!} \left\langle \alpha \left| \prod_{i=1}^{n} H_{a_i,b_i} \right| \alpha \right\rangle. \tag{2.13}$$

For non-bipartite lattices for which the exchange coupling J is frustrated, the term $(-1)^{n_2}$ can not be managed and the so called *sign problem* arises which leads to some statistical problems especially at low temperatures. Many attempts have been made to solve the sign problem in frustrated systems, but except for some special cases [44–46], the problem has not yet been solved. One example of the frustrated magnets where the sign problem can be avoided, is a Heisenberg model with ferromagnet z exchange coupling but antiferromagnet xy exchange coupling [45]. Here, however, we restrict ourselves to spin systems with no frustration.

By allowing the expansion order n to approach ∞ in Eq. 2.13, there is in principle no error in the expansion, but to simplify the Monte Carlo measurements, the expansion

order can be truncated at a maximum power M.

$$Z = \sum_{\alpha} \sum_{S_M} \frac{\beta^n (M-n)!}{M!} \left\langle \alpha \left| \prod_{i=1}^{M} H_{a_i,b_i} \right| \alpha \right\rangle, \tag{2.14}$$

where we have n bond operators of the types $H_{1,b}$ and $H_{2,b}$ and we introduce $M-n$ *unit operators* $H_{0,0} \equiv 1$ to artificially grow the operator-index sequences to the length M. Choosing an appropriate maximum expansion order M during the equilibration of the simulation is very important. It has to be adjusted such that it is never reached by n (the actual expansion order) during the simulation. It is thereby possible to completely neglect the truncation error. Based on this partition function, a QMC procedure can be used to sample the basis and operators (α, S_M). As is explained in section 2.1, to perform a Monte Carlo sampling, we need to have the probability distribution or weight of each configuration (α, S_M) and the transition probability between the configurations. Using Eq. 2.14, the weights $W(\alpha, S_M)$ are given by

$$W(\alpha, S_M) = \frac{\beta^n (M-n)!}{M!} \left\langle \alpha \left| \prod_{i=1}^{M} H_{a_i,b_i} \right| \alpha \right\rangle. \tag{2.15}$$

While the weights are obtained using the matrix elements of the Hamiltonian, the transition probabilities between the configurations depend on the applied algorithm. This will be more lengthily explained in section 2.2.2. To obtain the weights $W(\alpha, S_M)$ in Eq. 2.15, one needs to describe the operation of the operator string $\prod_{i=1}^{M} H_{a_i,b_i}$ on the basis $|\alpha\rangle$. To this end, it is more convenient to use the concept of *vertices*.

2.2.1. Representation of linked vertices

An important step in implementing QMC sampling is the way we represent the basis states, the operators and their operation. In QMC simulation, a good representation helps to store information of the basis states and operators in a simple and efficient way. A very handy representation in SSE method is the linked vertices. Before introducing vertices, we should first define *propagated states*. As seen in Eq. 2.15, to achieve the weight function, the initial state $|\alpha\rangle$ must be operated M times by the Hamiltonian $H_{a,b}$ and matches itself at the end. It would be very useful to know the state or configuration of the system $|\alpha\rangle$ at each step of the M operations. Thus a propagated state at step p is defined as

$$|\alpha(p)\rangle \sim \prod_{i=1}^{p} H_{a_i,b_i} |\alpha\rangle, \tag{2.16}$$

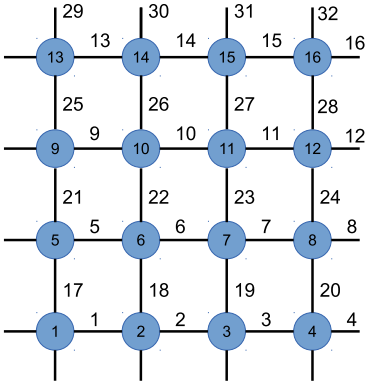

Figure 2.1.: The labeling of a periodic square lattice 4×4 is illustrated. Spins are shown as circles which are labeled by their numbers. Bonds (solid lines) and their corresponding bond numbers are also shown.

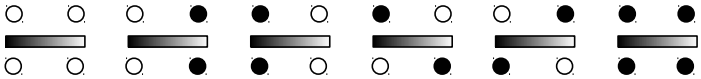

Figure 2.2.: The six allowed vertices for an antiferromagntic spin-1/2 Heisenberg chain is shown. Solid and open circles correspond to spin up and down respectively. Each vertex contains of two pairs of spins which are connected by an operator (the horizontal bar). This operator can be diagonal or off-diagonal depending on the corresponding bond Hamiltonian.

where all $|\alpha(p)\rangle$ are basis states. The evolution from $|\alpha(p)\rangle$ to $|\alpha(p+1)\rangle$ is either a flipping of a spin pair or no change at all. Therefore it is of more relevance to write the propagated states on the basis of two-spin states

$$|\alpha_{b_p}(p)\rangle = |S^z_{i(b_p)}(p), S^z_{j(b_p)}(p)\rangle, \tag{2.17}$$

where the spins are at bond b_p in the propagated state $|\alpha_{b_p}(p)\rangle$. With this definition, the weight factor in Eq. 2.15 can be written as

$$W(\alpha, S_n) = \frac{\beta^n}{n!} \prod_{p=1}^{n} \langle \alpha_{b_p}(p)|H_{b_p}|\alpha_{b_p}(p-1)\rangle. \tag{2.18}$$

Here we use a network of vertices to represent the corresponding matrix elements of this weight function. Each vertex consists of two entering spins $S^z_i(p), S^z_j(p)$, two outgoing

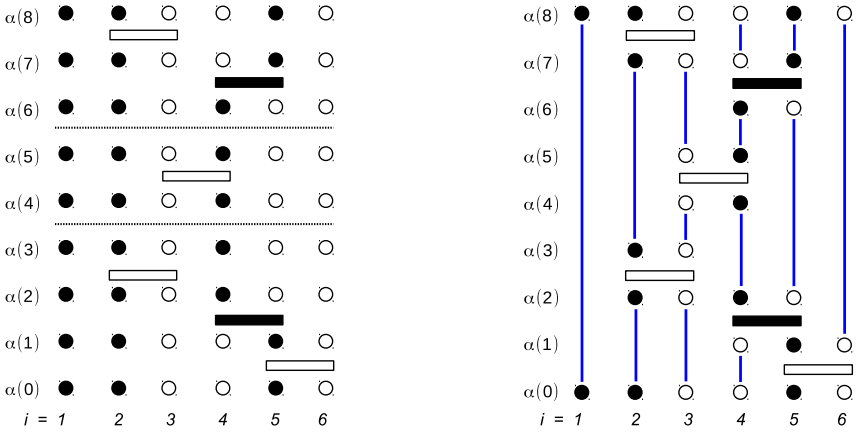

Figure 2.3.: Representation of propagated states for spin-1/2 chain with 6 lattice sites. Solid and open circles represent spin up and down respectively. The expansion order is shown on the left side of each panel by $\alpha(p)$ where $0 \leq p < 9$. Solid bars (open bars) correspond to the off-diagonal (diagonal) operators and the dashed lines indicate the unit operators. Diagonal and off-diagonal operators act on bond b which is the bond between spins of two sites b and $b+1$. In the left panel, the absence of diagonal or off-diagonal operator can be interpreted as a unit operator for which the corresponding spins are also depicted. In the right panel these unit operators and their spins are replaced by a link between legs of real operators.

spins $S_i^z(p+1), S_j^z(p+1)$ and a bond operator of any type which connect the two states $\alpha(p)$ and $\alpha(p+1)$. These vertices for the case of antiferromagnetic spin-1/2 Heisenberg chain are depicted in Fig. 2.2. There are only six allowed vertices in this case which correspond to the nonzero matrix elements of the Hamiltonian.

To construct a full representation of the propagated states, a simple way is to add an extra dimension to the real dimensions of the system, the so called propagating direction where one can map the evolution of states including the basis and the operators. In the left panel of Fig. 2.3, this is shown for an antiferromagnet spin-1/2 Heisenberg chain, where we only have two degrees of freedom for spin, up and down. This representation can be further simplified, if we skip the legs of vertices with unit operators, since they do not change the states of configuration. So in the new representation, only vertices with non-unit bond operators are linked to each other and instead of all spin configurations and operator strings of the system, a linked list of all vertices is stored. This list is a

more handy and efficient representation while doing the loop update (to be explained in the next section). The linking of vertices is done such that each leg of a vertex is linked either to the next or to the previous vertex (in the direction of propagation) at the same site. Since the periodic boundary condition of the propagated states has to be fulfilled, we end up having a bidirectional vertices configuration in which any arbitrary leg of a vertex has an incoming and an outgoing link. For our example which is an antiferromegnetic spin-1/2 Heisenberg chain, this representation is shown in the right panel of Fig. 2.3.

2.2.2. Updating

The starting point of the simulation is a randomly chosen state $|\alpha\rangle$ and an operator string with unit operators which have to be updated to achieve new allowed configurations (α, S_n). In this section two types of updating will be described through which one can do the importance sampling of different configurations. The first type of update is called diagonal update where the changes associated with the expansion order, and creating or annihilating diagonal operators are done. In the second update which is called loop update, changes of the type $[1, b_i] \leftrightarrow [2, b_i]$ (*diagonal*$\leftrightarrow$ *off-diagonal*) are considered.

Diagonal update

In this update, the expansion order n is changed by increasing and decreasing the number of unit operators. Diagonal and unit operators can be substituted with each other $([0,0]_p \leftrightarrow [1,b]_p)$ according to the acceptance probabilities

$$P([0,0]_p \to [1,b]_p) = \min\left(1, \frac{N_b \beta \langle \alpha(p)|H_{1,b}|\alpha(p)\rangle}{M-n}\right), \tag{2.19}$$

$$P([1,b]_p \to [0,0]_p) = \min\left(1, \frac{M-n+1}{N_b \beta \langle \alpha(p)|H_{1,b}|\alpha(p)\rangle}\right), \tag{2.20}$$

where N_b is the number of bonds. The process of these updates is in the way that during the propagating of $\alpha(p)$ from $p = 1$ to $p = M$, there are three possible cases to treat. If a unit operator is encountered, the expansion order is increased by one and a new diagonal operator according to Eq. 2.19 is inserted and the corresponding bond is chosen randomly out of all N_b bonds. If a diagonal operator is encountered, it will be removed according to the probability in Eq. 2.20 and the expansion order is decreased by one. In the case of off-diagonal operator, no change is made and the process is continued.

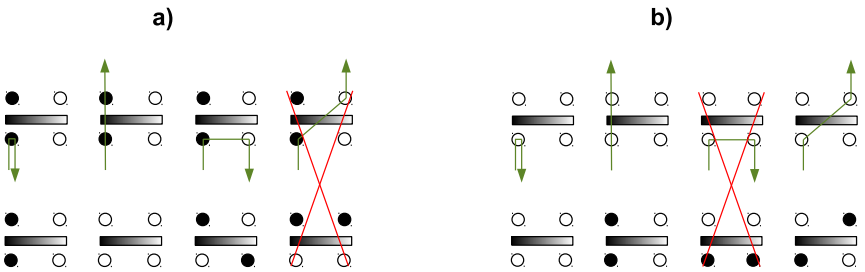

Figure 2.4.: All paths through two examples of vertices with the lower left leg as the entrance. The upper configurations are before updating while the results of updating are shown in lower configurations. The green arrows show the path of flipping spins and head the exit leg. from left to write of each panel, the processes are called *Bounce, Continue-straight, Switch-and-reverse* and *Switch-and-continue* respectively. One process of each panel has been marked as a forbidden process since the it does not correspond to operators of the Hamiltonian.

Loop update

In contrast to the diagonal update where only diagonal operators are involved, in the loop update, off-diagonal operators are also regarded. The purpose of this update is to include modifications of the type $[1, b]_p \leftrightarrow [2, b]_p$ to create new configurations and consequently new contributions to the partition function. In this update, the expansion order does not change and the rearrangement of unit operators are not considered. The loop update is carried out with the help of linked vertices representation introduced in section 2.2.1.

The process of loop update starts with constructing closed loops in the list of linked vertices. Each loop has a starting point which is a randomly chosen leg of a vertex, i.e. the entrance leg of that vertex. The loop continues its way by choosing an exit leg of the vertex. The way the exit leg is chosen will be explained later in this section. Since we are using the vertex representation, an exit leg of the preceding vertex is linked to a leg of the neighbor vertex and on the way of the loop, this is the entrance leg of the new vertex. This process goes on until the starting point of the loop is met again and the loop is closed. Along the loop path, all spins on the visited legs are flipped, thereby a new vertex list is generated and consequently new configurations contributing to the partition function are created.

In Fig. 2.4, given a special entrance leg of the vertex (the first lower leg) all possible loop paths through two different vertices are shown. Some of the paths are not allowed because

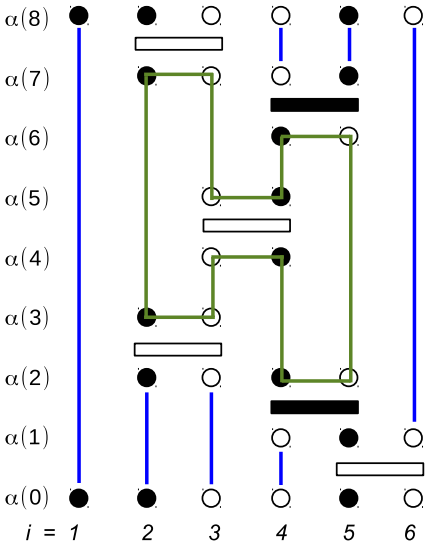

Figure 2.5.: A simple example of a loop path is shown for a lattice of 6 sites for which the representation of propagated states in Fig. 2.3. The green line here shows the path of the loop and following this path all visited spins must be flipped. In this example all visited vertices except for the one between two orders $\alpha(4)$ and $\alpha(5)$ are affected by a diagonal $\leftrightarrow$ off-diagonal type change.

of the absence of the corresponding matrix elements in the weight function (excluded with the cross signs in Fig. 2.4). As seen in the figure, there are in general four types of path that a loop can follow as the entrance leg is already chosen. For each panel from left to right, they are respectively called *bounce, continue-straight, switch-and-reverse*, and *switch-and-continue*. Each of these paths except for the bounces is associated with spin-flipping and also changing the bond operator of the vertex. One can already guess that bounces are not making any progress in updating because they create no new configurations and on the way back, destroy the changes which have been made during the loop. Therefore they must be excluded as much as possible so that the update is well optimized. This will be fully explained in the discussion of directed loops.

The length and the number of loops are two important factors which can highly affect the efficiency of the loop update. The number of loops can highly vary for different cases and should be fixed before loop update to avoid any bias in the measurements. Therefore it is adjusted during the equilibration of the simulation and usually is determined so that the

average number of visited vertices during one Monte Carlo step is approximately twice the size of the average or maximum expansion order. A Monte Carlo step refers to a sweep of diagonal updates and several loop updates so that a significant fraction of the vertices are visited. Regarding the loop length, it is usually much smaller than the number of bond operators, but in some cases it can be a major proportion of that. In very rare cases, very long loops can occur. They have to be terminated not to freeze the measurement. When the loop length is recorded, bounces are not taken into account because they do not contribute any change to the vertex. A simple example of a loop path is illustrated in Fig. 2.5 where the loop is shown by a green solid line walking through vertices in the configuration space.

Directed loops

As mentioned before, one repeating step in the loop path is to choose the exit leg in a vertex when the entrance leg is already given. One algorithm satisfying the detailed balance during the loop update is the heat bath. In this algorithm, the probability of exiting from a spacial leg is proportional to the corresponding matrix element with the flipped spins at both entrance and exit legs [39]. The factor of proportionality has to be chosen such that the sum of all possible probabilities is one. As an example for this algorithm, suppose that a loop passes a vertex with all spins originally pointing up, if the entrance leg is leg number 1 of the vertex, the probability of exit from leg number 3 of that vertex can be written as

$$P_{1\longrightarrow 3} = \frac{\langle - + |H_b| - + \rangle}{\langle - + |H_b| - + \rangle + \langle + - |H_b| - + \rangle + \langle + + |H_b| + + \rangle}, \tag{2.21}$$

where + (−) indicates spin up (down) state. The third term in the denominator of the above probability corresponds to the bounce probability and is always nonzero. As it was discussed, bounces are not good for the efficiency of the loop update. Therefore the idea of directed loops was suggested [22] in which bounces can be minimized or completely avoided. The heat-bath solution is, in fact, one special solution of the directed-loop equations. The term "directed" refers to the directional path through vertices, that is, the probability of going along a path is not equal with its revers process.

The basic equation of the directed-loop algorithm is the detailed balance equation which can be written as follows

$$P(s \to s^{'})W(s) = P(s^{'} \to s)W(s^{'}), \tag{2.22}$$

where s is a configuration with the weight $W(s)$, and $P(s \to s^{'})$ indicates the transition probability from the configuration s to $s^{'}$. $W(s)$ is expressed as a product over vertex

weights, as shown in Eq. 2.15 and $P(s \rightarrow s^{'})$ is written as a sum over all possible closed loops which result in the final configuration $s^{'}$. The general detailed balance equation for a loop update can be decomposed into detailed balance equations valid for every vertex. To do so, we introduce W_s as the weight of a bare vertex and $P(s, e \rightarrow s^{'}, x)$ as the probability given a configuration s and the entrance leg e to exit the vertex at leg x, resulting in the configuration $s^{'}$. Thus, using the definition $W(s, e, x) = W_s P(s, e \rightarrow s^{'}, x)$, the detailed balance valid for all possible vertices is written as

$$W(s, e, x) = W(s^{'}, x, e). \tag{2.23}$$

Another equation which has to be fulfilled for a vertex, is that the total probability of exiting a vertex after entering it, must equal one, i.e

$$\sum_{x} P(s, e, x) = 1, \tag{2.24}$$

or alternatively

$$\sum_{x} W(s, e, x) = W_s, \tag{2.25}$$

where the sum is over all legs on the vertex. Eqs. 2.23 and 2.25 are the basic elements of the directed-loop algorithm through which one constructs a set of equations to determine transition probabilities in the loop update.

In the case of XXZ model, given the entrance leg of a vertex, there are always three possible ways to exit, as shown in Fig. 2.4. To satisfy the detailed balance equation 2.23, we must only consider vertices in which given a path through the vertex, the reverse path also exists. One can divide all possible vertex configurations into eight subsets where the configurations within each subset transforms to each other while they do not transform into the configurations of the other subsets. In Fig. 2.6, half of these subsets are shown and the other half of them are obtained by interchanging up and down spins. Using Eq. 2.25, one relates the weight of a bare vertex to weights of all possible resulting configurations from a certain entrance leg. One can show that due to the symmetry of permuting the two spins of a bond and imaginary time inversion symmetry, for all the eight subsets, there are only two independent sets of equations resulting from Eq. 2.25. Each of the left quadrants of Fig. 2.6 belongs to one of these two independent sets. Therefore for the upper left quadrant of Fig. 2.6, we have

$$\begin{aligned} W_1 &= b_1 + a + b, \\ W_2 &= a + b_2 + c, \\ W_3 &= b + c + b_3, \end{aligned} \tag{2.26}$$

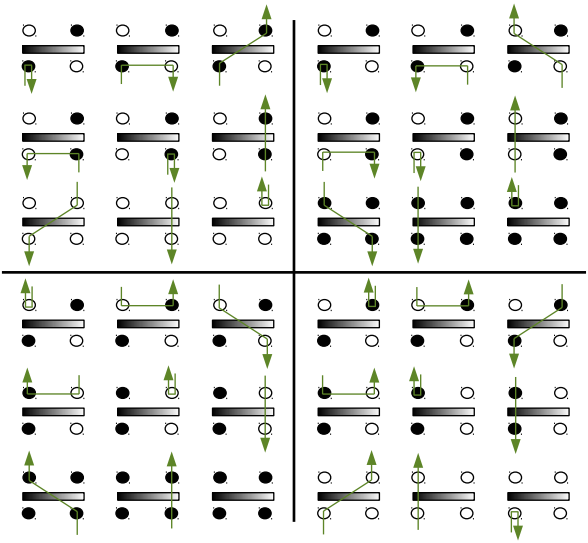

Figure 2.6.: Half of the all vertex configurations categorized in four subsets. The other half of them can be reached by interchanging up and down spins (solid and open circles). Configurations within one quadrant are transformed to each other by flipping the spins on the loop segment and reversing the arrow's direction while this is not the case for configurations within two different quadrants.

and for the lower left quadrant of that

$$\begin{aligned} W_1 &= b'_1 + a' + b', \\ W_2 &= a' + b'_2 + c', \\ W_4 &= b' + c' + b'_3. \end{aligned} \tag{2.27}$$

where the rows of these relations correspond to the rows in the figure, respectively, and the vertex weights are given by

$$\begin{aligned} W_1 &= \langle\uparrow\downarrow|H_b|\downarrow\uparrow\rangle = \langle\downarrow\uparrow|H_b|\uparrow\downarrow\rangle = 1/2, \\ W_2 &= \langle\downarrow\uparrow|H_b|\downarrow\uparrow\rangle = \langle\uparrow\downarrow|H_b|\uparrow\downarrow\rangle = \Delta/2 + h_b + \epsilon, \\ W_3 &= \langle\downarrow\downarrow|H_b|\downarrow\downarrow\rangle = \epsilon, \\ W_4 &= \langle\uparrow\uparrow|H_b|\uparrow\uparrow\rangle = \epsilon + 2h_b. \end{aligned} \tag{2.28}$$

where $\epsilon \geqslant 0$. The order of the symbols on the right sides of Eqs. 2.26 and 2.27 follows

the order of directed-loop segments in upper and lower quadrants of Fig. 2.6, respectively. Here b_i shows the bounce from the leg i of a vetex. It is worth noting that probabilities of selecting the exit legs are given by dividing the weights of the directed loop configurations such as $a, b, c, b_1, ...$ by the weight of the bare vertex. Eqs. 2.26 and 2.27 can be written in terms of the bounce weights $b_1, \ldots, b'_3$ as follows

$$\begin{aligned}
a &= \frac{1+\Delta}{4} + \frac{h_b}{2} + \frac{-b_1 - b_2 + b_3}{2}, \\
b &= \frac{1-\Delta}{4} - \frac{h_b}{2} + \frac{-b_1 + b_2 - b_3}{2}, \\
c &= \frac{\Delta-1}{4} + \frac{h_b}{2} + \epsilon + \frac{b_1 - b_2 - b_3}{2}, \\
a' &= \frac{1+\Delta}{4} - \frac{h_b}{2} + \frac{-b'_1 - b'_2 + b'_3}{2}, \\
b' &= \frac{1-\Delta}{4} + \frac{h_b}{2} + \frac{-b'_1 + b'_2 - b'_3}{2}, \\
c' &= \frac{\Delta-1}{4} + \frac{3h_b}{2} + \epsilon + \frac{b'_1 - b'_2 - b'_3}{2},
\end{aligned} \tag{2.29}$$

These linear equations can be solved either analytically or with the help of linear algebra libraries to obtain the transition probabilities. When obtaining the optimized solutions (where bounces are minimized), the requirement of non-negative weights and probabilities must be obeyed. Doing so, one can obtain the optimized solutions in terms of the two variables, the magnetic field on a bond h_b, and the anisotropy Δ, where there exists one region in which all bounce weights are zero. This is shown in Fig. 2.7, where the region with zero bounces is represented as a shaded area. In other regions, at least one nonzero bounce weight exists but still the smallest possible values for the bounce weights are obtained. Transitions between these regions are continuous, i.e for example by entering from the shaded region into other regions, the bounce weights increase continuously. The nonzero bounce weights and the minimum values of ϵ for different regions of the h_b-Δ phase diagram are given in table 2.1.

2.3. Physical quantities

After introducing the basic principles of the SSE method, now it is time to calculate physical quantities within this framework. We divide physical quantities into two types, first static ones such as susceptibility, static correlation functions, magnetization, energy and specific heat and second, dynamic ones including longitudinal and transverse dynamic structure factor. General considerations with regard to simulation of these two types of quantities will be discussed in this section.

	bounce weights		$\epsilon_{\min}$
I			$(\Delta^- - h_b)/2$
II	$b_2 = h_b - \Delta^-$	$b'_2 = -h_b - \Delta^-$	0
III	$b_2 = h_b - \Delta^-$		0
IV	$b_2 = h_b - \Delta^-$	$b'_3 = h_b - \Delta^+$	0
V		$b'_3 = h_b - \Delta^+$	$(\Delta^- - h_b)/2$
VI	$b_3 = -h_b - \Delta^+$	$b'_3 = h_b - \Delta^+$	$-h_b - \Delta/2$

Table 2.1.: Table of non-zero bounce weights and minimum values of ϵ (taken from Ref. [22]) for different regions of the optimized solution of the directed loop equations. The Roman numerals correspond to those in Fig. 2.7 and $\Delta^\pm$ are defined as $\Delta^\pm = (1 \pm \Delta)/2$.

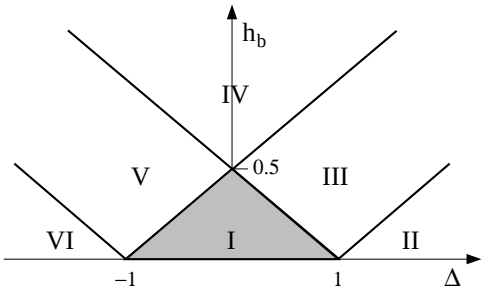

Figure 2.7.: The phase diagram of the regions of the XXZ chain with different bounce weights are shown. The shaded region refers to a region where all bounce weights are zero. In other regions there are different types of nonzero but minimized bounce weights [22].

2.3.1. Static quantities

In principle, using the SSE method, one can simply measure a large variety of static quantities. However here we just mention two of them which will be frequently calculated in the next chapters of this thesis. Let's first start with the static uniform susceptibility which can be written as the first derivative of the magnetization with respect to magnetic field

$$\chi = \frac{\partial M}{\partial B}. \tag{2.30}$$

The Magnetization itself is proportional to the derivative of the free energy and the free

energy is related to the partition function via

$$M = -\frac{\partial F}{\partial B}, \tag{2.31}$$

$$F = -\frac{1}{\beta}\ln Z. \tag{2.32}$$

So the susceptibility can be written as follows

$$\begin{aligned}\chi &= \frac{\partial}{\partial B}\left(\frac{g\mu_B}{Z}Tr[S^z e^{-\beta H}]\right) \\ &= g^2\mu_B^2\beta\left(\frac{Tr[(S^z)^2 e^{-\beta H}]}{Z} - \frac{(Tr[S^z e^{-\beta H}])^2}{Z^2}\right) \\ &= g^2\mu_B^2\beta\left(\langle(S^z)^2\rangle - \langle S^z\rangle^2\right).\end{aligned} \tag{2.33}$$

where g denotes the electron spin g-factor and μ_B is the Bohr magneton.

Another static quantity which has a great importance, specially when measuring the order of a spin system, is the statical spin-spin correlation function. As the name suggests, it indicates how two spins at two different sites of the real space are correlated. It is typically presented as a function of spacial distance between the two spins. The correlation between a spin and itself is called autocorrelation which is usually used for the normalization of spin-spin correlation functions. The autocorrelation function has always the maximum value of correlation functions. The static spin-spin correlation function between two spin sites i and j can be described by $\langle S_i^z S_j^z\rangle$. One can measure the correlation functions using only the initial state $|\alpha(0)\rangle$, but the statistical quality of this variable can be increased by averaging over all slices of the expansion order in the SSE method [38]

$$\langle S_i^z S_j^z\rangle = \left\langle \frac{1}{M}\sum_{p=0}^{M-1} S_i^z(p) S_j^z(p)\right\rangle \tag{2.34}$$

where $\langle ...\rangle$ denotes the thermal averaging and $S_i^z(p) = \langle\alpha(p)|S_i^z|\alpha(p)\rangle$. In the next chapters of this thesis, we will show how these two static quantities are used to characterize the quantum orders and phases of spin systems.

Improved estimators In some special cases, the statistical errors of expected values can be extremely reduced by using the so-called improved estimators [23, 47] which allow for smaller sample sizes. The idea is that instead of measuring the expected value of an observable A, we average over many estimators of the type $\bar{A}' = \bar{A} + \bar{\delta}$ where the added estimator $\bar{\delta}$ has zero expected value, $\langle\bar{\delta}\rangle = 0$. This free choice of the estimator $\bar{A}'$ which has a different variance, can be used to reduce the variance in the measurement. One

advantage of this averaging is that the time to accomplish it, is comparable to the time needed for a single measurement. As an example, the uniform spin susceptibility using an improved estimator is derived by dividing the space into loops at a given configuration. For a spin-1/2 model, this improved estimator can be introduced at vanishing magnetic fields. Starting from the expected value of the susceptibility which reads

$$\langle \chi \rangle = \beta \left\langle (M^z)^2 \right\rangle , \tag{2.35}$$

where M^z is the magnetization which can be written as a sum over all configurations

$$\langle M^z \rangle = \left\langle \sum_r S_r^z \right\rangle = \frac{1}{M} \left\langle \sum_l \sum_{(r,\tau)\in l} S_{r,\tau}^z \right\rangle , \tag{2.36}$$

in which subscripts r, τ respectively indicate spin sites and time slices of the loop l. Thus for the susceptibility, we have

$$\langle \chi \rangle = \beta \left\langle \left(\frac{1}{M} \sum_{\{l\}} \sum_{(r,\tau)\in l} S_{r,\tau}^z \right)^2 \right\rangle . \tag{2.37}$$

This can be divided into diagonal and cross terms

$$\begin{aligned} \langle \chi \rangle &= \frac{\beta}{M^2} \left\langle \sum_{\{l\}} \sum_{(r,\tau)\in l} \left(S_{r,\tau}^z \right)^2 \right\rangle \\ &+ \frac{\beta}{M^2} \left\langle \sum_{\{l\}} \sum_{(r,\tau)\in l} \sum_{\{l'\}} \sum_{(r',\tau')\in l'} S_{r,\tau}^z S_{r',\tau'}^z \right\rangle . \end{aligned} \tag{2.38}$$

Since the spin flipping takes place after generating all loops and flipping a loop reverses the sign of its total spin, the expected value of the cross terms is zero and the diagonal terms can be written as follows

$$\langle \chi \rangle = \frac{\beta}{M^2} \left\langle \sum_{\{l\}} (S_l^z)^2 \right\rangle , \tag{2.39}$$

with S_l^z being the total spin of a loop. For the sake of efficiency and to avoid overcounting of the loops, only one loop for each configuration is chosen. The probability of choosing one of the loops is $|l|/(MV)$, where $|l|$ is the length of the loop and MV indicates the number of the sites in the space-time area. So the final form of the susceptibility reads

$$\langle \chi \rangle = \frac{\beta}{M^2} \left\langle \frac{MV}{|l|} \left(S_l^z \right)^2 \right\rangle . \tag{2.40}$$

Since the only loops which wind around, in the time direction, contribute to the improved estimator, one can also write the susceptibility using the winding number $w_t(l)$

$$\langle \chi \rangle = \frac{\beta M}{4} \left\langle \frac{(w_t(l))^2}{|l|} \right\rangle . \tag{2.41}$$

2.3.2. Dynamic quantities

In the field of strongly correlated systems, dynamical quantities are among desirable and challenging quantities. They are very good links between theories and many experimental measurements. From an experimental point of view, these quantities are the *time-dependent* response of the system to an external perturbation. In the context of spin lattices, one of the most informative dynamic quantities is the dynamical structure factors (DSF) $S^{\mu\nu}(q,\omega)$ with $\mu,\nu = x,y,z$ which can be defined as the Fourier transform of the spin-spin correlation functions $\langle S^{\mu}_{\mathbf{r}_1}(t) S^{\nu}_{\mathbf{r}_2}(0)\rangle$. Mathematically, we have

$$S^{\mu\nu}(\mathbf{q},\omega) = \frac{1}{L} \sum_{\mathbf{r}_1,\mathbf{r}_2} \int_{-\infty}^{+\infty} dt e^{-i(\omega t - \mathbf{q}\cdot(\mathbf{r}_1-\mathbf{r}_2))} \langle S^{\mu}_{\mathbf{r}_1}(t) S^{\nu}_{\mathbf{r}_2}(0)\rangle, \tag{2.42}$$

where $\mathbf{r}_1$ and $\mathbf{r}_2$ label spin sites of a lattice. For an isotropic system with no magnetic field, the longitudinal dynamic structure factor S^{zz} is equal to the transverse ones S^{xx} or S^{yy}. DSFs are directly probed by inelastic neutron scattering (INS) experiments and they are also indirectly related to the nuclear magnetic resonance (NMR). The spin-lattice relaxation rate calculated by NMR is proportional to the integral of the dynamic structure factor over momentum space.

Since calculating the DSF is one important part of this thesis, a relevant question is how it can be obtained from QMC simulations. In principle the DSF can be calculated via the corresponding correlation functions in imaginary time [48, 49]. In the case of longitudinal correlation functions, we have

$$C^{zz}_{\mathbf{r}_1,\mathbf{r}_2}(\tau) = \langle S^{z}_{\mathbf{r}_1}(\tau) S^{z}_{\mathbf{r}_2}(0)\rangle. \tag{2.43}$$

To measure the correlations using SSE method, we start from the definition of the time evolution of spin-spin correlations in imaginary time

$$C^{zz}_{\mathbf{r}_1,\mathbf{r}_2}(\tau) = \frac{1}{Z} Tr[e^{\tau H} S^{z}_{\mathbf{r}_1} e^{-\tau H} S^{z}_{\mathbf{r}_2} e^{-\beta H}], \tag{2.44}$$

by Tylor-expanding the exponential terms, we obtain

$$C^{zz}_{\mathbf{r}_1,\mathbf{r}_2}(\tau) = \frac{1}{Z}\sum_{\alpha}\sum_{n=0}^{\infty}\sum_{m=0}^{\infty}\frac{(\tau-\beta)^n(-\tau)^m}{n!m!}\langle\alpha|H^n S^z_{\mathbf{r}_1} H^m S^z_{\mathbf{r}_2}|\alpha\rangle, \tag{2.45}$$

if we use the summation over operator-index sequences S_n, the equation can be rewritten as

$$\begin{aligned} C^{zz}_{\mathbf{r}_1,\mathbf{r}_2}(\tau) &= \frac{1}{Z}\sum_{\alpha}\sum_{n=0}^{\infty}\sum_{m=0}^{n}\sum_{S_n}\frac{(-\tau)^m(\tau-\beta)^{n-m}}{(n-m)!m!} \\ &\times \langle\alpha|\prod_{i=m+1}^{n} H^n_{a_i,b_i} S^z_{\mathbf{r}_1}\prod_{j=1}^{m} H_{a_j,b_j} S^z_{\mathbf{r}_2}|\alpha\rangle. \end{aligned} \tag{2.46}$$

Since $S^z|\alpha\rangle = S^z(p)|\alpha(p)\rangle$ and by comparing with the definition of the partition function in Eq. 2.13, the correlation functions can be written using the discrete expansion of the correlated sites in the direction of the expansion order

$$C^{zz}_{\mathbf{r}_1,\mathbf{r}_2}(\tau) = \left\langle \sum_{m=0}^{n}\frac{\tau^m(\beta-\tau)^{n-m}n!}{\beta^n(n-m)!m!}\bar{C}^{zz}_{\mathbf{r}_1,\mathbf{r}_2}(m)\right\rangle, \tag{2.47}$$

where

$$\bar{C}^{zz}_{\mathbf{r}_1,\mathbf{r}_2}(m) = \frac{1}{n+1}\sum_{p=0}^{n} S^z_{\mathbf{r}_1}(p) S^z_{\mathbf{r}_2}(p+m). \tag{2.48}$$

The correlation between diagonal operators like Eq. 2.47 can be evaluated during the diagonal update because there is no spin flipping process involved and the eigenvalues of diagonal operators are directly obtained. Similar to DSFs, when the Hamiltonian is isotropic and there is no external magnetic field applied to the system, the transverse correlation functions are equal to longitudinal correlations. In the existence of anisotropy or external field, the measurement of the transverse correlations is more complicated and needs more considerations. In this case, one can alternatively measure the correlations between spin raising and lowering operators S^+ and S^- which operate directly in the process of loop update. For this kind of operators Eq. 2.47 is still valid and moreover already in the loop update the detailed balance is satisfied and all sites and expansion orders are swept. How to record the correlations in the loop update is explicitly explained in Refs. [50, 51], but in a few words: we use Eq. 2.47 for spin raising and lowering operators and record only the correlations which correspond to spin flips. The type of right operator specifies the type of spin flipping and the summation in the expanding direction is over the moving operator in the spin flipping process while the other operator is at a fixed position.

One remaining question is how to obtain the real frequency DSF described in Eq. 2.42

from the imaginary time correlation functions. The answer to this question will be given in section 2.5. Before that however, we show how the statistical errors of QMC are estimated.

2.4. Autocorrelations and error estimation

One of the main issues when simulating physical quantities is the statistical error which has to be managed properly. In this section, we review the standard methods for estimating the statistical errors of QMC quantities, following Refs. [52–54]. Since the successive configurations generated in the Markov chain are usually correlated and these correlations are reflected in the measurements of physical quantities, one has to carefully take these correlations into account in order to properly determine the statistical errors of Monte Carlo simulations.

2.4.1. Estimators and autocorrelation times

For a time series of data obtained from the Markov chain of a Monte Carlo sampling, one can estimate the expected value $\langle A \rangle$ as a simple mean over the Markov chain

$$\langle A \rangle \approx \bar{A} = \frac{1}{N} \sum_{j=1}^{N} A_j \tag{2.49}$$

where N is the total number of measurements. This is worth noting that the estimator $\bar{A}$ must be conceptually distinguished from the expected value $\langle A \rangle$. While the expected value is a weighted average of all possible values, the estimator is a random number fluctuating around the expected value with the variance

$$\sigma^2_{\bar{A}} = \langle [\bar{A} - \langle \bar{A} \rangle]^2 \rangle = \langle \bar{A}^2 \rangle - \langle \bar{A} \rangle^2. \tag{2.50}$$

In the case of N uncorrelated subsequent measurements A_j, the above relation can be obtained from the variance of the individual measurements

$$\sigma^2_{\bar{A}} = \frac{\sigma^2_{A_j}}{N} = \frac{\langle A_j^2 \rangle - \langle A_j \rangle^2}{N}. \tag{2.51}$$

But when the measurements are correlated, the variance increases and can not be estimated using Eq. 2.51. The variance of correlated measurements reads

$$\sigma_{\bar{A}}^2 = \langle \bar{A}^2 \rangle - \langle \bar{A} \rangle^2 = \frac{1}{N^2} \sum_{i,j=1}^{N} \langle A_i A_j \rangle - \frac{1}{N^2} \sum_{i,j=1}^{N} \langle A_i \rangle \langle A_j \rangle, \tag{2.52}$$

which can be decomposed into diagonal and off-diagonal terms

$$\sigma_{\bar{A}}^2 = \frac{1}{N^2} \sum_{i=1}^{N} \left(\langle A_i^2 \rangle - \langle A_i \rangle^2 \right) + \frac{1}{N^2} \sum_{i \neq j}^{N} \left(\langle A_i A_j \rangle - \langle A_i \rangle \langle A_j \rangle \right). \tag{2.53}$$

The first term is again the variance of the individual measurements, times $1/N$. The summation in the second term can be reduced using the symmetry $i \leftrightarrow j$ and assuming the time translation invariance over the Markov chain

$$\sigma_{\bar{A}}^2 = \frac{1}{N} \left[\sigma_{A_i}^2 + 2 \sum_{t=1}^{N} \left(\langle A_i A_{i+t} \rangle - \langle A_i \rangle \langle A_i \rangle \right) \left(1 - \frac{t}{N} \right) \right], \tag{2.54}$$

where t is the time separation between different measurements of a Markov chain. By factoring out the $\sigma_{A_i}^2$ and using the definition of *integrated autocorrelation time* as

$$\tau_{int} = \frac{1}{2} + \sum_{t=1}^{N} C(t) \left(1 - \frac{t}{N} \right), \tag{2.55}$$

with

$$C(t) = \frac{\langle A_i A_{i+t} \rangle - \langle A_i \rangle \langle A_i \rangle}{\langle A_i^2 \rangle - \langle A_i \rangle \langle A_i \rangle}, \tag{2.56}$$

the variance can be written as

$$\sigma_{\bar{A}}^2 = \frac{\sigma_{A_i}^2}{N} 2\tau_{int}. \tag{2.57}$$

The autocorrelation $C(t)$ decays exponentially for a large time separation t

$$C(t) = a \exp(-t/\tau_{exp}), \tag{2.58}$$

where a is a constant and τ_{exp} is the *exponential autocorrelation time* which depends on the quantity A. Due to this exponential decay and for a large N the term t/N in Eq. 2.55 can be skipped and we are left with

$$\tau_{int} = \frac{1}{2} + \sum_{t=1}^{N} C(t). \tag{2.59}$$

The important point of Eq. 2.57 is that the statistical errors of correlated measurements obtained by $\sqrt{\sigma_{\bar{A}}^2}$ is increased by a factor of $\sqrt{2\tau_{int}}$ or equivalently, the effective number of measurements is decreased by a factor of $2\tau_{int}$ compared to the completely uncorrelated measurements, i.e. $N_{eff} = N/2\tau_{int}$. This means that every $2\tau_{int}$ iterations of the measurements are effectively uncorrelated. The discussion clearly demonstrates the very important role of autocorrelation times. Therefore, in such measurements, one should get a rough estimate of them.

2.4.2. Binning analysis

Since it is computationally difficult and often time consuming to get an accurate estimate of the autocorrelations especially for the dynamic quantities, the idea is to avoid correlations using other more convenient ways such as binning analysis. The basis of this analysis is to group the data in bins or blocks of a finite size, in order to create binned series of measurements with almost zero correlation. For N number of correlated measurements of A_i, one can create N_B number of bins, each including $k = N/N_B$ subsets. The average of each block is obtained by

$$A_{B,n} = \frac{1}{k}\sum_{i=1}^{k} A_{(n-1)k+i},\ n = 1, ..., N_B. \tag{2.60}$$

To avoid the correlation effects entirely, one has to choose bins of sufficiently large size. Then the variance can be obtained by

$$\sigma_{\bar{A}}^2 = \sigma_B^2/N_B = \frac{1}{N_B(N_B-1)}\sum_{n=1}^{N_B}(A_{B,n} - \bar{A}_B)^2, \tag{2.61}$$

where obviously $\bar{A_B} = \bar{A}$. An important technical point in the case of binning is that one should calculate the error estimates for bins of different length and make sure that they converge to a unique value. Otherwise the autocorrelation time is larger than the simulation time and to fix the problem one has to do longer simulations. Taking this point into account, the approach guarantees a very reliable estimate of the errors. One can also use this analysis to determine an autocorrelation time called the "binning autocorrelation" time. Using Eq. 2.57 and 2.61, we have

$$\frac{\sigma_B^2}{N_B} = \frac{2\tau_{int}\sigma_{A_i}^2}{N}, \tag{2.62}$$

which leads to

$$\tau_{bin} \equiv \tau_{int} = \frac{k\sigma_B^2}{2\sigma_{A_i}^2}. \tag{2.63}$$

As discussed above, binning is a very successful and reliable approach to estimate errors and avoid the correlations and therefore has been used to produce almost all quantities calculated throughout this thesis. However the problem is more challenging when one is dealing with quantities which are not directly measured in the simulation but instead as a non-linear combination of other observables such as $\langle A\rangle/\langle B\rangle$. In this case the Jackknife analysis is a more efficient method.

2.4.3. Jackknife analysis

In the Jackknife method [55, 56], we again create N_B number of bins with length $k = N/N_B$ but this time we have $N_B + 1$ evaluation of A where A_0 is one estimate including all bins and A_i $(i = 1, ..., N_B)$ contains all bins but the i-th one. As a result of this new configuration of blocks, the Jackknife procedure leads to smaller variance compared to the binning method. Thus the estimate of A reads

$$A = A_0 - (N_B - 1)(\bar{A} - A_0), \tag{2.64}$$

where $\bar{A} = \frac{1}{N_B}\sum_{i=1}^{N_B} A_i$ and the corresponding variance can be written as

$$\sigma_A^2 = \frac{N_B - 1}{N_B}\sum_{n=1}^{N_B}(A_i - \bar{A})^2. \tag{2.65}$$

The Jackknife method has the ability to handle error propagation and cross-correlations of combined quantities (functions of other quantities). However in the case of linear quantities both Jackknife and binning methods are equivalent.

2.5. Real frequency dynamical structure factor

In section 2.3.2, we showed how the imaginary time correlation functions are obtained using a summation over the correlations in the expansion order space. Now the question is how to transform these imaginary time data into the real frequency dynamical structure factor which can be directly compared with the relevant experimental measurements. The answer to this question is explained in the context of analytical continuation problem which will be described in this section.

2.5.1. Analytical continuation

In principle, QMC produces the imaginary time Green's function which for two operators A and B can be written as follows

$$G^{AB}(\tau) = -\langle T_\tau A(\tau)B(0)\rangle, \tag{2.66}$$

where τ denotes the imaginary time axis, T_τ the time ordering, and $\langle ...\rangle$ the grand canonical ensemble averaging over the states of the many-body system. One can also consider the wave vector dependence of the Green's functions but since it doesn't play a role in our discussion and for the sake of simplicity we skip it for the moment. The Green's function $G^{AB}(\tau)$ can be expressed in terms of Matsubara frequencies ω_n

$$G^{AB}(\tau) = \frac{1}{\beta}\sum_{\omega_n} e^{-i\omega_n\tau}G^{AB}(i\omega_n), \tag{2.67}$$

where $\beta = 1/K_BT$ and ω_n's are defined as $2n\pi/\beta$ for bosons and $(2n+1)\pi/\beta$ for fermions, with integer values of n. In the case where the operators A and B indicate the spin operators $S^{x,y,z}$, the periodic condition $G^{AB}(\tau) = G^{AB}(\tau+\beta)$ is satisfied and therefore we can use the bosonic frequencies $\omega_n = 2n\pi/\beta$. The process of transforming the Matsubara complex frequencies function into the real frequency function is called analytical continuation. One can relate $G^{AB}(i\omega_n)$ to the spectral density function $\chi^{''}(\omega)$

$$G^{AB}(i\omega_n) = \int_{-\infty}^{\infty} d\omega \frac{\chi^{''}(\omega)}{i\omega_n - \omega}. \tag{2.68}$$

Using Eqs. 2.67, 2.68 and also the relation between spectral function and dynamic structure factor in the bosonic case $\chi^{''}(\omega) = (1-e^{-\beta\omega})S^{AB}(\omega)$, we have

$$G^{AB}(\tau) = \frac{1}{\beta}\sum_{\omega_n} e^{-i\omega_n\tau}\int_{-\infty}^{\infty} d\omega \frac{(1-e^{-\beta\omega})S^{AB}(\omega)}{i\omega_n - \omega}. \tag{2.69}$$

Using Cauchy's residue and Mittag-Leffler theorems the summation over Matsubara frequencies can be performed and the relation is rewritten as

$$G^{AB}(\tau) = \int_{-\infty}^{\infty} d\omega e^{-\omega\tau}S^{AB}(\omega). \tag{2.70}$$

Now the main issue is to extract $S^{AB}(\omega)$ given that we have the $G^{AB}(\tau)$ from QMC and using the integral kernel $e^{-\omega\tau}$. Mathematically speaking, the transformation in Eq. 2.70 has to be inverted to obtain the real frequency results or the dynamic structure factor. This inversion is a mathematical ill-posed problem because there exists an infinite number of different $S^{AB}(\omega)$ resulting in the same $G^{AB}(\tau)$. Another problem is that the

statistical errors of QMC can highly change the solution and may lead to some non-physical structures. So it needs lots of effort and attention to select the best solution out of many possible solutions. There are several methods by which this problem has been addressed. Least-squares fit [57, 58], Pade approximant method [59], regularization [60–62] and maximum entropy [25] are the most common methods. In the least squares fitting, the real frequency spectrum is approximated with a set of box functions such that the position and the weight of these functions are determined by minimizing the least-squares misfit between the spectrum and the QMC data. The problem of this method is that by increasing the box functions, the fit becomes unstable and noisy. In the Pade approximant method , the Fourier transform of the $G^{AB}(\tau)$ in Matsubara frequencies space is fitted to a rational function of a given order. After finding the fitted parameters, the analytical continuation is carried out by replacing $i\omega_n = \omega + i\eta$ where $\eta \to 0$. In this method the weight of the spectrum is controlled by the value of η which has to be properly chosen. It is an efficient technique for very accurate data but not a reliable method for less precise data. There are also different types of regularization in which the main idea is to add some auxiliary constraints in order to simplify the problem and find the unique solution. Maximum entropy method (MEM) which can also be considered as a special case of regularization has been known as one of the most powerful methods to the inversion problem. Here we introduce the general idea and basics of this method which is used throughout the thesis.

2.5.2. Maximum entropy method (MEM)

In maximum entropy, Bayesian statistics is applied to find the most probable solution to the inversion problem. Since we obtain a vector of data for $\mathbf{G} = (G_{\tau_1}, .., G_{\tau_N})$ from QMC, here we focus on the numerical solution of Eq. 2.70. This means that we have an inversion problem with the form $\mathbf{A} = K^{-1}\mathbf{G}$ where $\mathbf{A} = (A_{\omega_1}, ..., A_{\omega_M})$ is a vector of discrete values of the spectrum $S^{AB}(\omega)$ and K is the kernel matrix with elements $K_{i,j\in M,N}$. In order to achieve the spectrum $\mathbf{A}$, K has to be mathematically inverted.

Bayes' theorem: Our task is to find the probability of $\mathbf{A}$ given $\mathbf{G}$. Since $\mathbf{A}$ is initially unknown, the Bayes' theorem helps us to link the probability of $\mathbf{A}$ given $\mathbf{G}$ to the inverse probability, i.e. the probability of $\mathbf{G}$ given $\mathbf{A}$, which can be estimated. In general the Bayes' theorem for two events a and b and their joint probability reads

$$P(a, b) = P(a)P(b|a) = P(b)P(a|b), \tag{2.71}$$

which for our case can be rewritten as

$$P(\mathbf{A}|\mathbf{G}) = P(\mathbf{G}|\mathbf{A})P(\mathbf{A})/P(\mathbf{G}). \tag{2.72}$$

As seen in the above equation, to achieve the so called *posterior probability* $P(\mathbf{A}|\mathbf{G})$, there are two functions which are of importance: the *likelihood function* $P(\mathbf{G}|\mathbf{A})$ and the *prior probability* $P(\mathbf{A})$. Since one set of QMC data are used at each time, the third function $P(\mathbf{G})$ in the denominator of Eq. 2.72 is a constant and may be considered as a normalization term.

Prior probability: In our case and based on the argument by Skilling [63], the prior probability is a positive-definite function which can be normalized and is proportional to $\exp(\alpha S)$ with S being the entropy defined relative to a positive-definite function $m(\omega)$

$$\begin{aligned} S &= \int d\omega[A(\omega) - m(\omega) - A(\omega)\ln(A(\omega)/m(\omega))], \\ S &\approx \Delta\omega \sum_{i=1}^{M} A_i - m_i - A_i \ln(A_i/m_i), \end{aligned} \tag{2.73}$$

here $S^{AB}(\omega)$ is replaced by $A(\omega)$ not to be confused with the entropy S. The second equation is valid under the condition that the frequency axis is divided into M equal parts. So the prior probability is a function of two parameters $m(\omega_i)$ which is called the default model and α which is a regularization parameter. The default model expresses prior information that we know about the solution. Although choosing a suitable default model can impact the results and the procedure of obtaining the results, the obtained spectrum is practically almost independent of the default model given that we have precise QMC data. The choice of α can however highly affect the spectrum which will be discussed later in this section. Thus probability $P(\mathbf{A})$ can be alternatively written as

$$P(\mathbf{A}|m,\alpha) \propto \exp(\alpha S) \tag{2.74}$$

Likelihood function: To obtain the form of the likelihood function, we assume that the QMC data are Gaussian-distributed. This assumption is valid when the number of repeated measurements of QMC is large enough and each of these measurements is independent of the others or in other words their correlations are very small. These correlations usually exist between adjacent measurements and therefore can be removed by common analysis such as rebinning, as discussed in section 2.4 by introducing bins of data and averaging over practically uncorrelated bins. The elements of the covariance matrix for N_B number of bins can be written as

$$C_{ij} = \frac{1}{N_B(N_B-1)} \sum_{k=1}^{N_B} (G_i^k - \bar{G}_i)(G_j^k - \bar{G}_j), \tag{2.75}$$

where i and j count the elements of the k-th bin of $\mathbf{G}$ vector and $\bar{G}$ indicate the average value of each element of the bins. If C is not a diagonal matrix, it has to be diagonalized

using a transformation matrix. Then for a diagonal C matrix the likelihood function reads

$$P(\mathbf{G}|\mathbf{A}) \propto \exp(-\chi^2/2), \tag{2.76}$$

where

$$\chi^2 = \sum_{i=1}^{N} \left(\frac{G_i - \sum_j K_{i,j} A_j}{\sigma_i} \right)^2, \tag{2.77}$$

and σ_i^2's are the diagonal elements of the C matrix. $K_{i,j}$'s are the elements of the kernel matrix and A_j's indicate the values of the initial vector for the spectrum.

Knowing the prior and likelihood functions, our problem of finding the maximum posterior probability

$$P(\mathbf{A}|\mathbf{G}) \propto \exp(\alpha S - \chi^2/2) \tag{2.78}$$

decreases to finding a maximum for the term $Q(\mathbf{A}) = \alpha S - \chi^2/2$. It is worth noting that each of the prior, likelihood, and consequently the posterior functions has to be properly normalized [64, 65].

2.5.3. Selection of α

If we set χ^2 to a fixed value, for a large α the dominant term in maximization process is owned by the entropy and the data can not largely deviate from the default model while for a small α, the χ^2 function dominates and the solution is determined mostly by the error of QMC data. Therefore it is crucial to select a reasonable α which balance between the two extreme limits. Here we explain three different approaches to choose this parameter an discuss their efficiency.

Historic solution: In this case, α is simply taken such that $\chi^2 = N$ [66] which can be derived from the fact that the misfit between the original data and the data corresponding to the evaluated spectrum is of the order of standard deviations. This means that the values of the term $G_i - \sum_j K_{i,j} A_j$ are with the same order of magnitude as the deviations σ_i. α obtained from this method depends on the estimated uncertainties σ_i rather than the data themselves which might not be a good idea because the estimation of uncertainties is relatively more difficult than the data.

Classic solution: Another method to set α is to maximize the probability $P(\alpha|\mathbf{G}, m)$ with respect to $\mathbf{A}$ in order to find the most probable spectrum [63, 65, 67]. This probability is defined as

$$P(\alpha|\mathbf{G}, m) = \int d^N\mathbf{A}\; P(\mathbf{A}, \alpha|\mathbf{G}, m), \tag{2.79}$$

where

$$\begin{aligned} P(\mathbf{A},\alpha|\mathbf{G},m) &= P(A|\mathbf{G},m)P(\alpha) \\ &\propto \exp(\alpha S-\chi^2/2)P(\alpha). \end{aligned} \tag{2.80}$$

The prior probability $P(\alpha)$ can be taken either as a constant or as a scale invariant form called Jeffry's prior $P(\alpha)=1/\alpha$ [68]. Therefore we have

$$P(\alpha|\mathbf{G},m)\propto\int d^N\mathbf{A}\exp(\alpha S-\chi^2/2)/\alpha. \tag{2.81}$$

Now if we expand the exponential term in the integrand around the maximum of $Q(\mathbf{A})=\alpha S-\chi^2/2$

$$\exp(\alpha S-\chi^2/2)\approx\exp\{Q(\hat{\mathbf{A}})+\frac{1}{2}\delta\mathbf{A}^T\{\frac{1}{2}\nabla\nabla\chi^2|_{\hat{\mathbf{A}}}-\alpha/\hat{\mathbf{A}}\}\delta\mathbf{A}\}, \tag{2.82}$$

where $\hat{\mathbf{A}}$ is supposed to be the Maximum of $Q(\mathbf{A})$. Performing the integral in Eq. 2.81, the probability can be written as

$$P(\alpha|\mathbf{G},m)\propto\prod_i\left(\frac{\alpha}{\alpha+\lambda_i}\right)^2\exp(\alpha S-\chi^2/2), \tag{2.83}$$

where λ_i's are the eigenvalues of $\frac{1}{2}\{\mathbf{A}^{1/2}\}\nabla\nabla\chi^2|_{\hat{\mathbf{A}}}\{\mathbf{A}^{1/2}\}$. Now the probability $P(\alpha|\mathbf{G},m)$ is maximized with respect to α,

$$\frac{\partial\log P(\alpha|\mathbf{G})}{\partial\alpha}=0, \tag{2.84}$$

which leads to

$$-2\hat{\alpha}S\approx\sum_i\frac{\lambda_i}{\hat{\alpha}+\lambda_i}. \tag{2.85}$$

For large $-2\hat{\alpha}S$ or equivalently when the eigenvalues λ_i's are larger than α , the probability $P(\alpha|\mathbf{G})$ is sharply peaked at $\alpha=\hat{\alpha}$ and the approximation is very well justified. It is worth noting that unlike the historic maximum entropy where the value of χ^2 was involved when choosing α, in the classic solution, the selection of α is completely independent of the corresponding χ^2 value.

Bryan solution: The solution suggested by Bryan was to consider a range of α's instead of a single one in the classic solution and average over their probability contribution to the spectrum [69]. This method is useful when the probability $P(\alpha|\mathbf{G})$ is a broad distribution in terms of α which means that one particular value of α can not represent the mean.

Thus

$$\langle \mathbf{A} \rangle = \int d\alpha \mathbf{A}(\alpha) P(\alpha|\mathbf{G}, m). \tag{2.86}$$

For very precise and completely uncorrelated data, one expect almost identical results generated by these three different methods but for a less precise set of data the Bryan method produces more reasonable results.

2.5.4. Bryan algorithm

To perform each of the methods described for the maximum entropy problem, one needs to use a very efficient and fast numerical algorithm. One of the common algorithms is the Bryan's which is distinguished from its predecessors due to its highly reduced and optimized variable space [65]. A comparison between this algorithm and another one known as Meshkov's algorithm [70] has been made in Ref. [50], where it is shown that while both algorithms generate almost the same results, the Brayan's is much faster specially for higher spectral resolution.

In Bryan's algorithm, the minimization of $Q(\mathbf{A})$ has been taken with respect to $\mathbf{A}$ in the following way. For the entropy we have

$$(\nabla S)_j = \frac{\partial}{\partial A_j} \sum_{i=1}^{N} [A_i - m_i - A_i \ln(\frac{A_i}{m_i})] = -\ln(\frac{A_j}{m_j}), \tag{2.87}$$

and for the gradient of χ^2

$$\nabla(\frac{\chi^2}{2}) = \frac{1}{2} K^T \frac{\partial \chi^2(\mathbf{G}, K\mathbf{A})}{\partial (K\mathbf{A})} \tag{2.88}$$

To decrease the variable space of possible solutions which is usually too large, Bryan has performed a singular-value decomposition (SVD) of the kernel K with the definition $K = V\Sigma U^T$ where U and V are orthogonal matrices and Σ is a diagonal matrix. Performing SVD on K, one obtains $K^T = U\Sigma V^T$ where the diagonal elements of Σ are ordered from largest to smallest. The smallest elements are practically zero and therefore can be neglected. This leads to a reduced space called *singular space* in which the computational calculations are faster. Considering such a space defined using a truncation order of matrix elements and combining Eqs. 2.87 and 2.88, we have

$$-\alpha \ln\left(\frac{\mathbf{A}}{\mathbf{m}}\right) = \frac{1}{2} U^c \Sigma^c (V^c)^T \frac{\partial \chi^2(\mathbf{G}, K\mathbf{A})}{\partial (K\mathbf{A})}, \tag{2.89}$$

where the superscript c indicates the cutoff order corresponded to the singular space. One can expand the solution $\mathbf{A}$ in terms of the elements of the U matrix because the vector spaces of K^T and U are the same. Thus

$$A_j = m_j \exp(\sum_{i=1}^{N_c} U_{ji}^C u_i). \tag{2.90}$$

Now $\mathbf{u} = (u_1, ..., u_{N_c})$ contains the solution defined by $\nabla Q = 0$ and the search must be limited to this space. Inserting the expansion of $\mathbf{A}$ into Eq. 2.89, one obtains

$$-\alpha U^c \mathbf{u} = \frac{1}{2} U^c \Sigma^c (V^c)^T \frac{\partial \chi^2(\mathbf{G}, K\mathbf{A})}{\partial (K\mathbf{A})}, \tag{2.91}$$

which can be simplified as

$$-\alpha \mathbf{u} = \frac{1}{2} \Sigma^c (V^c)^T \frac{\partial \chi^2(\mathbf{G}, K\mathbf{A})}{\partial (K\mathbf{A})} \equiv \mathbf{g}. \tag{2.92}$$

To find the solution in the singular space using this equation, a Newton-Raphson method is used starting from and arbitrary $\mathbf{u}$ with the increment of $\mathbf{u}^{n+1} = \mathbf{u}^n + \delta\mathbf{u}$ at each iteration and the following relation

$$(\alpha I + \partial \mathbf{g}/\partial u)\delta u = -\alpha u - \mathbf{g}, \tag{2.93}$$

where I is the identity matrix and

$$\begin{aligned} \frac{\partial \mathbf{g}}{\partial \mathbf{u}} &= \frac{1}{2} \Sigma^c (V^c)^T \frac{\partial^2 \chi^2(\mathbf{G}, K\mathbf{A})}{\partial (K\mathbf{A})^2} \frac{\partial (K\mathbf{A})}{\mathbf{A}} \frac{\partial \mathbf{A}}{\partial \mathbf{u}} \\ &= \frac{1}{2} \Sigma^c (V^c)^T \frac{\partial^2 \chi^2(\mathbf{G}, K\mathbf{A})}{\partial (K\mathbf{A})^2} V^c \Sigma^c (U^c)^T diag\mathbf{A} U^c \\ &= MD, \end{aligned} \tag{2.94}$$

with

$$\begin{aligned} M &= \frac{1}{2} \Sigma^c (V^c)^T \frac{\partial^2 \chi^2(\mathbf{G}, K\mathbf{A})}{\partial (K\mathbf{A})^2} (V^c) \Sigma^c \\ D &= (U^c)^T diag\mathbf{A} U^c. \end{aligned} \tag{2.95}$$

Collecting all these substitutions in Eq. 2.93 and applying a matrix inversion we are left with

$$\delta \mathbf{u} = -(\alpha I + MD)^{-1} (\alpha \mathbf{u} + \mathbf{g}). \tag{2.96}$$

To keep the algorithm stable we must restrict $\delta\mathbf{u}$ in size. This is done by adding another parameter μ in the equation

$$\delta\mathbf{u} = -((\alpha+\mu)I + MD)^{-1}(\alpha\mathbf{u} + \mathbf{g}) \tag{2.97}$$

so that the step length remains below a limit

$$\delta\mathbf{u}^T D\delta\mathbf{u} \leqslant \sum_i m_i. \tag{2.98}$$

This guarantees that the search is within the range of validity of a local quadratic expansion of Q. Moreover the convergence criteria is defined as follows

$$\frac{Q_n - Q_{n-1}}{Q_n} < \epsilon, \tag{2.99}$$

where ϵ is a small number that we usually set it to 10^{-7}.

2.6. Summary

We introduced the quantum Monte Carlo method based on a stochastic series expansion and its implementation for the spin-1/2 XXZ model . In this context, we explained the concept of vertices, their representation and different types of updating the quantum configurations. We showed how the static and dynamic quantities can be obtained using the method and discussed the importance of careful and reliable statistical error analysis. We also represented the analytical continuation problem and its numerical solutions including different types of maximum entropy methods and the very efficient Bryan algorithm.

3. Transport in spin-1/2 Heisenberg chain

Recently, transport and dynamic properties of low-dimensional systems has attracted much attention. The antiferromagnetic spin-1/2 chain as a prototype model has been at the focus of intense theoretical as well as experimental studies, however a complete understanding of its transport has not been achieved yet. A long standing question in this area is whether spin transport at finite temperature is ballistic or diffusive. In this chapter, we will address this question using a combination of QMC, ED calculations, and results from perturbative bosonization.

The organization of this chapter is the following. In section 3.1, we explain some basic terms and concepts which are needed for our discussion of transport. Then we discuss main challenges or controversial aspects of spin transport in spin-1/2 XXZ chain by giving a literature review of the topic in section 3.2. In section 3.3, we introduce a method through which one can evaluate the spin current relaxation rate of the chain at finite frequency, small momentum and finite temperature. Then, the main results and discussions are split threefold. In section 3.4, we investigate finite temperature spin transport of the isotropic Heisenberg chain by looking at the spin current relaxation rate. The section discusses a finite size scaling of the results, an ED analysis, and checking for an anomalous diffusion. We also show our results for magnetic field and anisotropy dependence of the relaxation rate in sections 3.5 and 3.6, respectively, and finally we give a brief summary in section 3.7

3.1. Basic principles

In this section, several basic principles and concepts which will be used throughout this chapter are clarified.

3.1.1. Linear response theory

Many of transport studies are explained in the framework of linear response theory [71, 72]. This theory describes conductivities of a system in terms of finite temperature dynamic correlation functions calculated at thermodynamic equilibrium. As the name suggests, a linear response to a small external perturbation in the system is taken as an approximation to the whole response. The conductivity can be spin, heat or electric conductivity of an arbitrary model and the perturbation can be induced by external forces on the system such as magnetic field, electric field or temperature gradient. Here we discuss the spin transport of the Heisenberg chain which can be generated by a magnetic field gradient.

For a system in equilibrium described by a time-independent Hamiltonian, H_0, the expected value of the operator A is evaluated as

$$\langle A\rangle = Tr[\rho A] = \frac{1}{Z}\sum_n \langle n|A|n\rangle e^{-\beta E_n}, \tag{3.1}$$

where Z is the partition function, $\beta = 1/K_B T$, and ρ is the density operator which is written in terms of a complete set of eigenvalues E_n and eigenstates $|n\rangle$ of the Hamiltonian H_0. Applying an external perturbation at the time $t = t_0$, the perturbed Hamiltonian reads

$$H(t) = H_0 + H^{'}(t)\theta(t - t_0). \tag{3.2}$$

To obtain the expected value of the operator A at the time t where $t > t_0$, one can use the time evolution of the eigenstates of the unperturbed Hamiltonian $|n(t)\rangle$. Thus, we have

$$\langle A(t)\rangle = Tr[\rho A] = \frac{1}{Z}\sum_n \langle n(t)|A|n(t)\rangle, \tag{3.3}$$

where

$$i\partial_t|n(t)\rangle = H(t)|n(t). \tag{3.4}$$

Using the interaction picture representation $|\hat{n}(t)\rangle$, one can write the time dependence of the eigenstates as

$$|n(t)\rangle = e^{-iH_0 t}|\hat{n}(t)\rangle = e^{-iH_0 t}U(t, t_0)|n\rangle. \tag{3.5}$$

If the perturbation is weak, one can approximate $U(t, t_0)$ by the first order approximation as

$$U(t, t_0) \approx 1 - i\int_{t_0}^{t} dt^{'} H^{'}(t^{'}). \tag{3.6}$$

Inserting this in Eq. 3.3, the time-dependent expected value of the operator A up to the first order is given by

$$\langle A(t)\rangle = \langle A\rangle_0 - i\int_{t_0}^{t} dt^{'}\frac{1}{Z}\sum_n e^{-\beta E_n}\langle n|[A(t), H^{'}(t^{'})]|n\rangle. \tag{3.7}$$

This is a general form of the Kubo formula which represents the linear response of an arbitrary model to a weak perturbation. It is often more convenient to use the Kubo formula in frequency domain. To do so, we apply a Fourier transform of general form

$$A(\omega) = \int_{-\infty}^{\infty} dt e^{-i\omega t}A(t), \tag{3.8}$$

to Eq. 3.7. For the Heisenberg chain with the Hamiltonian $H_0 = J\sum_l[\Delta S_l^z S_{l+1}^z + (S_l^+ S_{l+1}^- + S_l^- S_{l+1}^+)/2]$, if we suppose that the spin current is induced by a space- and time-dependent magnetic filed in the z-direction, $B_l^z(t)$, the perturbation term in Eq. 3.7 can be written as

$$H^{'}(t) = -\sum_l S_l^z h_l^z(t) \tag{3.9}$$

where S_l^z is the local spin density and $h_l^z(t) = g\mu_B B_l^z(t)$. Using the Kubo formula in frequency domain and the lattice continuity equation of the local spin density S_l^z

$$\frac{\partial S_l^z}{\partial t} + \nabla j_l = 0 \tag{3.10}$$

where $j_l = -\frac{iJ}{2}(S_l^+ S_{l+1}^- - S_l^- S_{l+1}^+)$, the spin conductivity $\sigma(\omega)$ is defined as the linear response of the spin current to the frequency-dependent magnetic field gradient $\nabla B^z(\omega)$

$$\langle j(\omega)\rangle = -\sigma(\omega)\nabla B^z(\omega). \tag{3.11}$$

It is worth noting that here the long wavelength limit, $q = 0$, has been considered. Following Refs. [72–74], the real part of the frequency-dependent conductivity $\sigma(\omega)$ can be written as

$$\mathrm{Re}[\sigma(\omega)] = 2\pi D\delta(\omega) + \sigma_{reg}(\omega), \tag{3.12}$$

where D is the Drude weight

$$D = \frac{\beta}{L}\sum_{\substack{m,n \\ E_m = E_n}} e^{-\beta E_m}|\langle m|j|n\rangle|^2, \tag{3.13}$$

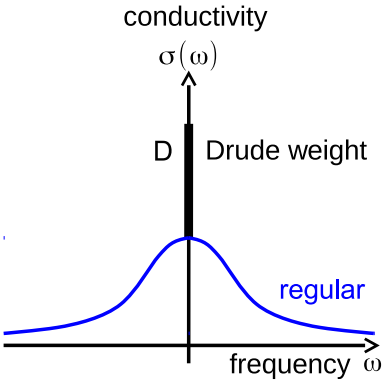

Figure 3.1.: The sketch of the sharp peak of Drude weight D at zero frequency shown as the black bar and the Lorentzian form of regular conductivity as a function of frequency (the blue curve).

and σ_{reg} is the regular part of the conductivity

$$\sigma_{reg}(\omega) = \frac{1 - e^{-\beta\omega}}{\omega} \frac{\pi}{L} \sum_{\substack{m,n \\ E_m \neq E_n}} e^{-\beta E_m} |\langle m|j|n\rangle|^2 \delta(\omega - E_n + E_m). \tag{3.14}$$

where the operator j is defined as $j = \sum_l j_l$. In Fig. 3.1, an sketch of the two types of conductivity in terms of frequency is illustrated where the peak function at zero frequency is the Drude weight and the Lorentzian shape function is the regular part of conductivity. This latter one is of our interest and specially the width of the Lorentzian function which is characterized as the spin current relaxation rate is in detail discussed in this chapter. We will show how this relaxation rate can be determined by the imaginary part of the Fourier transformed time-ordered spin-spin correlation functions. Several studies have been carried out to obtain this contribution to the conductivity which however are not in a complete consistency [26, 28, 75, 76]. Direct calculation of the Drude weight D is not an easy issue, however there are expressions for that in the literature which are usually limited by some technical difficulties. One can use the optical sum rule [77–79] or the Kohn formula [80] and its generalization at finite temperature [81, 82], in order to get an estimate of D. For the optical sum rule, one needs to have the value of all current matrix elements and in the case of Kohn formula, the difficulty is to estimate the finite size energy corrections [73]. Nevertheless, another efficient approach is to use a type of inequality instead of the exact expression for the Drude weight, by introducing a lower bound for the Drude weight. Such an inequality has been suggested by Mazur and Suzuki [83, 84] and has the advantage that it does not require the calculation of dynamical

correlation functions and is thus much more accessible by standard techniques [27].

3.1.2. Mazur's inequality

According to Mazur's inequality, the time decay of correlations can be related to the local conserved quantities Q_n of a Hamiltonian system

$$lim_{t'\to\infty}\frac{1}{t'}\int_0^{t'}\langle A(t)A\rangle \geq \sum_n \frac{\langle AQ_n\rangle^2}{\langle Q_n^2\rangle}, \qquad \langle Q_m Q_n\rangle = \langle Q_n^2\rangle\delta_n, m, \tag{3.15}$$

where $\langle \dots \rangle$ denotes thermodynamic average. In other words, it is shown that conservation laws can lead to non-decaying correlation functions and consequently a finite current at the long-time limit. It must be noted that a local conserved quantity is defined as $Q_n = \sum_j q_j^n$, where q_j^n is a density operator acting on n adjacent sites j. In the case of spin-1/2 Heisenberg chain where the spin-current density operator is defined from the continuity equation for the density of the globally conserved spin component

$$\partial_t S_l^z = -i[S_l^z, H] = -(j_l - j_{l-1}), \tag{3.16}$$

with

$$j_l = -\frac{iJ}{2}(S_l^+ S_{l+1}^- - S_{l+1}^+ S_l^-),\ \mathcal{J} = \sum_l j_l, \tag{3.17}$$

the Mazur's inequality can provide a lower bound for the Drude weight by

$$D \geq D_{\text{Mazur}} \equiv \frac{1}{2LT}\frac{\langle \mathcal{J}\mathcal{J}_E\rangle^2}{\langle \mathcal{J}_E^2\rangle}, \tag{3.18}$$

where energy current $\mathcal{J}_E$ is the simplest nontrivial conserved quantity

$$\begin{aligned}\mathcal{J}_E &= J^2\sum_l [S_{l-1}^y S_l^z S_{l+1}^x - S_{l-1}^x S_l^z S_{l+1}^y \\ &+ \Delta(S_{l-1}^x S_l^y S_{l+1}^z - S_{l-1}^z S_l^y S_{l+1}^x) \\ &+ \Delta(S_{l-1}^z S_l^x S_{l+1}^y - S_{l-1}^y S_l^x S_{l+1}^z)].\end{aligned} \tag{3.19}$$

As shown in Eq. 3.18, in order to have a finite Drude weight, two conditions have to be fulfilled, first there must exist local conserved quantities in the system and second the overlap of the spin current with the conserved quantities must be finite. The existence of conserved quantities can be discussed in the context of integrability.

3.1.3. Integrability

The definition of integrability for a classical system was first proposed by Liouville [85] and therefore the notion of Liouville-integrability refers to a system with $2N$-dimensional phase space which has N constants of motion Q_n. In the classical limit the constants of motions are recognized by a zero Poisson bracket with the Hamiltonian as well as other constants

$$\{H, Q_n\} = 0, \qquad \{Q_m, Q_n\} = 0. \tag{3.20}$$

Only the existence of these constants is enough to demonstrate the system as integrable, while solving equations of motion is another issue. An analogous definition of classical integrability for quantum systems can be given by considering Q_n's as conserved quantities, $[H, Q_n] = 0$. and substituting Poisson brackets with mutually commutators between these conserved quantities, $[Q_n, Q_m] = 0$.

Quantum systems in one dimension and at low temperatures can be often described as integrable models plus some small perturbations. In statistical mechanics, quantum integrable systems are often referred to as models which can be exactly solved using the Bethe ansatz approach. One example is the XXZ model where all of its eigenstates are explicitly obtained by Bethe ansatz. In the context of transport, we are especially interested in the relation between integrability and transport properties of low-dimensional spin systems. Many studies have been devoted to this relation and specially to the question of ballistic or diffusive regime of transport for integrable and non-integrable systems (see Ref. [27] and references therein).

3.2. Controversial aspects

As it was already discussed the transport properties of a model are strongly connected to the conservation laws and the integrability of the system. Based on these concepts, here, the discussion of transport is addressed for our example, i.e. the spin-1/2 XXZ chain. A main question in this context is whether an integrable system holds a non-decaying spin current. It has been conjectured that the Drude weight $D(T > 0)$ should be finite for integrable models while it vanishes in the case of nonintegrable ones [75, 81]. A finite Drude weight implies an infinite *dc* conductivity resulting in a ballistic transport while in the diffusive behavior of the system, the current decays as the time goes to infinity. For the case of XXZ chain which is an integrable model, although a finite Drude weight has been calculated exactly by Bethe ansatz (BA) at zero temperature [77], there are contradicting scenarios in the case of finite temperatures.

Thermodynamic BA (TBA) [86] suggests a finite Drude weight at $T > 0$ which decreases monotonically with T for the XXZ chain in the critical regime ($|\Delta| < 1$) and zero magnetic field. This method however predicts a vanishing Drude weight at the isotropic point. An alternative BA calculation proposed by Benz *et al.* which is based on spinon and antispinon particles has predicted a diverging $D(T > 0)$ with a different temperature dependence so that near the isotopic point it is an increasing function of temperature. Nevertheless both of these methods violate the exact relation of the Drude weight at high temperatures [27, 86] .

There are also several numerical and analytical studies showing a finite Drude weight at $T > 0$. In Refs. [87–89], an exact diagonalization method has been used to indicate a finite Drude weight in the critical regime of XXZ chain including the isotropic point. In Ref. [90] however it has been suggested that the transport is ballistic in the gapless regime, anomalous at the isotropic point and diffusive in the gapped regime. Some of the studies have used the argument of integrability conjecture using the Mazur's inequality to indicate a lower bound for the Drude weight and establish a ballistic transport [75, 81, 91–96].

Moreover a QMC approach has been applied to obtain the Drude weight by doing an analytic continuation of the conductivity in terms of Matsubara frequencies [97–99]. At high temperatures, other methods including Lanczos method [100, 101] and Master equation [102, 103] have predicted a ballistic transport in the gapless regime and a diffusive one in the gapped regime.

However the spin diffusion has been experimentally observed in spin-1/2 chain compounds using NMR [104, 105] and muon spin resonance [106] with a large diffusion constant. This is not consistent with the conjecture of ballistic transport in integrable systems. The existence of a diffusive behavior in XXZ chain has been supported analytically by a field theory approach based on bosonization [26] and confirmed by DMRG calculations [27] and a comparison to NMR experiment on Sr_2CuO_3 [104]. The recent QMC results have approved that there exists a diffusive transport for XXZ chain at finite temperature and the isotropic point [28]. It has been also suggested that the ballistic and diffusive transports can principally coexist [26, 27, 107, 108] such that these two channels of transport compete for spectral weight of the spin-spin correlation functions. This means that there can be a diffusive transport while the Drude weight is finite.

3.3. Method of analysis

The Hamiltonian of the antiferromagnetic spin-1/2 XXZ chain at finite magnetic field is given by

$$H = J\sum_{l}\left[\Delta S_l^z S_{l+1}^z + \frac{1}{2}(S_l^+ S_{l+1}^- + S_l^- S_{l+1}^+)\right] - h\sum_i S_i^z, \tag{3.21}$$

where $J > 0$ is the exchange coupling constant, $S_l^{z,\pm}$ are spin-1/2 operators on site l, Δ is the exchange anisotropy and h is the longitudinal magnetic field. As discussed in the linear response theory, the zero momentum frequency dependent optical conductivity can be described as

$$\mathrm{Re}[\sigma(\omega)] = 2\pi D\delta(\omega) + \sigma_{reg}(\omega), \tag{3.22}$$

where D is the Drude weight and σ_{reg} is the regular spectrum of conductivity. The main goal here is to study the regular part of the conductivity using a combination of results from a perturbation theory (PT) based on bosonization and the very accurate results obtained from QMC. The QMC data have been obtained using directed loop algorithm based on the stochastic series expansion (SSE) method [48].

The method which is used to study the regular conductivity of the model has been very well described in Refs. [27, 28]. Here we just mention the main points and try to be brief. In principle one can relate σ_{reg} to the imaginary part of the retarded spin susceptibility $\chi\,(q,\omega)$ using the continuity equation. Thus, we have

$$\sigma_{reg} = \lim_{q\to 0}\frac{\omega}{\pi q^2}\mathrm{Im}[\chi\,(q,\omega)]. \tag{3.23}$$

However, the spin susceptibility obtained from the SSE method is in imaginary time domain, $\chi(q,\tau)$. In order to obtain the real-frequency spin susceptibility, one way is to use analytical continuation methods as described in chapter 2 which are usually accompanied by hard-controllable sources of error. Here, however, we apply a method in which instead of transforming $\chi(q,\tau)$ into frequency space, we use an approximate expression obtained from a perturbative method based on bosonization [109, 110] for the low-energy and long-wavelength spin susceptibility in the frequency space

$$\chi_{ret}\,(q,\omega) = \frac{-Kvq^2/2\pi}{\omega^2 - v^2q^2 - \Pi^{\mathrm{ret}}(q,\omega)}, \tag{3.24}$$

where $\Pi^{\mathrm{ret}}(q,\omega)$ is the self-energy and can be approximated to the second order of Umklapp scattering and to the first order of the band curvature perturbations [111] and therefore

$$\Pi^{\mathrm{ret}}(q,\omega) \approx -2i\gamma\omega - b\omega^2 + cv^2q^2. \tag{3.25}$$

This expression can be transformed onto imaginary-time domain where the QMC data

are extremely exact. By inserting the self-energy into $\chi(q,\omega)$, the general form of the spin susceptibility can be rewritten as

$$\chi_{ret}(q,\omega) = \frac{-Kvq^2/(2\pi)}{(1+b)\omega^2 - (1+c)v^2q^2 + 2i\gamma\omega}, \tag{3.26}$$

where K is the Luttinger parameter, v is the spin velocity and γ is the spin current relaxation rate. Our main concern in this chapter is to evaluate these three parameters and find out the behavior of them in terms of different system parameters. Among them the relaxation rate γ is of more interest because it gives us an estimate of the diffusion in the system such that a finite γ implies the existence of a diffusive channel in transport while a zero γ corresponds to a pure ballistic transport. For very small ω, we have $\omega^2 \to 0$ and therefore Eq. 3.26 has a diffusion pole with a diffusion constant $\Gamma = (1+c)v^2/(2\gamma)$. We must also note that the finite width of the spectral function $\chi''(q,\omega) = \mathrm{Im}[\chi_{ret}(q,\omega)]/\pi$, which is dominantly set by the two-spinon continuum, has not been incorporated in Eq. 3.26. This width is however negligible in the limit of our interest, $q \ll 1$.

The parameters γ, b and c have been obtained by perturbative theory [26]. In the anisotropic case, $-1 < \Delta < 1$, the parameters are given by

$$\begin{aligned} 2\gamma &= Y_1 T^{4K-3}, \\ b &= \underbrace{(Y_2 - Y_3)T^{4K-4}}_{b_2} + \underbrace{Y_4 T^2}_{b_1}, \\ c &= \underbrace{-(Y_2 + Y_3)T^{4K-4}}_{c_2} \underbrace{-Y_4 T^2}_{c_1}. \end{aligned} \tag{3.27}$$

Here b_1 and c_1 (b_2 and c_2) are the parts stemming from the band curvature (Umklapp) terms, respectively. The spin velocity v and Luttinger parameter K are taken from zero temperature Bethe Ansatz and

$$\begin{aligned} Y_1 &= \Lambda \frac{B(K,1-2K)}{\sqrt{\pi}2^{2K+1}} \cot(\pi K), \\ Y_2 &= \Lambda \frac{B(K,1-2K)}{\pi^{5/2}2^{2K+4}} (\pi^2 - 2\Psi'(K)), \\ Y_3 &= \Lambda \frac{1}{\pi 2^{4K+4}} \cot^2(\pi K)\Gamma(1/2-K)\Gamma(K), \\ Y_4 &= \frac{\pi^2}{6v^2}(\lambda_+ + 6\lambda_-), \\ \Lambda &= 4\pi K\lambda^2 \sin(2\pi K) \left(\frac{2\pi}{v}\right)^{4K-2} \Gamma(1/2-K)\Gamma(K), \end{aligned} \tag{3.28}$$

where $\Psi(x)$ is the Digamma function. At the isotropic point, $\Delta = 1$, Umklapp scattering

becomes negligible and a perturbative power expansion of temperature $T/J \ll 1$ is used to obtain the required parameters. The Luttinger parameter can be replaced by a running coupling constant g, $K \to 1 + g(T)/2$ and the following equations are applied in order to calculate the relaxation rate

$$\begin{aligned} 2\gamma &= \pi g^2 T, \\ b &= \frac{g^2}{4} - \frac{g^3}{32}\left(3 - \frac{8\pi^2}{3}\right) + \frac{\sqrt{3}}{\pi}T^2, \\ c &= \frac{g^2}{4} - \frac{3g^3}{32} - \frac{\sqrt{3}}{\pi}T^2. \end{aligned} \tag{3.29}$$

The running coupling constant $g(T)$ is determined [110] by the equation

$$\frac{1}{g} + \frac{\ln g}{2} = \ln\left[\sqrt{\frac{\pi}{2}}\frac{e^{1/4+\tilde{\gamma}}}{T}\right] \tag{3.30}$$

where $\tilde{\gamma}$ is the Euler constant.

This perturbative method discussed above does not however lead to the exact values of the parameters γ, b and c because of the approximations and simplifications considered in the method. In this chapter, we want to use the very exact QMC data to extract not only the exact values of these three parameters but also those of the Luttinger parameter K and spin velocity v at finite temperatures. This is however only possible in the valid regime of Eq. 3.26, namely only at low temperatures, since we use this equation as our fitting function.

The dynamic susceptibility $\chi_{ret}(q,\omega)$ can be transformed onto imaginary-time axis using the following transformation

$$\chi(q,\tau) = 2\sum_{n=0}^{\infty}\cos(\omega_n\tau)\chi(q,\omega_n) - \chi(q,0), \tag{3.31}$$

with

$$\chi(q,\omega_n) = \frac{K_q v_q q^2/(2\pi)}{(1+b)\omega_n^2 + (1+c)v_q^2 q^2 + 2\gamma_q|\omega_n|}, \tag{3.32}$$

where $\omega_n = 2\pi n T$ are bosonic Matsubara frequencies with integer values of n which have to be summed over. It must be noted that Eq. 3.26 is a valid approximation of the spectrum in the limit where $|\omega \pm vq| \ll T$. However here we assume that it is valid for all values of ω. The zero frequency limit of the dynamic susceptibility $\chi(q,\omega \to 0) = K/(2\pi v(1+c))$ is known to monotonously increase for the Heisenberg model as $q \to \pi/2$. Nevertheless, the momentum dependence of $\chi(q,\omega \to 0)$ in the bosonization approach has not been

taken into account. But we consider this dependence when fitting the QMC data to Eq. 3.31. Therefore, a momentum dependence of $K \to K_q$ and $v \to v_q$ is also allowed. Now by fitting the imaginary time QMC data to Eq. 3.31, the fitted parameters K_q, v_q and γ_q at small momenta can be extracted. In the fitting process, the values of the constants b and c are set to the suggested values from bosonization. However, it is proved that even taking them as fitting parameters would not lead to considerable deviations from those values.

The described method avoids the analytical continuation error and only includes the very small standard statistical errors which can be simply controlled. In the next sections, we will prove the applicability of this approach using various analyses and then we use it for different system parameters of the XXZ model subject to an external magnetic field. One point which has to be kept in mind throughout the next sections of this chapter specially in the legends of figures where the spin current relaxation rate, Luttinger parameter or spin velocity are shown, is that the term *QMC* refers to this method here (QMC data used to extract the fitting parameters) and it is not the original QMC data directly obtained from the code.

3.4. Isotropic chain

This section is a very detailed extension of the previous work [28], which has only been restricted to a single size of the Heisenberg chain at the isotropic point. We do a finite size scaling ($64 < L < 256$) for the model and discuss the role of finite size effects in the determination of the relaxation rate as well as other relevant fitting parameters. In addition to that, we do an ED analysis and show to what extent our approach is consistent with exact results for a finite system size $L = 18$. We go further by checking for an anomalous diffusion kernel where a potential power law frequency dependence of the diffusion kernel is examined.

3.4.1. Finite-size scaling

In Ref. [28], the approach described in section 3.3 has been applied to the isotropic spin-1/2 Heisenberg chain for a single system-size $L = 128$. Here, we extend on this approach to larger system-sizes up to $L = 256$ and show how the system size can affect the results or if at all, there exist any considerable finite size effects. We also investigate a smaller system-size $L = 64$ to see if for smaller systems, there is any deviation from the thermodynamic limit which is the valid limit of the bosoniazation method. The temperatures considered

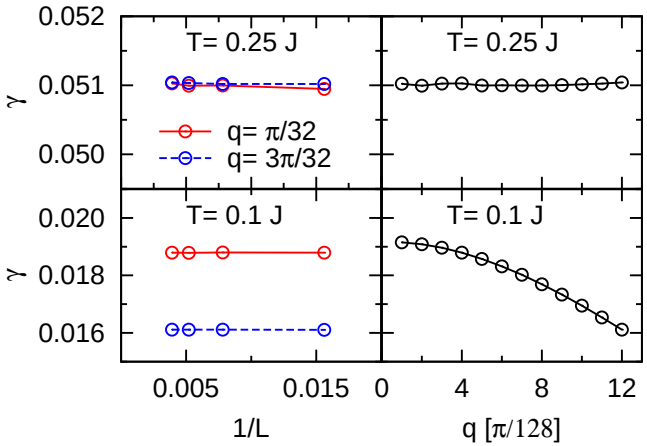

Figure 3.2.: Finite frequency spin current relaxation rate γ of the isotropic Heisenberg spin chain versus momentum q and inverse system size $1/L$, for chain lengths $64 < L < 256$, at two temperatures $T = 0.1J$ and $0.25J$. For momentum dependence of γ, the largest system size $L = 256$ is chosen.

here are $T = 0.1J$ and $T = 0.25J$. As explained in section 3.3, the QMC data can be fitted to Eq. 3.31 by taking the three parameters, the Luttinger parameter K, the spin velocity v and the spin current relaxation rate γ, as fitting parameters. As a result, none of the three parameters is size dependent. Even the weak momentum dependence of γ for the lower temperature $T = 0.1J$ is independent of system-size. In Fig. 3.2 the momentum dependence of γ for a system size $L = 256$ as well as the size dependence of the spin current relaxation rate γ for the range $64 < L < 256$ at two momenta $q = \pi/32$, $3\pi/32$ are shown. Since momentum space for finite system-size is discrete, to do finite size scaling, those wave vectors are chosen which are matched for different sizes and are not necessarily the smallest possible wave vectors of each system-size.

It was speculated [28] that the weak momentum dependence of the scattering rate at $T = 0.1J$ might be because of finite size effects but the finite size scaling shows that it is not the case and this dependence survives at larger and also lower system-sizes. Nevertheless the origin of this dependence is still not clear to us. Momentum dependence of the relaxation rate is also important in the sense that we can extrapolate the relaxation rate when $q \to 0$. In our case the extrapolation shows a finite relaxation rate at both temperatures which proves the existence of a diffusive regime within the valid region of

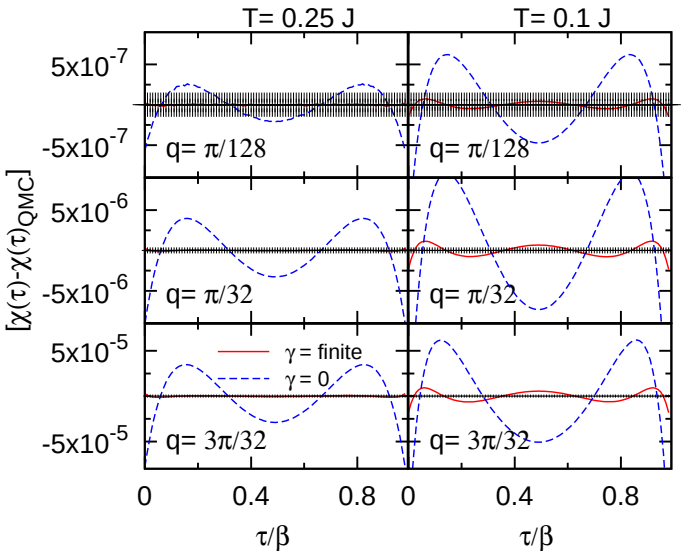

Figure 3.3.: Differences between the fitted curve and the original QMC results at the isotropic point for different wave vectors and temperatures. The system-size considered here is $L = 256$.

bosoniazation.

The authors of the recent paper [101] have obtained the momentum dependence of γ for almost high temperatures using a memory-function formalism. The lowest temperature they have considered is $T = 0.7J$ which is still far away from the valid temperature of bosonization. However for the isotropic spin-1/2 chain, they also found a finite γ at rather small momenta. For the limit $q \to 0$, their results are not conclusive due to the restriction of finite sizes.

To test the accuracy of our fitting procedure, a comparison between QMC data and Eq. 3.31 is shown in Fig. 3.3 for different temperatures and small nonzero wave vectors of a system with 256 sites. Each panel shows the difference between QMC data and equation 3.31 with two γ's, one finite γ as optimized by fitting and another one forced to be zero. The QMC statistical errors are shown as the error bars. There are some points which have to be mentioned. First of all, fitting errors (the difference between QMC data and equation 3.31) are very small, and for the smallest nonzero wave vector $q = \pi/128$, Eq.

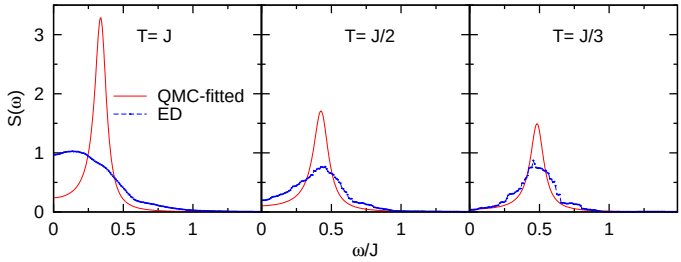

Figure 3.4.: ED and QMC spectra in frequency domain at the isotropic point and chain length $L = 18$ for $q = \pi/9$ and three temperatures $T = J/\{1, 2, 3\}$.

3.31 is identical to QMC data for a finite γ (within the standard deviation of QMC). Moreover, by decreasing the wave vector, the difference becomes smaller which reflects the fact that bosoniazation is valid when $q \to 0$. Even at rather large wave vectors, a finite γ leads to a better consistency with QMC data than $\gamma = 0$ does.

3.4.2. Exact diagonalization analysis

It would be of great interest to test the current method (combination of QMC and bosonization) against other possible methods and establish the degree of consistency between them. One reliable method to study dynamics of low dimensional systems is the exact diagonalization (ED) method, where the time evolution of the correlation functions is obtained from exact eigenvalues and eigenstates of the Hamiltonian (full diagonalization). This method is limited to small system sizes due to exponentially increasing number of states. Moreover, it can not produce a smooth dynamical structure factor (DSF) at low temperatures because of the small population of the excited states and also the stronger effects of finite-size in this limit. However, one can calculate the DSF of a finite system size at intermediate temperatures and see its evolution as temperature decreases. By doing so, the low-temperature excitation spectrum can be speculated.

The DSF for a system with 18 sites and three different temperatures at the smallest nonzero wave vector $q = \pi/9$ is shown in Fig. 3.4. On the one hand, ED is used to obtain the frequency dependence of the DSF (data from Ref. [112]), where the produced spectrum is a collection of peak positions in the frequency axis that correspond to the excited states and what is seen in Fig. 3.4 is a smooth function obtained from sorting peaks into bins of a histogram (by averaging over frequency intervals). On the other

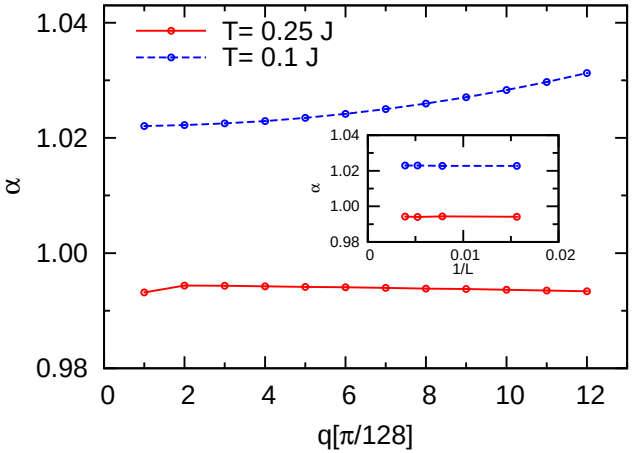

Figure 3.5.: Exponent α of the spin density relaxation rate $\gamma\omega^{\alpha}$ of the isotropic Heisenberg chain versus momentum q at chain length $L = 256$ for two temperatures $T = 0.1J$ and $0.25J$.

hand, the same system size is chosen for QMC simulation and the imaginary time results are fitted to Eq. 3.31. The extracted fitting parameters are inserted into Eq. 3.26 to obtain the DSF in frequency domain. It is worth noting that this inserting of the parameters in Eq. 3.26 does not generate any errors associated with transformations or matrix inversion of the spectral kernel and therefore it is completely different from the analytical continuation methods which are usually accompanied by an error related to the uncertainly of the spectrum. As seen in Fig. 3.4, by decreasing temperature from $T = J$ to $T = J/3$, the consistency between the two methods improves significantly. We believe that if ED method could produce a smooth spectrum at smaller temperatures, this agreement would be even better. Of course at high temperatures, this consistency is not expected because it is not the valid regime of bosonization which means that the comparison in this regime is meaningless.

3.4.3. Anomalous diffusion

So far it was assumed that the general form of the dynamical susceptibility at the special regime of validity can be fully described by Eq. 3.26, where the diffusion kernel was

considered as a frequency independent one. Now, we want to go beyond this assumption and check for an anomalous diffusion kernel. One example of anomalous diffusion has been given in Ref. [90], where the infinite temperature transport of the XXZ chain is anomalous with a diffusion diverging as $\Gamma \sim \sqrt{L}$ where L indicates the system-size.

Here, however, we want to consider the more intuitive guess, namely a power law frequency dependence of the diffusion kernel. To this end, we rewrite Eq. 3.26 as follows

$$\chi_{ret}(q,\omega) = \frac{-Kvq^2/(2\pi)}{(1+b)\omega^2 - (1+c)v^2q^2 + 2i\gamma\omega^{\alpha}}, \tag{3.33}$$

where the power α is included in the diffusion term (in denominator). For small frequencies, we can consider the assumption $\omega^2 \to 0$ in the above equation. This leads to a diffusion pole in the susceptibility with a diffusion kernel $\Gamma = (1+c)v^2\omega^{\alpha-1}/(2\gamma)$. The deviation of α from 1 indicates the frequency dependence of the diffusion and by setting $\alpha = 1$ the former frequency-independent kernel is accessed. So the question here is: what is the value of α and how can it be estimated from QMC data? The answer is to let α be free in the fitting procedure in addition to other parameters and try to optimize the fitting once more.

As a result, it appears that α shows only an infinitesimal deviation from one. This means that the diffusion kernel Γ is independent of frequency. In Fig. 3.5, α versus momentum for the system size $L = 256$ and the two promised temperatures $T = 0.1J$ and $T = 0.25J$ is plotted. In the inset, a finite size scaling of α for a range of system-sizes $64 < L < 256$ and one momentum $q = \pi/32$ is shown. Not only the momentum dependence of α is marginal but it also doesn't depend on the system size. This proves that for the isotropic Heisenberg chain, there is no power law frequency dependence of the diffusion kernel. One can also check for other types of anomaly in the kernel but since the diffusion is size independent either in the standard form or in the power-law one, even if there is an anomaly in diffusion, it would be unlikely a size dependent one.

It is worth noting that by adding α to the free parameters of the fitting process, the values of γ, K, and v might also change. However these changes are very small which implies that the approach is independent of the suggested form of the diffusion kernel.

3.5. Field dependence

In this section, we will extend our approach to the case with a finite magnetic field where the spin rotation invariance is broken. The main concern is to find out the behavior of the spin current relaxation rate as a function of magnetic field. However the Luttinger

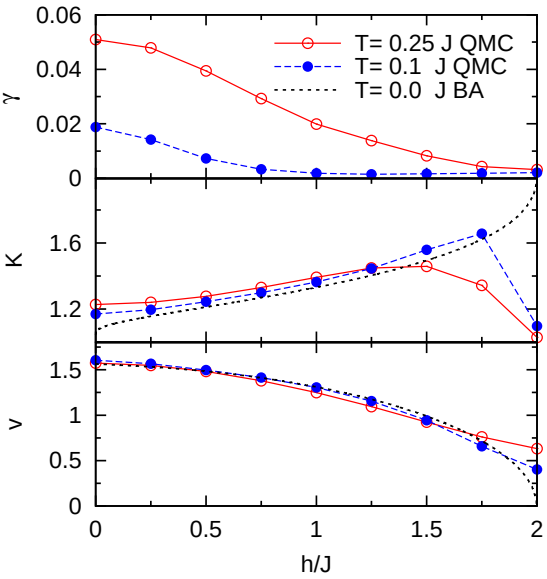

Figure 3.6.: Spin current relaxation rate γ, Luttinger parameter K, and spin velocity v at finite temperatures $T = 0.1,\ 0.25\ J$ obtained from QMC of a chain with 64 sites and Luttinger parameter K and spin velocity v at zero temperature known from BA in terms of magnetic field are shown.

parameter and the spin velocity are also estimated to approve the validity of the method at a finite magnetic field. Here we restrict ourselves to the isotropic chain and considerations of the exchange anisotropy is postponed until the next section.

Again the starting point is Eq. 3.26 and its transformation in imaginary time domain Eq. 3.31. By fitting the longitudinal dynamic structure factor obtained from QMC, the fitting parameters K, v and γ are extracted. The field dependence of these parameters is shown in Fig. 3.6 for two temperatures $T = 0.1J,\ 0.25J$ at wave vector $q = \pi/32$ of a system with 64 sites. For both temperatures the spin current relaxation rate decreases down to almost zero as the magnetic field increases up to the saturation field ($h = 2J$). At the first glance the nonzero relaxation rate at a finite magnetic field seems to contradict the Mazur's inequality [83, 113] due to the fact that for finite magnetic fields there exist conservation laws preserving the Drude weight. It might also conflict the ED calculations of the Drude weight in Ref. [88]. Nevertheless as it was proposed in Refs. [26, 27], a

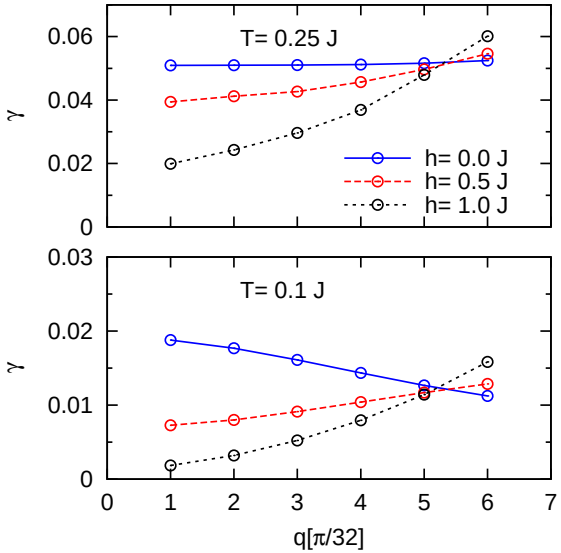

Figure 3.7.: Momentum dependence of the spin current relaxation rate for two temperatures $T = 0.1,\ 0.25\ J$ and different external magnetic fields is plotted. The system-size considered here is $L = 64$.

coexistence of ballistic and diffusive contributions to the transport is possible. This means that a finite spin current relaxation rate does not necessarily imply a zero Drude weight and vice versa.

Another feature shown in Fig. 3.6 is the field dependence of the Luttinger parameter and the spin velocity at finite temperatures which have been compared with those at zero temperature. The latter ones have been exactly obtained from a numerical solution of the Bethe ansatz integral equations [114, 115]. One can clearly see good agreement between finite temperature parameters and the BA results. The small deviation seen close to the saturation field ($h = 2J$) is due to finite temperature and vanishes by decreasing temperature. This agreement with exact results can be interpreted as another proof of the validity of our method at finite magnetic fields.

We are also interested in the momentum dependence of the relaxation rate at small momenta and finite magnetic fields. This is illustrated in Fig. 3.7 for two temperatures

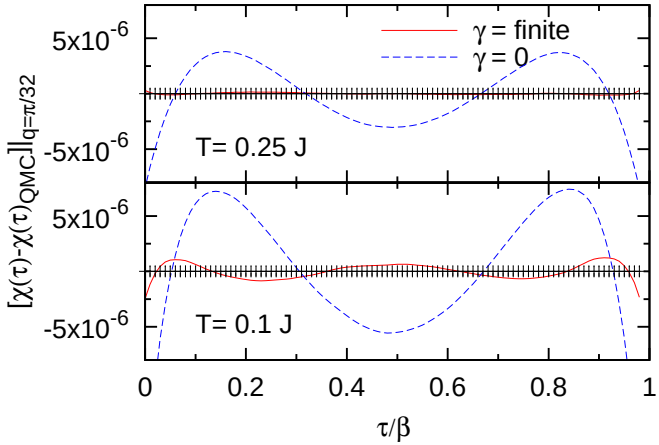

Figure 3.8.: Differences between the fitted curves and original QMC data for $h = 0.25J$ and two different temperatures at momentum $q = \pi/32$. The system-size considered here is $L = 64$.

$T = 0.1$, 0.25 J and three magnetic fields $h = 0$, 0.5, 1.0 J. At finite magnetic fields, the momentum dependence behavior of the relaxation rate changes so that for $h = 0.5$, 1.0 J, we have an increasing function of wave vector while for $h = 0$, it is either a decreasing or a constant function. Nevertheless, still at small magnetic fields the extrapolated value of the relaxation rate is a finite one. By increasing h, the slope of the function increases which leads to a zero relaxation rate at the saturation field and in the limit $q \to 0$. Once more, to make sure that the fitting has been accurately performed, the fitting error (the difference between QMC data and equation 3.31) is tested for the case of a finite magnetic field. As an example, this error for $h = 0.25J$ and two temperatures, $T = 0.1$, 0.25 J, has been plotted in Fig. 3.8. The error of the case in which γ is forced to be zero has been also shown in this figure for comparison. In all cases, the finite γ is associated with smaller errors which are almost within the error bars of QMC data.

3.6. Anisotropy

One of the important and interesting aspects of spin transport in XXZ model is the role of exchange anisotropy Δ, because real materials most likely possess such anisotropy

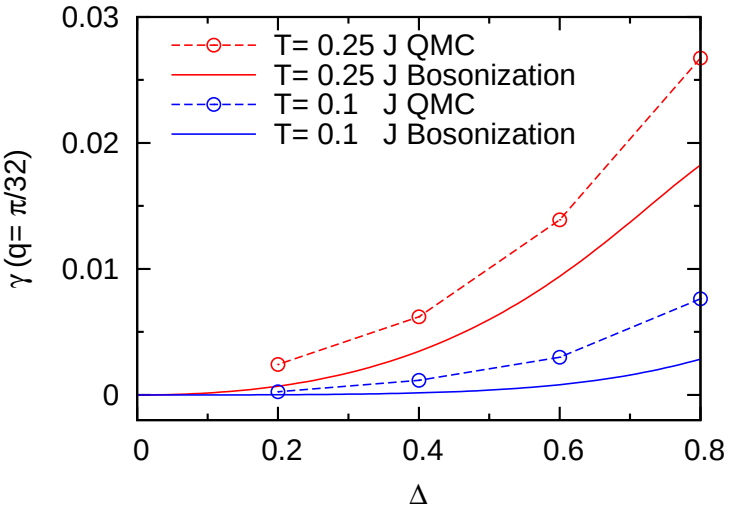

Figure 3.9.: Anisotropy dependence of the spin current relaxation rate obtained from bosonization (solid curves) and our method (symbols) for the first nonzero momentum on a system of 64 sites for two temperatures $T = 0.1, 0.25\ J$. The dashed curve is just a guide to the eyes.

due to the broken rotational symmetry in existence of spin-orbit couplings or dipolar interactions. At zero temperature, it is believed that the transport is ballistic in the critical regime $-1 < \Delta \leq 1$ and a finite Drude weight has been exactly calculated using BA [77]. However, as discussed in section 3.2, different approaches of BA and numerical calculations have not led to a conclusive picture of transport at finite temperatures. In the gapped regime $\Delta > 1$, a diffusive transport has been suggested [116] with a vanishing Drude weight as Δ decreases but the minimum value of anisotropy at which the Drude weight is zero has not been determined.

Here we use our method to obtain the spin current relaxation rate as a function of anisotropy in the region of $0 < \Delta < 1$ and at finite temperatures. We know that for $\Delta = 0$ we have non-interacting spinless fermions, so the scattering rate γ must be zero at this point. But we are yet interested in the behavior of the relaxation rate when $0 < \Delta < 1$. As it is described in section 3.3, a temperature dependence of the relaxation rate has been suggested from bosonization

$$\gamma(T) = f(K, v)T^{4K-3}, \tag{3.34}$$

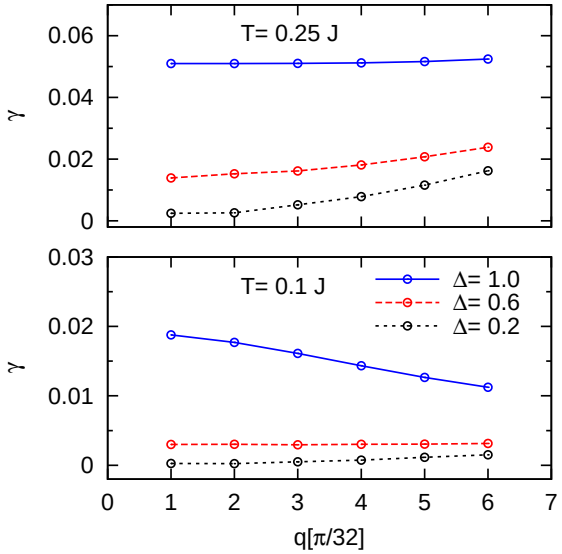

Figure 3.10.: Momentum dependence of the spin current relaxation rate γ for different anisotropies and temperatures of a system with length $L = 64$.

where f is a function of the Luttinger parameter K and the spin velocity v which are exactly known from BA at zero temperature

$$K = \frac{\pi}{\pi - \arccos\Delta}, \; v = \frac{\pi\sqrt{1-\Delta^2}}{2\arccos\Delta}. \tag{3.35}$$

Although at finite temperatures the values of these parameters may deviate from those at zero temperature, it has been assumed that the deviations are small. However while extracting the relaxation rate using QMC data, K and v are considered as free parameters and therefore exactly extracted at finite temperatures.

In Fig. 3.9, the anisotropy dependence of the relaxation rate obtained from both methods, fitted QMC data and bosonization is shown for two temperatures. For QMC data it is plotted for the smallest nonzero wave vector $q = \pi/32$ and at chain length $L = 64$. One can see a good qualitative agreement between the two relaxation rates but for both temperatures the γ obtained from QMC is quantitatively different from that of bosonization. One reason of such a difference might be skipping of some high order terms in the

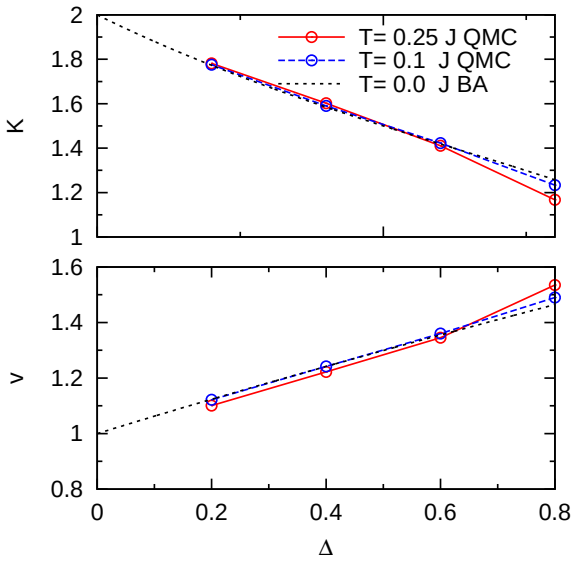

Figure 3.11.: Luttinger parameter and spin velocity at finite temperature obtained from QMC in terms of anisotropy for the first nonzero momentum at chain length $L = 64$ are plotted. Luttinger parameter and spin velocity at zero temperature known from BA are also shown for comparison purposes.

approximations emerged from bosonization.

It appears that the exchange anisotropy in the model plays a similar role as the magnetic field does at the isotropic point in the sense that both parameters lead to a decrease of γ and consequently drive the system to the limit of purely ballistic regime.

The momentum dependence of γ is also shown in Fig. 3.10 at two temperatures $T = 0.1$, $0.25\ J$ for the isotropic point $\Delta = 1$ and two values of anisotropy $\Delta = 0.2$, 0.6. Similar to the finite field case, the momentum dependence function totally varies by changing the value of anisotropy. For the higher temperature, i.e. $T = 0.25\ J$, the momentum dependence is a constant function at the isotropic point and an increasing function in the anisotropic case. For $T = 0.1J$, we have a decaying function (γ verses q) at $\Delta = 1$, while for the anisotropic case, this behavior is reversed, i.e. an increasing one, and the slope of the function strongly depends on the value of anisotropy.

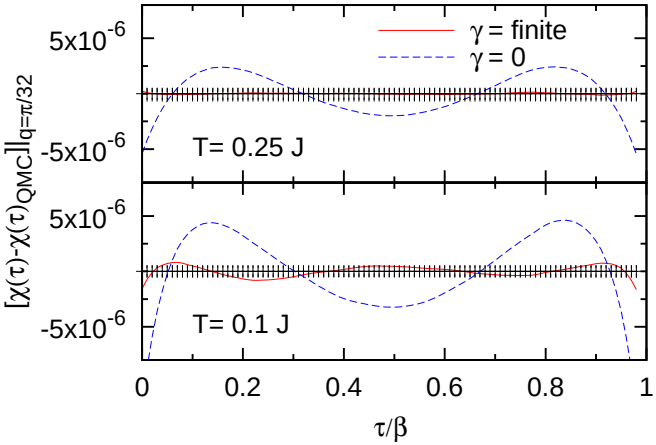

Figure 3.12.: Differences between the fitted curves and the original QMC data for $\Delta = 0.8$ and two temperatures at momentum $q = \pi/32$. The system-size considered is $L = 64$.

As it was done in the finite field case, we would like to obtain the behavior of K and v, this time, as a function of exchange anisotropy and compare it with the exact results of BA at zero temperature. This is shown in Fig. 3.11 and an excellent agreement is found which is again a proof of the validity and accuracy of our approach. Nevertheless, due to finite temperature, small deviations of these parameters from the zero temperature ones are evident at larger values of Δ.

The fitting error has also been tested and it was found that in any cases, γ is associated with small errors that are almost within the error bars of QMC data, while assuming zero relaxation rate leads to larger fitting errors. This is shown in Fig. 3.12 for one example of the anisotropic case, i.e. $\Delta = 0.8$.

In conclusion, our results for the anisotropic chain $\Delta < 1$ disagree with the common idea of transport that suggests a zero diffusion for the gapless region, but rather they are consistent with the bosonization results and numerical calculations of time-dependent density matrix renormalization group in Refs. [26, 27], where a coexistence of ballistic and diffusive channels of transport has been proposed.

3.7. Summary

Using a combination of the QMC method and results from a perturbation theory based on bosonization and providing several complementary analyses, we have studied finite temperature spin transport of the spin-1/2 XXZ chain and addressed the question of valid limits for ballistic and diffusive regimes. We started with a finite size scaling of the isotropic chain for system-sizes ranging from 64 up to 256, in order to show the size dependence of the spin current relaxation rate. We found that finite size effects are negligible beyond $L = 64$. We made a comparison to ED calculations of the dynamic structure factor for a finite system-size $L = 18$ and intermediate temperatures to show the tendential behavior of the spectrum as temperature decreases down to temperatures where bosonization is valid. As a result, we found very good agreement between ED and our method which proves the validity of our approach. We have also studied effects of external magnetic field as well as exchange anisotropy on the Luttinger parameter, the spin velocity and more importantly the relaxation rate of the model. We showed that the results for the relaxation rate are qualitatively consistent with previous studies [26, 27], although there exist quantitative differences. The evaluation of the Luttinger parameter and the spin velocity at finite temperature were in good agreement with zero temperature BA results.

4. Quantum phases and dynamics of spin-1 chain

In this chapter of the thesis, we will be mainly concerned about dynamics of spin-1 chain with the general Hamiltonian

$$H = J \sum_n \vec{S}_n \cdot \vec{S}_{n+1} - h \sum_n S_n^z + D \sum_n (S_n^z)^2, \tag{4.1}$$

where J is the antiferromagnetic exchange interaction, D is the single-ion anisotropy and h indicates the applied longitudinal magnetic field. The spin-1 Heisenberg chain is one of the fundamental models in strongly correlated low-dimensional systems. It is also the simplest model to demonstrate the Haldane conjecture [6]. For the isotropic case, $D = 0$, and zero magnetic field, $h = 0$, there have been many efforts to discover the elementary excitations of the chain using various theoretical and numerical methods. It is well known that the lowest-lying excitation of this model is a single-magnon mode. The lower edge of this mode has been obtained as a function of momentum in Ref. [117]. Its minimum boundary is the Haldane gap which happens at π in wave vector. It is also believed that a two-particle excitation dominates the spectrum at small momenta near $q = 0$ [118]. This continuum is separated from the ground state by twice the size of the Haldane gap 2Δ, whereas the second lowest-excitation at $q = \pi$ which is a three-particle continuum, starts at 3Δ. The existence and boundaries of these elementary excitations have been studied using several numerical methods as well as nonlinear σ model (NLσM) which is an approximation based on large-spin expansion [29, 115, 119–122]. While the single magnon mode is observed clearly in many experiments [123–125], the multi-particle continua have not yet been confirmed experimentally.

A quantitative approach to the spectral function of the spin-1 chain at zero magnetic field and isotropic point has been performed using time dependent density matrix renormalization group (tDMRG) [30]. The results have been compared to NLσM predictions and a qualitative agreement resulted.

Since most experimental spin-1 chain materials such as NENP, DTN, NENC, NDMAP, NDMAZ and even the well known isotropic one, $CsNiCL_3$, have at least a small single-ion

anisotropy, it is of great interest to analyze the evolution of the excitation spectrum as a function of anisotropy. Moreover many experimental measurements including neutron scattering [126, 127] (NS), electron-spin resonance [128, 129] (ESR), nuclear magnetic resonance [130–132] (NMR) and the thermal transport [133] have been performed at finite magnetic fields, therefore it is of relevance to take magnetic field into account and survey its role in the dynamic calculations. So the main purpose of this chapter is to study the role of anisotropy and magnetic field and specially the interplay between these two parameters in dynamics of the chain. We also show that our results are consistent with previous theoretical as well as numerical calculations [30, 115, 122].

To get a better understanding of our dynamic results, we would like to first reveal the quantum phase diagram of our model as a function of anisotropy and magnetic field which necessarily needs some thermodynamic calculations. The phase diagram, transition points and also the spin gap of the chain in terms of the anisotropy have been already obtained using various methods [111, 134–141]. We also know that by increasing magnetic field, the excitation gap between the singlet ground state and triplet excited state decreases linearly and at a critical applied magnetic field, it vanishes completely. At this point, the system undergoes a transition to a gapless Luttinger Liquid (LLQ) phase [142–144]. Although the behavior of the system in terms of these two parameters is known independently, a complete image of its phase diagram in the presence of both parameters simultaneously is to be obtained.

The outline of this chapter is as follows. First, we give a brief theoretical and experimental background in section 4.1 and 4.2 where in the theoretical part, the two common theoretical approaches to the integer spin systems are introduced and in the experimental part, a list of the most relevant and well studied experimental compounds in the context of Haldane chain and some of their properties are given. In section 4.3, we reveal the quantum phase diagram of the spin-1 chain as a function of single-ion anisotropy and magnetic field. We also discuss general properties of different phases and transitions between them in this section. We report magnetic excitations of the chain and their evolution in terms of single-ion anisotropy and magnetic field in section 4.4. Section 4.5 is devoted to the estimation of NMR relaxation rate which can be obtained from dynamic results of QMC. We summarize and conclude our findings in Sec. 4.6 .

4.1. Theoretical background

Although an exact solution (using Bethe ansatz) of the spin-1 antiferromagnetic chain has not been found, there are some powerful theoretical approaches which have been able to largely explain the main physical properties of the model. The most common of them are the nonlinear σ-model and the AKLT method.

4.1.1. Nonlinear σ-Model

The importance of the Nonlinear σ-Model (NLσM) is partially due to the fact that the very big evolution in the field of strongly correlated systems known as the Haldane's conjecture was primarily described using this model [6]. NLσM was first introduced in high energy physics in the context of chiral symmetry breaking and then was developed in the condensed matter physics where it explains the low energy physics of microscopic models [145].

Following Refs. [146–148], here we briefly describe this model. Starting from the Heisenberg Hamiltonian for a spin-S chain

$$H = J\sum_l \mathbf{S}_i \cdot \mathbf{S}_{i+1} - \mathbf{B} \cdot \sum_i \mathbf{S}_i, \tag{4.2}$$

with $\mathbf{B}$ being a general form of an external magnetic field. Introducing the set of coherent states, the corresponding partition function in the quasiclassical NLσM can be written as

$$Z = \int D\boldsymbol{n} e^{-A_E/\hbar}, \tag{4.3}$$

where $\boldsymbol{n}$ is the unit vector (the spin direction) parameterizing the set of coherent states

$$|\boldsymbol{n}\rangle = e^{iS^z\varphi} e^{iS^y\theta} |S^z = S\rangle, \tag{4.4}$$

and A_E is the Euclidean action over the imaginary time axis $\tau = it$. If we break the spin variable $\boldsymbol{n}$ into smooth and staggered parts, $\boldsymbol{n}_j = \boldsymbol{m}_j + (-1)^j \boldsymbol{l}_j$, we will have the continuum fields $\boldsymbol{m}$, $\boldsymbol{l}$ under the terms of $\boldsymbol{ml} = 0$, $\boldsymbol{l}^2 + \boldsymbol{m}^2 = 1$. For weak fields at low energies, the magnetization of the antiferromagnet is small, $|\boldsymbol{m}| \ll |\boldsymbol{l}|$ and therefore the term $\boldsymbol{m}$ in the constraint can be neglected and we are left with $\boldsymbol{l}$ as a unit vector. Thus the effective Euclidean action can be rewritten as [148]

$$A_E = A_B + \frac{1}{2}\int_0^\beta d\tau \int dx \{(\partial_\tau \boldsymbol{l} + i\boldsymbol{l} \times B)^2 + (\partial_x \boldsymbol{l})^2\}, \tag{4.5}$$

where A_B is the Berry or topological term and is given by

$$A_B = i2\pi\hbar SQ, \qquad Q = \frac{1}{4\pi}\int dx d\tau \boldsymbol{l} \cdot (\partial_\tau \boldsymbol{l} \times \partial_x \boldsymbol{l}). \tag{4.6}$$

Q is an integer value which indicates how many times the vector $\boldsymbol{l}$ sweeps the unit sphere when time and space dimensions are swept. The presence of the topological term is the origin of the difference between low excitation spectra of half-odd and integer spin systems. For integer spin S, the topological term A_B is ineffective in the NLσM formulation because

it is a multiple of $2\pi\hbar$ which leads to zero contribution in the partition function. In this case, the zero temperature partition function of the system with a dimension d is equivalent to that of a classical ferromagnetic system with dimension $D = d + 1$ at an effective temperature, $T_{eff} = 2/S$. The counterpart of a spin-S chain with regard to this correspondence is a 2D classical ferromagnet. It is known that at finite temperature, the 2D classical ferromagnet has a finite correlation length $\xi \propto e^{2\pi/T_{eff}}$ [149, 150] which corresponds to a finite Haldane gap Δ in integer spin chains. For the case of half-odd integer spins, the topological term contribute actively as a destructive phase term in the partition function and consequently a gapless spectrum for the Heisenberg spin-S chain is produced [151, 152]. This difference between the low energy excitation of integer and half-integer chains is known as the Haldane conjecture [6].

4.1.2. AKLT model

In principle the AKLT model can describe any integer spin system in one dimension and more [153, 154]. One common and important example for this model is the spin-1 chain with a Hamiltonian which is described by introducing a *projector operator*, $P^{J=2}$. This operator projects the states of two neighboring spin-1 sites onto a subspace with total spin $J = 2$. Thus for the Hamiltonian we have

$$H^{AKLT} = K \sum_i P^{J=2}_{i,i+1}, \tag{4.7}$$

where the projector operator $P^{J=2}_{i,i+1}$ can be given in terms of first neighbor interactions

$$P^{J=2}_{i,i+1} = \mathbf{S}_i \cdot \mathbf{S}_{i+1} + \frac{1}{3}(\mathbf{S}_i \cdot \mathbf{S}_{i+1})^2. \tag{4.8}$$

This leads to the following Hamiltonian

$$H^{AKLT} = K \sum_i \mathbf{S}_i \cdot \mathbf{S}_{i+1} + \frac{1}{3}(\mathbf{S}_i \cdot \mathbf{S}_{i+1})^2, \tag{4.9}$$

where K is a positive constant. The AKLT Hamiltonian has an extra biquadratic term compared to the standard Heisenberg model. However the ground state and excitations of this model are similar to those obtained from other approaches based on the Heisenberg Hamiltonian and therefore the physical effects of the biquadratic term in the AKLT Hamiltonian are practically small. To obtain the ground state of Eq. 4.7, we use the idea of *valence bonds*, where for each two neighbors of spin-1/2, a valence bond is formed by making a singlet state of the spins. For the case of a spin-1 chain, each spin is regarded as the symmetric part of the product of two spin-1/2's where each of them are linked to a

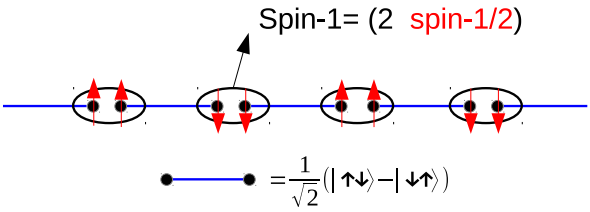

Figure 4.1.: The AKLT model for the ground state of the spin-1 chain is represented.

spin-1/2 of the nearest site by constructing a singlet state. This state is called the valence bond state (VBS) and is represented in Fig. 4.1 for a spin-1 chain. The same structure can be considered for higher integer spins such as a spin-2 chain. It is worth mentioning that the ground state of a chain with open boundary conditions is different from that with periodic ones due to the presence of the two free spin-1/2's at ends of the chain. While the ground state of a periodic chain is a nondegenerate singlet state, for open boundary conditions, there exists a fourfold degeneracy including singlet and triplet states [155]. One simple example which shows the success of the AKLT model for the spin-1 chain is the determination of the ground state energy per spin $E = -\frac{4}{3}$ which is quit close to the numerical value of that, $E \simeq -1.4$ [156].

One is interested in the VBS wave function of the AKLT Hamiltonian. A very simple representation of these wave functions is shown in the language of *matrix product states* [157, 158]. We have

$$|\psi\rangle = Tr(g_1 \otimes g_2 \otimes ... \otimes g_N), \qquad g_n^{AKLT} = \frac{1}{\sqrt{3}} \begin{pmatrix} -|0\rangle_n & -\sqrt{2}|-\rangle_n \\ \sqrt{2}|+\rangle_n & |0\rangle_n \end{pmatrix} \tag{4.10}$$

where $|+/-/0\rangle_n$ indicate different z components of the spin S^z at site n. One can prove that $|\psi\rangle$ is the ground state of the AKLT Hamiltonian $H^{AKLT}|\psi\rangle = 0$ by considering the product of nearest neighbor matrices $g_i \otimes g_{i+1}$ [158].

An important question one expect a robust model like AKLT to answer is description of lowest excitations. It is known that the Haldane chain has a triplet state above the singlet one as the first excitation mode. In the AKLT model, this can be captured by replacing one of the singlet links in the wave function of the model with a triplet one at site n

$$|\mu, n\rangle = Tr(g_1^{AKLT} \otimes ... \otimes g_{n-1}^{AKLT} \otimes (g_n^{1\mu}) \otimes g_{n+1}^{AKLT} \otimes ... \otimes g_N^{AKLT}) \tag{4.11}$$

where $\mu = S_z$ and $g^{1\mu}$ is defined as

$$g^{1\mu} = a\sigma^\mu \cdot g^{AKLT} + b g^{AKLT} \cdot \sigma^\mu, \tag{4.12}$$

with the ratio a/b being a free parameter which can be set to 3 in order to achieve orthogonal states $|\mu, n\rangle$ on different sites [159]. The corresponding states are solitons with a very simple form of magnon dispersion relation [160]

$$\varepsilon(k) = \frac{5}{27}(5 + 3\cos k). \tag{4.13}$$

which shows a gap at $k = \pi$ as $\Delta = \varepsilon(\pi) = \frac{10}{27} \simeq 0.37$. This gap and the overall structure of the excitation spectrum is almost similar to that of a Haldane chain. It is also believed that this kind of spectrum is valid for the isotropic spin-1 chain as well as the anisotropic one [161].

4.2. Experimental background

The first experimental evidence of the Haldane conjecture has been observed in the quasi-1D antiferromagnet $CsNiCl_3$ [4, 162], where inelastic neutron scattering measurements have clearly revealed the existence of a gap in the excitation spectrum. $CsNiCl_3$ is one of the most isotropic and best studied quasi-1D spin-1 antiferromagnetic compounds. Its crystal structure is hexagonal within the space group P63/mmc. Ni^{2+} ions form the chains along the c axis and a triangular lattice in the a-b plane. A reliable estimate for the in-chain exchange coupling is $J = 2.275$ mev [163] and there exists a very small single-ion anisotropy, $D = 0.002\ J$. The disadvantage of $CsNiCl_3$ as a 1D compound is the large interchain coupling which leads to a 3D order. Other candidates for the Haldane chain are $Ni(C_2H_8N_2)_2NO_2(ClO_4)$ (NENP) [11], $Ni(C_5D_{14}N_2)_2N_3(PF_6)$ (NDMAP) [164–166], $Ni(C_5H_{14}N_2)_2N_3$ (ClO_4) (NDMAZ) [167, 168], $Ni(C_3H_{10}N_2\ )_2N_3(ClO_4)$ (NINAZ) [169], $AgVP_2P_6$ [170] and Y_2BaNiO_5 [171]. Among these materials, one of the most studied via inelastic neutron scattering is NENP which has a strong planar anisotropy. This compound is a better candidate than $CsNiCl_3$ because it has no three dimensional long-range magnetic order down to low temperatures and moreover the exchange interaction of NENP is almost three times larger than that of $CsNiCl_3$. Other experimental measurements performed on Haldane chain consist of susceptibility, magnetization, nuclear magnetic resonance, electron spin resonance, muon spin resonance and specific heat measurements where in all cases, the obtained data have been in a very good agreement with the theoretical predictions of the Haldane picture. The magnetization measurements of NENP have given clear evidence for the existence of a critical field at which the lower branch of the excited triplet state vanishes [172, 173]. Recently much interest has been devoted to NDMAP and NDMAZ, specially in the high-field experiments because of their very small critical field which is accessible to many experimental probes [127, 174, 175]. Both of these compounds, similar to NENP, have easy-plane anisotropy.

4.3. Phase diagram

Understanding the phase diagram of a model in terms of various system parameters has been always of great interest both for experiment and theory. In this section we study the phase diagram of the spin-1 chain in terms of magnetic field and single-ion anisotropy. On the one hand, a complete picture for such a phase diagram has not yet been given in the literature, on the other hand, since the main goal of this chapter is to study dynamics of the chain, it is instructive to discuss this in the context of relevant quantum phases.

4.3.1. Zero magnetic field

At zero magnetic field, the phase diagram of the spin-1 chain in terms of single-ion anisotropy has been already investigated [111, 134–136]. It consists of Néel , Haldane and large-D phases. The transition from Néel to Haldane is an Ising type of transition while the one from Haldane to large-D is of Gaussian type. The transition points between these phases have been determined using various numerical methods. Although there are slight quantitative differences between results of different methods for the transition points, it is believed that the transition between Néel and Haldane takes place around $D \simeq -0.31J$ and that between Haldane and large-D is happening around $D \simeq 1.0J$ [137–140]. All these three phases are gapful.

4.3.2. Finite magnetic field

It is known that the spin gap of a Haldane chain decreases by increasing easy-plane anisotropy, but a gapless phase is never reached. Applying an external magnetic field can drive the system into a gapless LLQ phase [142–144]. This means that at finite fields, we have a LLQ phase opening up between Haldane and large-D. Here we want to establish this and see how in general the quantum phase diagram evolves by increasing magnetic field. A very common way to characterize the Haldane phase is to estimate the *string order* parameter which is a nonlocal order parameter and in some sense the topological order of the Haldane phase [134, 135]. The string order is defined as a limiting value of the following correlator

$$O_S^{\alpha}(n,n') = \lim_{|n-n'|\to\infty} \left\langle -S_n^{\alpha} e^{i\pi \sum_{j=n+1}^{j=n'-1} S_j^{\alpha}} S_{n'}^{\alpha} \right\rangle, \qquad \alpha = x,y,z. \tag{4.14}$$

The presence of this order means that the ground state of the chain favors those spin states where $|+\rangle$ and $|-\rangle$ spin states alternate and they are separated from each other

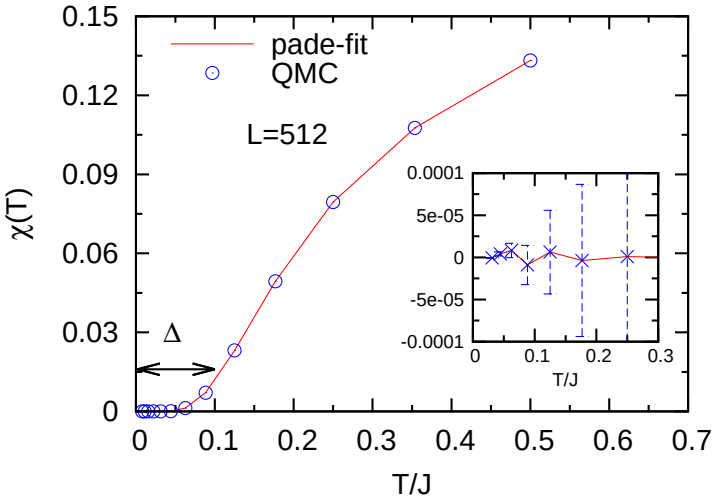

Figure 4.2.: The spin susceptibility in terms of temperature obtained from QMC is shown for a spin-1 chain of size $L = 512$ (symbols). A Padé fit to the data is also plotted (solid curve). Here Δ is an estimate of the spin gap. In the inset the error of the fitting and QMC error bars are shown.

by strings of $|0\rangle$ spin state of arbitrary length. This implies that the string order preserves in the Haldane phase. However it is shown that this order parameter is fragile to perturbations which break the rotational symmetry, while keeping other symmetries such as time-reversal, parity and translation symmetries [176–178]. Since both Haldane and large-D phases are gapped while the LLQ formed between them is gapless, one alternative way to capture the boundary of these phases is to scale the energy gap of the chain which is sometimes a hard task because of critical behaviors near to transition points [179]. The spin gap of the chain has to be finite in the Haldane phase, vanishing in the LLQ phase and finite again in the large-D phase. So by looking at the behavior of the spin gap, we would be able to distinguish between gapped and gapless regions of the phase diagram. To obtain the spin gap, first we measure the uniform spin susceptibility in terms of temperature, $\chi(T)$, for a large system size. One can then extract the gap by fitting the low-temperature values of $\chi(T)$ to

$$\chi(T) \approx e^{-\Delta/T} P_k^l(T)/T, \tag{4.15}$$

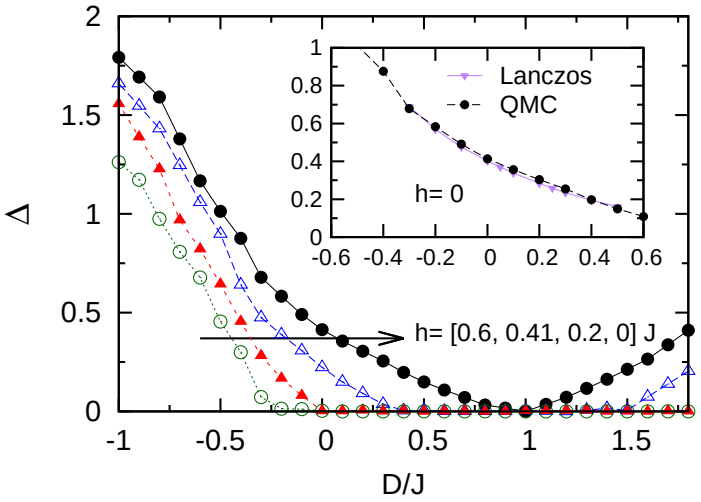

Figure 4.3.: Spin gap of the spin-1 chain in terms of single-ion anisotropy for several external magnetic fields. Inset: for zero magnetic field, the spin gaps in terms of single-ion anisotropy obtained from QMC and Lanczos methods are compared. Lanczos data are extracted from Ref. [141].

where $P_k^l(T)$ is a Padé approximant of order $[l, k]$. The lowest temperature considered here is $T = 0.0078J$ and the calculations are performed for a system with 512 sites. The fitting errors are within the QMC's error bars which are of the order of 10^{-4}. More details of this method can be seen in Fig. 4.2 where the spin susceptibility of a spin-1 chain in terms of low temperatures has been plotted. The solid line shows the Padé approximant to the data and the difference between the Padé approximant and the QMC data is shown in the inset where the error bars of QMC are also plotted. As seen in the inset, this difference is much smaller than the QMC error bars which represents the accuracy of the fitting method. This method is also able to give accurate estimates for the spin gap of higher integer spin chains [50, 180] as well as more complicated systems such as n-leg ladders.

Using this approach, the spin gap as a function of the single-ion anisotropy for different magnetic fields is obtained (see Fig. 4.3). For each magnetic field, we have a gap closure which is identified as a transition from Haldane into LLQ. There is also a reopening of the gap which characterizes the transition from LLQ into the Large-D phase. At zero magnetic field, as expected, the transition is directly from Haldane to large-D without

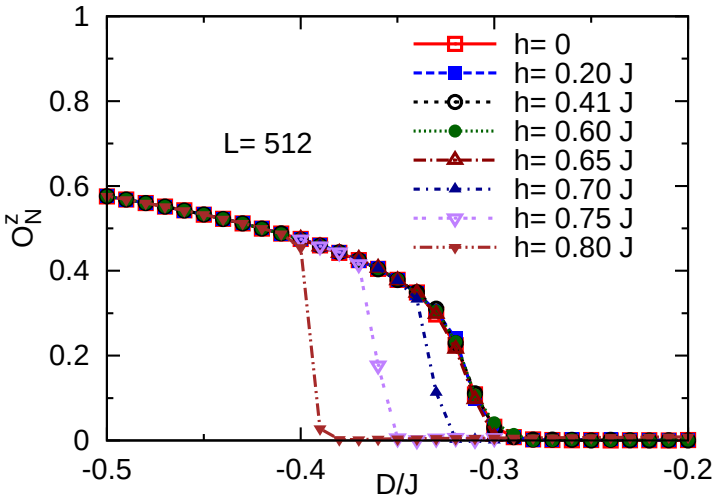

Figure 4.4.: Néel order parameter is shown as a function of anisotropy for different magnetic fields. The temperature and system size considered here are $T = 0.01J$, $L = 512$, respectively.

accessing the LLQ phase. But as soon as we switch on the magnetic field, an increasing area of the LLQ phase opens up between the Haldane and the large-D phase. In the inset of Fig. 4.3, the gap is compared to that obtained form a finite size Lanczos method for zero magnetic field and small values of D [141] and a very good agreement is found, though due to the finite size effects in the Lanczos method [141], its curve lies almost below the QMC curve. It should be noted that the small wiggling in the curves of Fig. 4.3 especially for large D's is due to the fitting procedure when extracting the spin gap from spin susceptibility and it does not have anything to do with the accuracy of the data obtained from QMC. It is clear from Fig. 4.3 that the Haldane-Néel transition can not be captured just by the gap study of the system simply because both Haldane and Néel phases have finite gaps. To distinguish between these gapped phases, we use another approach, namely by analyzing the *Néel parameter*. It is well known that long-range spin-spin correlations vanish in the Haldane phase while they have a finite value in the Néel phase. Considering the Néel parameter, we can find a transition from the disordered Haldane phase to the ordered Néel one [181]. This method has been already used to determine the Haldane phase boundaries as a function of exchange anisotropy in a XXZ

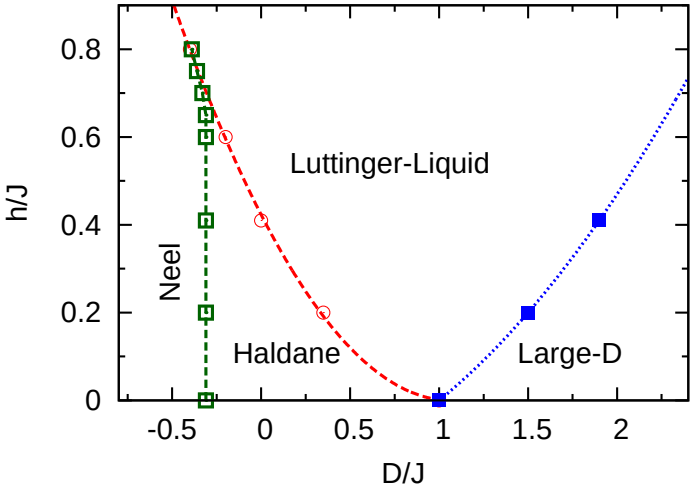

Figure 4.5.: The phase diagram of a spin-1 Heisenberg chain as a function of single-ion anisotropy and magnetic field is shown.

spin-1 chain model [182]. The spin-spin or Néel correlations of the system are given by

$$\mathcal{O}^z_{\rm N}(i,j) = (-1)^{i-j}\langle S^z_i S^z_j\rangle, \tag{4.16}$$

and the Néel parameter can be defined as long-distance correlations, $O^z_{\rm N} = \lim_{|i-j|\to\infty} \mathcal{O}^z_{\rm N}(i,j)$. A finite $O^z_{\rm N}$ indicates an antiferromagnetic state of the system. By calculating the Néel parameter for a range of magnetic fields and anisotropies shown in Fig. 4.4, we have found the following. At zero magnetic field, the transition point that we have obtained is $D \sim -0.31J$ which is very close to the value suggested in Refs. [138, 140]. Surprisingly, this transition is independent of magnetic field up to the point where we reach the LLQ phase. This means that the border between Haldane and Néel is a straight line as seen in Fig. 4.5. Considering the fact that long-range spin-spin correlations must also vanish in the LLQ phase, we can indicate the transition between Néel and LLQ by increasing magnetic field to large values ($h/J \gtrsim 0.7$). As shown in Fig. 4.5, this transition coincides with that obtained from the gap study of the system.

As a result, the complete phase diagram of the spin-1 chain in terms of the single-ion anisotropy and magnetic field is obtained (shown in Fig. 4.5) in which the boundaries

between Haldane, LLQ and large-D phases are taken from closure and reopening the spin gap as we described in the gap study of the chain and the borders between Néel and Haldane and also between Néel and LLQ are obtained from the behavior of the spin-spin correlations. The dashed lines which have linked the symbols are just guides to the eyes.

4.4. Dynamic structure factor

As explained in chapter 2, the dynamic structure factor (DSF), $\mathbf{S}(\mathbf{q},\omega)$, of a spin system can be accessed using the imaginary time spin-spin correlation functions obtained from QMC simulations by applying a maximum entropy method in order to transform the imaginary time data into the real frequency domain. Here we discuss the transverse dynamic structure factor of the spin-1 chain in the presence of single-ion anisotropies an external magnetic fields. We have chosen several magnetic fields and anisotropies in the way that all quantum phases described in the previous section except for the large-D phase are covered so that one can get a fine understanding of the dynamics of the chain within the relevant quantum phases.

4.4.1. General overview of $\mathrm{S}(\mathbf{q},\omega)$

Contour plots of the transverse dynamic structure factor (tDSF) of the isotropic chain for four different magnetic fields are plotted in Fig. 4.6. There are some main points in these contour plots we want to note. A very sharp peak, i.e. the single magnon mode can be clearly seen in panel a, where the magnetic field is zero. While it holds most of the spectral weight at large momenta near $q = \pi$, its weight decreases rapidly as we go to lower momenta so that it smears as $q \to 0$. As we switch on the magnetic field, the peak starts to split into two branches due to the Zeeman effect. The splitting is more visible in panel c where the magnetic field is equal to the Haldane gap. At this point, the lower branch of the peak touches the ground state, the gap is completely closed and we enter the LLQ phase (see also Fig. 4.5).

4.4.2. Small and large momenta

In addition to the very sharp magnon mode, there are also some multi-particle continua in the spectrum which have much smaller weights compared to the mode so that they are not easily visible in the contour plots. Therefore we have plotted a cut through DSF's

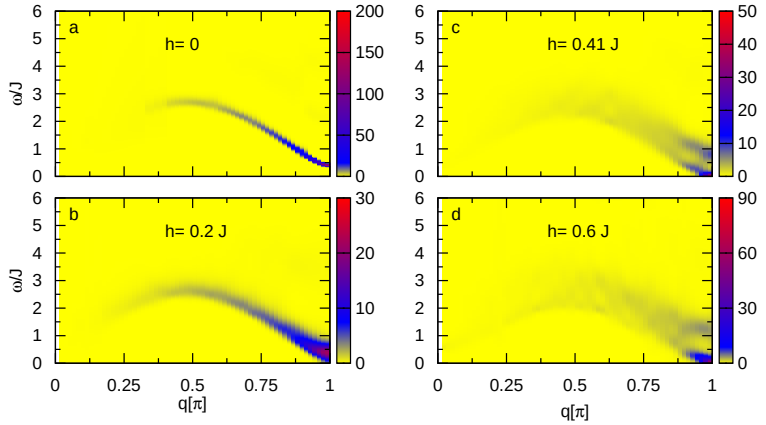

Figure 4.6.: Contour plot of the transverse dynamic structure factor of the isotropic spin-1 chain as a function of frequency ω and wave vector q for four different magnetic fields. The system size of the chain for all cases is $L = 128$ and temperature is set to $T = 0.1\ J$.

at various anisotropies and magnetic fields in Fig. 4.7, where one can clearly see the shape and the weight of the spectra despite the very large difference in their scale at different frequency and momentum regions. We have chosen three magnetic fields, $h = 0$, 0.2, $0.41J$, for each of which the tDSF is obtained at the isotropic point, two easy-axis anisotropies, $D = -0.2$, $-0.5J$, and two easy-plane anisotropies, $D = 0.2$, $0.5J$. For each of these cases two wave vectors have been considered, $q = \pi/64$ (left panels) and $q = \pi$ (right panels).

Starting from the isotropic case at small momenta (see panel c of Fig. 4.7), what we see for a zero magnetic field is a peak at zero frequency which is a signature of thermal fluctuations due to finite temperature. This is accompanied by a small continuum at higher frequencies which is not observable in the panel because of its relatively small weight. As we go to larger wave vectors, this continuum gets larger and dominates the spectrum. We will refer to this later on. The zero frequency peak and the continuum shift to larger frequencies, as we increase magnetic field such that the peak of the spectrum locates at a frequency which is equal to the magnitude of the applied field.

Considering anisotropy in the model, either the easy-axis one (as seen in panels a and b) or the easy-plane one (as seen in panels d and e), leads to shifting the weight of the

spectrum to larger frequencies. What is more interesting is the effect of the interplay between anisotropy and magnetic field on the spectrum. This interplay strongly differs depending on the value and the type of anisotropy. While in the case of easy-plane anisotropy, the magnetic field only shifts the weight of the spectrum, in the case of easy-axis anisotropy, there is a splitting of the dominant peak as a result of the interplay.

Another remarkable feature is that the spectrum in the Néel phase at $D = -0.5J$ differs qualitatively regarding its intensity and spectral extent as compared to the spectra in the quantum disordered phases. This can be seen by comparing panels a and f of Fig. 4.7 with the other panels in the same figure.

Moving to the spectra at $q = \pi$, one can clearly see the sharp magnon peak which dominates the spectrum at all anisotropies and magnetic fields. At zero magnetic field, the peak position which is a fingerprint of the spin gap shifts towards lower frequencies, as we go from the strong easy-axis anisotropy, $D = -0.5J$, in panel f to the strong easy-plane one, $D = 0.5J$, in panel l. We have found a very good coincidence between these peak positions and the spin gaps obtained from our gap study in the thermodynamic limit despite the fact that the temperature considered for calculating DSFs is a finite temperature, $T = 0.1J$, and not zero. Even at finite magnetic field, the monotonous behavior of the spectrum in terms of anisotropy persists but it is accompanied by a splitting of the peak due to the Zeeman effect as we have already mentioned when discussing the contour plots. As we increase magnetic field, the distance between the two branches of the magnon mode gets larger until the lower branch reaches the ground state and we have a peak at zero frequency. This is where we enter LLQ phase and the spin gap is zero. Increasing magnetic field after this point leads to accumulating weight at zero frequency peak but smearing the higher branch of the spectrum. This behavior can be seen clearly by comparing panels k and l.

In addition to the single-magnon mode, a small multi-particle continuum exists at higher frequencies. This is most likely a three-magnon continuum as proposed in Refs. [30, 115] or a combination of that with higher multi-magnon continua. This is shown in the inset of right panels of Fig. 4.7. We must note that the weight of this continuum is much smaller than that of the single-magnon mode and that is probably why in many numerical as well as experimental measurements, it has not been observed.

4.4.3. Isotropic point and zero magnetic field

At the isotropic point, results have been obtained by several other methods such as NLσ, free boson method and tDMRG [30, 115, 122]. Here, we present a comparison of our results and those. In Fig. 4.8, we have shown this comparison for two momenta, a

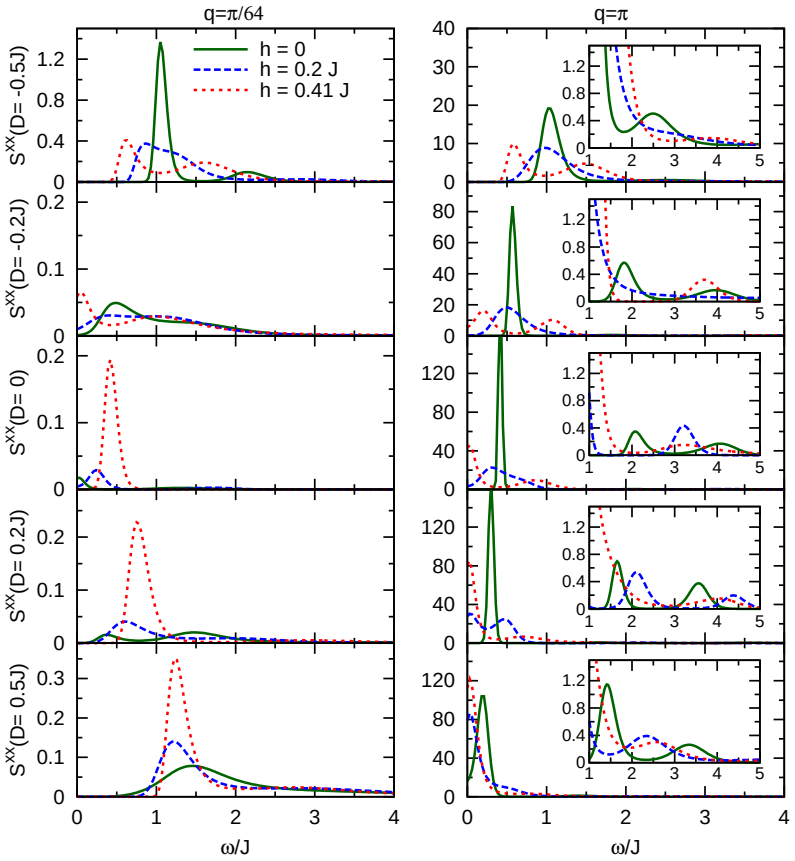

Figure 4.7.: Transverse dynamic structure factor of the spin-1 chain as a function of frequency at two wave vectors $q = \pi/64$, π, and for different anisotropies and magnetic fields. The system size of the chain for all cases is $L = 128$ and temperature is set to $T = 0.1J$. In the insets of the right panels, the large-frequency tail of the spectrum in a larger scale is shown.

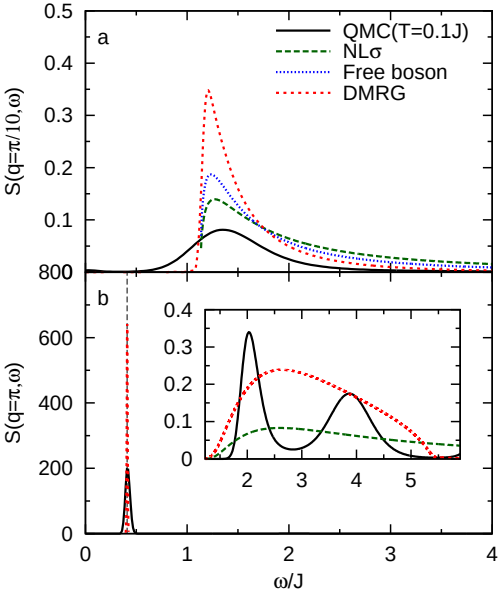

Figure 4.8.: Dynamic structure factor of the isotropic chain at zero magnetic field for two wave vectors ($q = \pi/10, \pi$) obtained from different methods. For QMC data, the temperature is set to $T = 0.1J$ while for other data which are extracted from Refs. [30, 115, 122], the temperature is set to zero.

rather small one $q = \pi/10$, and $q = \pi$ In the case $q = \pi/10$ which is shown in panel a of Fig. 4.8, a good qualitative agreement between different methods is found. The small broadening in the QMC's spectrum is due to the finite temperature calculations ($T = 0.1J$) in contrast to other methods which are at zero temperature. The spectrum at $q = \pi$ is shown in panel b. Here again one realizes a finite temperature broadening of the QMC's spectrum as compared to that obtained from tDMRG, however their perfect overlapping and also consistency with the thermodynamic spin gap is remarkable. In the inset of panel b, tail of the spectrum at large frequencies obtained from three different methods is manifested. Although qualitative consistencies like comparable magnitude and range of different continua are evident, there are discrepancies regarding the shape of the continuum which varies from method to method. The tDMRG continuum has a single hump with a finite magnitude of weight and frequency range, while NLσ continuum is rather broad and has a rather long tail and that of QMC shows clearly a double peak

again with a finite frequency range. These differences are unclear at present.

4.4.4. Sum rules

In general, there are several applications for the sum rules such as evaluating contributions of multi-particle excitations to the spectral weight of the dynamical structure factor [183–185]. Here, however, we apply them to estimate the quality of the analytic continuation. The sum rules for the static structure factor $S^{\alpha\beta}(q)$ and the static susceptibility $\chi^{\alpha\beta}(q)$ can be obtained by integral transforming the dynamical structure factor [186]

$$S^{\alpha\beta}(q) = \frac{1}{\pi}\int_0^\infty d\omega(1+e^{-i\omega t})S^{\alpha\beta}(q,\omega) \tag{4.17}$$

$$\chi^{\alpha\beta}(q) = \frac{2}{\pi}\int_0^\infty d\omega\omega^{-1}(1-e^{-\beta\omega})S^{\alpha\beta}(q,\omega). \tag{4.18}$$

The way we use these rules to assess the quality of the analytic continuation is that the left side of each equation is obtained directly from static QMC calculations without considering any analytical continuation procedure, while the right side of the equations are calculated by integrating the dynamic structure factor obtained from MaxEnt over the whole range of frequency. The equality of the two sides can be interpreted as a consistency check on the accuracy of the MaxEnt method. Since both of these sum rules can be transformed into each other, we just evaluate the first one for $S(q)$. In Fig. 4.9, the comparison of the two sides of Eq. 4.17 is shown on a logarithmic scale for the range of anisotropies and magnetic fields presented in section 4.4. As a result, we find very good matching of the two sides of Eq. 4.17 is found with differences lying within the QMC error bars of the static structure factor. The QMC error bars are smaller than the symbols shown in Fig. 4.9. We note that such agreement fulfillment of the sum rules is remarkable because the typical MaxEnt error is estimated to be ∼10-20% [187].

4.5. NMR relaxation rates

Nuclear magnetic resonance or NMR is a phenomenon which occurs when the nuclei of certain atoms immersed in a static magnetic field are exposed to an additional oscillating magnetic field. The radiation energy absorbed or emitted from the nuclei has a resonance depending on the magnetic fields and magnetic properties of the atoms. The oscillating field in NMR causes a non-equilibrium magnetization in the sample. The process in which the z component of the magnetization vector comes back into its initial thermodynamic equilibrium is called *spin-lattice relaxation* and the corresponding time is the spin-lattice

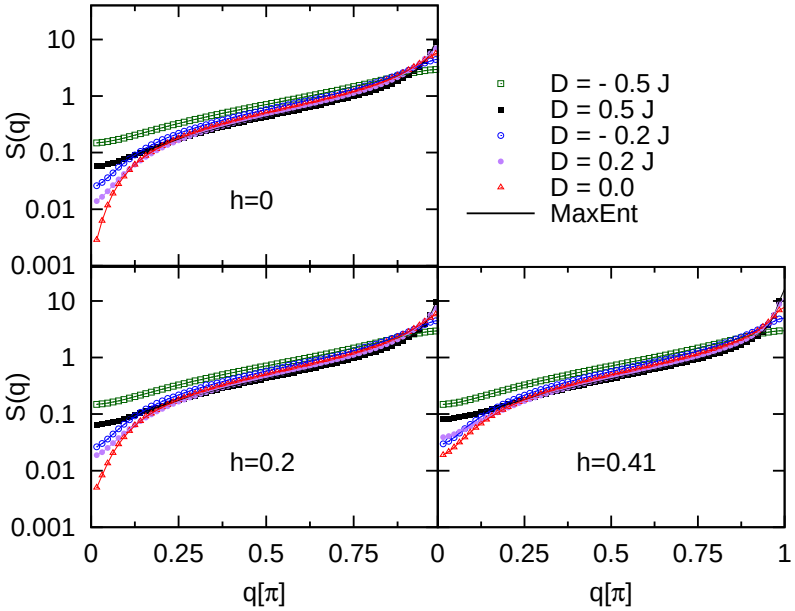

Figure 4.9.: Sum rule for different single-ion anisotropies $D/J \in 0, \pm 0.2, \pm 0.5$ and different fields $h/J \in 0, 0.2, 0.41$. Static structure factor obtained by QMC accurately without involving MaxEnt procedure is compared to that obtained from Eq. 4.17.

relaxation time, T_1. We can access the inverse of this time by a summation over all wave vectors of the dynamics structure factor obtained from QMC as described in the following relation

$$1/T_1 = \sum_q A(q) S^{\alpha,\beta}(q, \omega_R) \tag{4.19}$$

where $A(q)$ is the hyperfine coupling form factor evaluated at the NMR resonance frequency ω_R. The resonance energy is typically much smaller than the energy scale of spin exchange interactions, therefore one can set $\omega_R \to 0$ in Eq. 4.19. In Fig. 4.10 the NMR rate of the chain in terms of magnetic field for different anisotropies is plotted. The symbols are the direct evaluation of the NMR rate from QMC transverse dynamical structure factor using Eq. 4.19 and the dashed and solid lines correspond to the theoretical functions for the NMR rate proposed in Refs. [188, 189]. The two theoretical functions

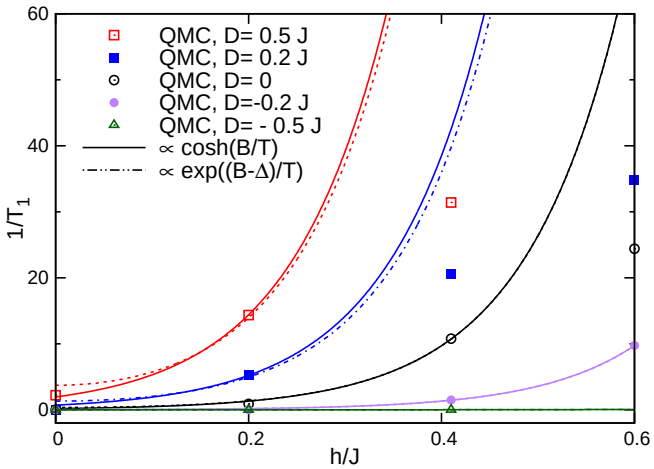

Figure 4.10.: Field dependence of the T_1-relaxation rate for different single-ion anisotropies of the spin-1 chain. The symbols are obtained from the zero frequency summation of the spectrum produced by MaxEnt method over the wave vectors as described in Eq. 4.19. The Solid and dashed lines correspond to other theoretical estimations of the relaxation rate in Refs. [188, 189]

are as follow. The first one is a hyperbolic function of the form $A\cosh(h/T)$ obtained from field theoretical approaches [188] while the second one is an exponential function of the magnetic field, $Ae^{(h-\Delta)/T}$ which has been suggested using a modified spin-wave theory [189]. Both of these functions are only valid well within the Haldane phase. As long as the magnetic field is substantially smaller than the spin gap $h < \Delta$ which is the valid region for the theoretical functions, they agree well with the NMR rates of QMC as seen in Fig. 4.10. These functions and their condition remain valid for finite single-ion anisotropies given that the anisotropy dependence of the spin gap has been taken into account when considering the region of validity, i.e. $h < \Delta(D)$. It should be noted that here, we have ignored the small momentum dependence of the hyperfine form factor and set it to a constant value, namely 1. However, for an experimental comparison this factor can be accessed as a free parameter in a fitting process.

4.6. Summary

We have used quantum Monte-Carlo to study the transverse dynamic structure factor of an antiferromagnetic spin-1 chain with single-ion anisotropy and subject to an external magnetic field. First we have uncovered the quantum phase diagram of the chain in terms of anisotropy and magnetic field. The phase diagram has been obtained by studying the spin gap and the spin-spin correlation functions of the system and was shown to consist of Néel, Haldane, Luttinger Liquid and Large-D phases.

Our main concern was to study the spin dynamics of these quantum phases and to see how anisotropy and magnetic field affect the excitation spectrum of the chain. We have successfully obtained the magnetic excitations spectrum of the chain at low temperatures for various anisotropies and magnetic fields over the complete Brillouin zone. As a result, we found a very pronounced single-magnon mode in the excitation spectrum. We also showed how this single mode is affected by the external fields and anisotropies, namely splitting, shifting and changing the weight of the mode. Moreover we have proved the existence of the multi-particle continua in the spectrum and showed the behavior of these continua as a function of our variables. Our results are consistent with those in Refs. [30, 115, 122], where other methods such as tDMRG, NLσ model and free boson theory have been used to study the spectral function of the isotropic spin-1 chain at zero magnetic field. Finally, we contrasted field dependence of the NMR rate for various anisotropies calculated from QMC spectra against those predicted by theoretical approaches such as field theory and spin wave theory.

5. Quantum phases and dynamics of a frustrated four-leg spin tube

Recently, $Cu_2Cl_4{\cdot}D_8C_4SO_2$ has been suggested to be a new spin-1/2 tube with four legs [12]. Tubes with four legs and only nearest neighbor AFM exchanges are *not* frustrated. However, substantial next-nearest neighbor AFM exchange, diagonally coupling adjacent legs, has been claimed for $Cu_2Cl_4{\cdot}D_8C_4SO_2$, rendering this ladder system frustrated. Inelastic neutron scattering [31, 32] has revealed a strongly one-dimensional (1D) elementary excitation, which is gapped and slightly incommensurate. The former is consistent with Haldane's conjecture [6] for 1D spin systems with an even number of spin-1/2 moments per unit cell. The latter is consistent with a frustrated exchange. Magnetic fields have been shown to stabilize the incommensurate spin correlations[31, 32]. Motivated by this, a *geometrically* frustrated and simplified four-spin tube (FFST) model has been introduced in Ref. [33], where a restricted regime of the phase diagram, the so called weakly coupled plaquettes regime was studied using a series expansion method. However, an understanding of the *quantum* phases of the FFST on a larger scale is still missing and therefore in this chapter, we study the ground-state phase diagram of the model using a variety of complementary techniques, namely, density matrix renormalization group, exact diagonalization, Schwinger boson mean-field theory, quantum Monte Carlo, and series expansion, we explore the parameter space of this model in the regime of all-antiferromagnetic exchange.

The structure of this chapter is as follows. In section 5.1, the model, its lattice structure, and the phase diagram of the classical FFST are given. In section 5.2, we consider the quantum phase diagram of the FFST and briefly describe quantum phases and the transitions between them Section 5.3 discusses the strong leg coupling region of the phase diagram. Spin susceptibility and dynamic structure factor of the tube will be studied in this section. Finally, we give a short summary of our results in 5.4.

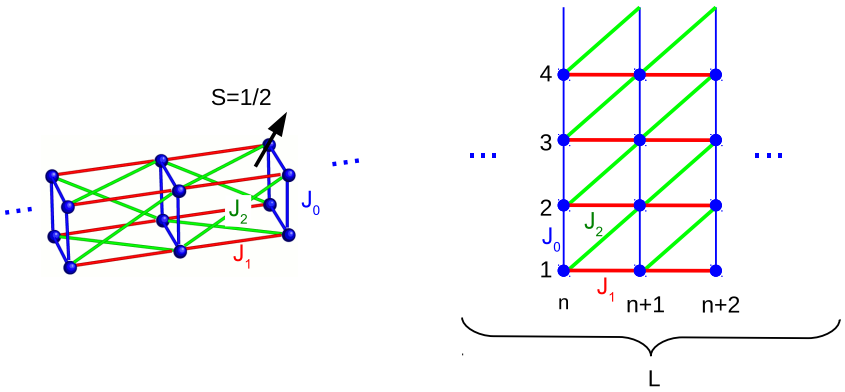

Figure 5.1.: A lattice structure of the frustrated four-spin tube is shown in two different views. Solid circles represent spin-1/2 moments. Plaquettes (bold blue lines)are coupled by nearest (J_1) and next-nearest (J_2) antiferromagnetic exchanges, red and green lines, respectively. On-plaquette coupling is shown by J_0. The left panel shows a closed view of the frustrated four-spin tube while an unwrapped structure of the tube is illustrated in the right panel where one can alternatively see a structure of an anisotropic triangular lattice.

5.1. Model and classical phase diagram

The lattice structure of our model is shown in Fig. 5.1. Spin-1/2 moments are located on the solid circles and all couplings, $J_{0,1,2}$ are antiferromagnetic. One can consider the tube as an anisotropic triangular lattice on a torus with four site circumference. The Hamiltonian is

$$H = \sum_{lm} J_{lm} \mathbf{S}_l \cdot \mathbf{S}_m \,, \tag{5.1}$$

where J_{lm} indicate the exchange couplings between nearest or next-nearest neighbors and can be reduced to $J_{0,1,2}$.

To achieve the classical phase diagram, we think about the spin structure as a spiral. This structure can be depleted to a planar structure as a result of unitary symmetry. Thus, we have

$$\mathbf{S}(\mathbf{r}_l) = S(\cos(\mathbf{Q}\cdot\mathbf{r}_l), \sin(\mathbf{Q}\cdot\mathbf{r}_l), 0), \tag{5.2}$$

with $\mathbf{r} = l_x\mathbf{R}_x + l_y\mathbf{R}_y$, where $\mathbf{R}_{x,y} = (1,0),(0,1)$, $l_x \in \mathbb{N}$, and $l_y = [1,\ldots,4]$. The transverse pitch vector Q_y has to be discretized according to $(0,1,2,3)\pi/2$. Introducing

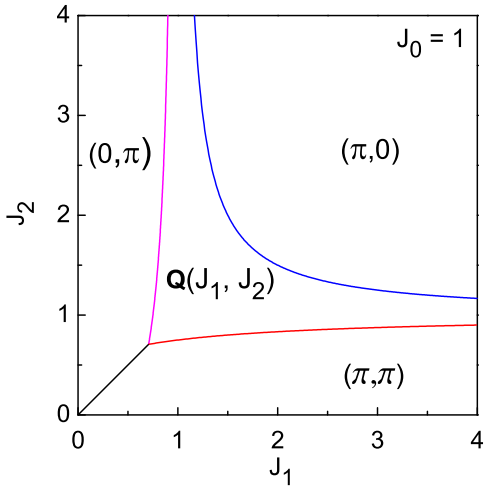

Figure 5.2.: Four classical phases of the FFST with commensurate pitches $\mathbf{Q} = (\pi, \pi)$, $(\pi, 0)$, $(0, \pi)$ and incommensurate regime $\mathbf{Q}(J_1, J_2)$ are shown.

these definitions and minimizing the ground-state energy

$$\varepsilon = J_0 cos(Q_y) + j_1 cos(Q_x) + J_2 cos(Q_x + Q_y), \tag{5.3}$$

we end up having classical phases with respect to the exchange couplings as shown in Fig. 5.2. For the sake of simplicity, we have set $J_0 = 1$ and described the phase diagram in terms of the two other couplings. This however doesn't distort the generality of the model. The regions in Fig. 5.2 can be described as follow

1) In the case of $J_2 \leqslant (1 + 2J_1)/(2(J_1 + 1))$ and $J_2 \leqslant J_1$, there exists a commensurate AFM phase with $\mathbf{Q} = (\pi, \pi)$.

2) In the case of $J_2 \geqslant (1 - 2J_1)/(2(J_1 - 1))$, $J_1 < 1$, and $J_2 \geqslant J_1$, there exists a commensurate AFM phase with $\mathbf{Q} = (0, \pi)$.

3) In the case of $J_2 \geqslant (2J_1 - 1)/(2(J_1 - 1))$ and $J_1 > 1$, there exists a commensurate AFM phase with $\mathbf{Q} = (\pi, 0)$

4) There are two degenerate incommensurate spirals with $\mathbf{Q}(J_1, J_2) = \pm(2\arctan(\alpha), \pi/2)$, and $\alpha = (J_1 + \sqrt{J_1^2 + J_2^2})/J_2$ in the remaining region of the phase diagram.

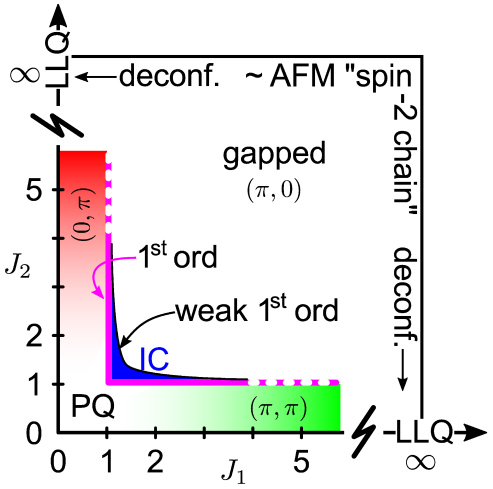

Figure 5.3.: Quantum phase diagram of the FFST

The classical phase diagram can not solely describe the real phase diagram of the model. Frustrations and quantum fluctuations may drive the system to a different quantum phase diagram. To discover this, we have done a very detailed study of the quantum phase diagram in the following. We believe that a comparison of these two types of phase diagram can be very informative and conclusive.

5.2. Quantum phase diagram

Here, we briefly describe the quantum phase diagram of the FFST. For more details on how this phase diagram is determined, we refer the reader to appendix A of this thesis and Ref. [34]. A variety of techniques including density matrix renormalization group, Schwinger boson mean field theory, exact diagonalization and series expansions has been used to determine the quantum phase diagram of the tube which is shown in Fig. 5.3 This figure should be contrasted against the tube's phase diagram in the classical limit, i.e. Fig. 5.2. While all phases in the latter are long range ordered, none of the quantum phases are.

The point $J_{1,2} = 0$ hosts a gapped system of decoupled plaquettes, while at the asymptotic points $J_{1(2)} \to \infty$, $J_{2(1)} = 0$, the spin tube consists of decoupled spin-1/2 chains in a

Luttinger liquid state. The phase diagram is symmetric with respect to interchanging $J_1 \leftrightarrow J_2$. On either of the two axes $J_{1(2)} = 0$, the system is unfrustrated, the inter-leg coupling is relevant, and a spin gap opens. This unfrustrated weakly coupled chain regime is known to be adiabatically connected to that of the weakly coupled plaquettes.

Turning on the frustrating exchange, our results are consistent with the weakly coupled plaquette regime to survive along two strips (red and green in Fig. 5.3) of width of order unity, parallel to each of the $J_{1(2)}$-axis, at least up to $J_{1(2)} \approx 5J_0$. The system remains gapped in this region. Accordingly, our analysis of correlation functions exhibits exponential real space decay. Consistent with series expansions around $J_{1,2} = 0$, the static structure factor obtained from density matrix renormalization group evolves smoothly from a flat plaquette signature around PQ in Fig. 5.3, into a peaked commensurate behavior along the red/green strips, parallel to each axis. The peak locations are consistent with short-range correlation remnants of the long-range order present in the classical limit of the tube in this region. As for the unfrustrated four-leg tube, we expect no quantum phase transition while increasing $J_{1(2)} \to \infty$ parallel to the axis within these strips until the Luttinger liquid fixed point is reached (zig-zag marks in Fig. 5.3).

Perpendicular to the $J_{1,2}$-axis the plaquette regime is terminated by a line of first order transitions evidenced by those of our techniques able to detect ground state energy level crossings. The critical lines emerge approximately from the point of maximum frustration $J_{0,1,2} = 1$ and run parallel to the $J_{1,2}$ axes (magenta line in Fig. 5.3). The numerical precision, locating the level crossing along the borders of the PQ strip, decreases away from $J_{0,1,2} = 1$, indicated by the doting of the magenta line.

Beyond the first order critical line, close to the point of maximum frustration, $J_{0,1,2} = 1$, DMRG shows that the plaquette phase turns into a gapped phase with short range incommensurate correlations (IC, blue in Fig. 5.3), analogous to the spiral phase which is found in the classical limit of the tube in this regime. Along the diagonal $1 \lesssim J_1 = J_2 \lesssim 1.3$, the static structure factor shows a maximum approximately at the pitch vectors of the classical spiral phase. Off the diagonal, the maximum of the static structure factor is slightly shifted from the classical values. Increasing the inter-plaquette coupling, around the line $J_1 \sim J_2$, the incommensurate quantum phase terminates with a very weak first order transition into a gapped commensurate $(\pi, 0)$ phase, labeled by the thin black line in Fig. 5.3. In contrast to the PQ (π, π) and $(0, \pi)$ region, the overall extent of the incommensurate region in the quantum case is strongly reduced as compared to that of the classical spiral phase.

Due to numerical limitations, it remains an open issue if the quantum IC and PQ regimes extend beyond $J_{1(2)} \sim 5$ at $J_{2(1)} \sim 1$.

5.3. Strong leg coupling

One of the phases of the FFST where the frustration can be neglected, is the strong leg coupling phase or the classical $(\pi, 0)$ phase which can be accessed by considering $J_{1,2} \gg J_0$ or by explicitly setting $J_0 = 0$. The good point about this phase is that one can apply QMC method to study its thermodynamic properties as well as its dynamics. This limit of the FFST can be also recognized as an anisotropic twisted square lattice on a torus. For the sake of simplicity, we set $J_0 = 0$, $J_1 = 1$ and normalize J_2 in terms of J_1.

5.3.1. Uniform susceptibility and spin gap

The real space arrangement of spins in the classical $(\pi, 0)$ phase at $J_1 \sim J_2 \gg J_0$ is that of a spin-2 AFM chain (see Fig.5.4). While in the quantum model the total spin per plaquette is not conserved, it is nevertheless tempting to speculate on a gap similar to that of an actual spin-2 AFM quantum chain at $J_1 = J_2$. This kind of mapping can be visualized in Fig. 5.4. Finite $J_{1,2}$ lead to four equally aligned spins on a plaquette forming spin-2's of a chain. Additionally, upon reducing $J_2/J_1 \to 0$, the limit of four decoupled chains is reached, which is a Luttinger liquid LLQ phase and shows no spin gap.

To test these assumptions, we evaluate the uniform spin susceptibility $\chi(T)$ versus temperature T on systems of up to $L = 512$ plaquettes for $J_2 = [1, 0.75, 0.5, 0.25]\ J_1$. The case of $J_1 = J_2$ is shown in the inset of Fig. 5.5(b). Obviously, the system, has a gap. To extract the gap from $\chi(T)$, the same method used in chapter 4 (see section 4.3) is applied where the low-temperature behavior of the susceptibility for $0.0055 \leqslant T \leqslant 0.2 J_1$ is fitted to $\chi(T) \approx e^{-\Delta/T} P_k^l(T)/T$, with $P_k^l(T)$ being a Padé approximant of order $[l, k]$. The errors of such fits - for a particular choice of the fitted temperature interval - can be made less than the QMC's error bars (not shown) which are of the order of 10^{-6}. Fig. 5.5(a) details the finite size scaling of the spin gap for $64 \leqslant L \leqslant 512$. The small oscillations of the data in this plot should not be confused with QMC errors or deviations from simple scaling. Rather they are due to the particular choice of the temperature interval for the Padé fit. As is obvious from this figure, these oscillations are less than the actual finite size corrections. Finally, the main panel of fig. 5.5(b) proves our speculation, namely, the spin gap at $J_1 = J_2$ is close to that of a spin-2 chain [50, 180] and the gap decreases monotonously as $J_2/J_1 \to 0$, where, corresponding to the LLQ, $\Delta(J_2/J_1 = 0) = 0$.

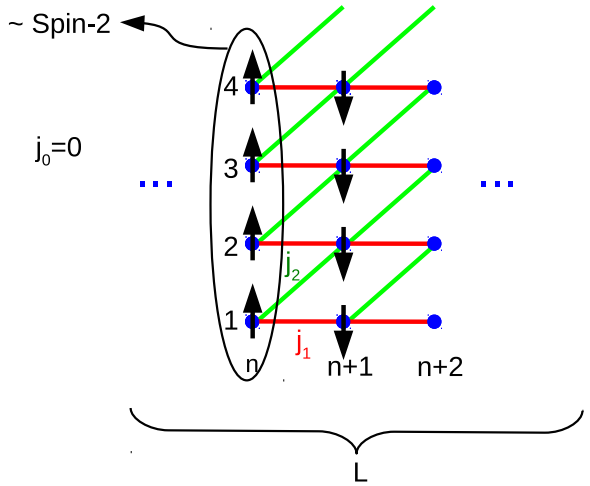

Figure 5.4.: The FFST is mapped into a spin-2 chain within the $(\pi, 0)$ phase where $\mathbf{Q} = (\pi, \pi)$, $(\pi, 0)$, $(0, \pi)$. The polarization of spins are shown by black arrows. Each four spin-1/2's on a plaquette corresponds to one spin-2 of the chain.

5.3.2. Dynamic structure factor

Continuing on the analogy of a crossover from a gapped Haldane-like spin-2 AFM chain to a LLQ for J_2/J_1 ranging from 1 to 0, the dynamical structure factor of the FFST should show signatures of deconfinement from gapped magnon-like modes at $J_2/J_1 = 1$ to a two-spinon continuum as $J_2/J_1 \to 0$.

To analyze this, we investigate the dynamic structure factor $S(\mathbf{Q}, \omega)$ at frequency ω, which we obtain from MaxEnt analytic continuation of imaginary time dynamic structure factor

$$S(\mathbf{Q}, \tau) = \frac{1}{4L} \sum_{\mathbf{r}} e^{i\mathbf{Q}\cdot\mathbf{r}} \langle \mathbf{S}(\mathbf{r}, \tau) \cdot \mathbf{S}(\mathbf{0}, 0) \rangle,$$

evaluated by QMC (see 2.5). This is shown in Fig. 5.6. In all of these plots $Q_y = 0$. The absolute scales on all panels of this figure are adjusted to ensure approximately identical extent of the spectra along the y-axes, which allows to compare the width of the spectral contours. Turning to Fig. 5.6(a-c), we first note that all three contour plots display a certain broadening due to the finite temperature $T = 0.25J_1$. We return to this

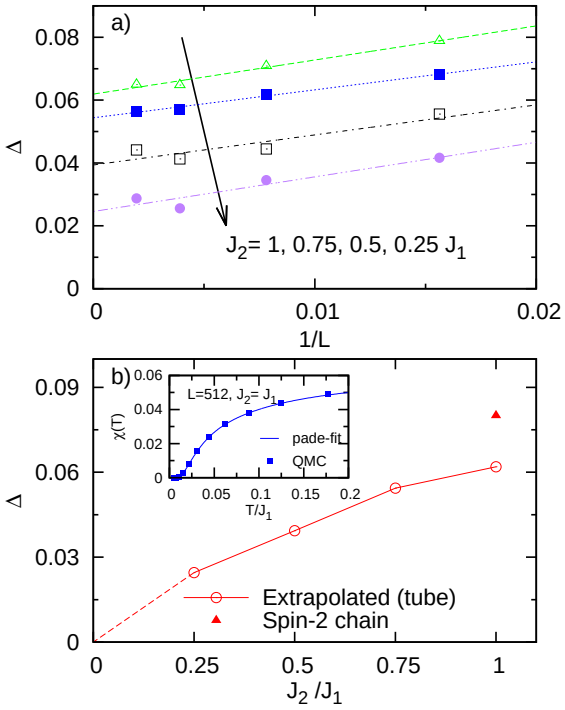

Figure 5.5.: a) Finite size scaling for $64 \leqslant L \leqslant 512$ of the spin gap for different values of J_2. b) $L = \infty$ extrapolated spin gap vs. J_2, as well as spin gap of a spin-2 chain. Inset: susceptibility vs. temperature for $L = 512$ and $J_2 = J_1$ where symbols show QMC data and the solid curve is the Padé fit of the data.

in Fig. 5.6(d-f). Apart from that, at $J_1 = J_2$ the figures show a rather sharp magnon-like mode, similar to the spectra of integer-spin Haldane chains (see chapter 4 of this thesis and Refs. [50, 119, 190]), accompanied by a marked loss of spectral weight as $Q_x \to 0$, which is also a typical feature of integer spin chains. [123] As $J_2 \to 0$, the spectrum starts to broaden in the vicinity of $Q_x = \pi$, resembling a shape very similar to that of the spinon continuum of the spin-1/2 AFM Heisenberg chain [191, 192], exactly as anticipated. To get a better view of the DSF near $Q_x = \pi$, a cut through $S(\mathbf{Q}, \omega)$'s of Fig. 5.6 has been shown in Fig. 5.7. Panel a) of this figure details that although the finite temperature maximum of the dynamic structure factor does not have to coincide with the spin gap, it

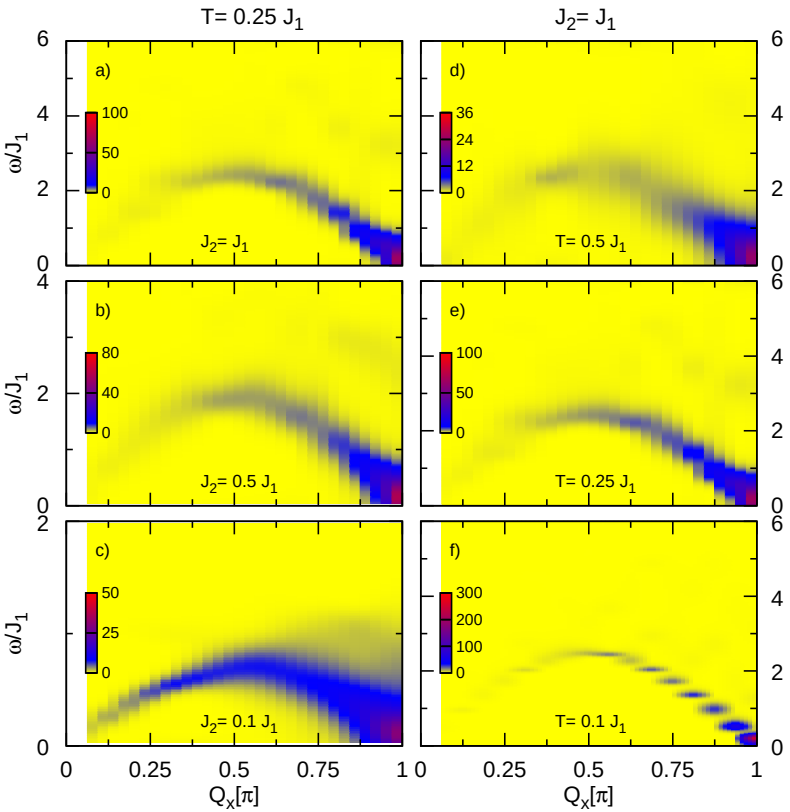

Figure 5.6.: Contour plots of the dynamic structure factor $S(\mathbf{Q},\omega)$ from QMC & MaxEnt for systems of $L = 32$ vs. ω and Q_x at $Q_y = 0$. Panels (a-c): for $J_2/J_1 = 1$, 0.5, and 0.1 at $T = 0.25J_2$. Panels (d-f): for $T/J_1 = 0.5$, 0.25, and 0.1 at $J_2/J_1 = 1$.

nevertheless decreases similar to the latter with respect to J_2/J_1.

Figs. 5.6(d-f) list the temperature dependence of $S(\mathbf{Q},\omega)$ for $J_1 = J_2$. First, these panels clarify, that $T = 0.25J_1$ is a reasonable compromise between finite size effects at $L = 32$ and thermal broadening, i.e., for $T = 0.1J_1$ the line broadening is already less than the

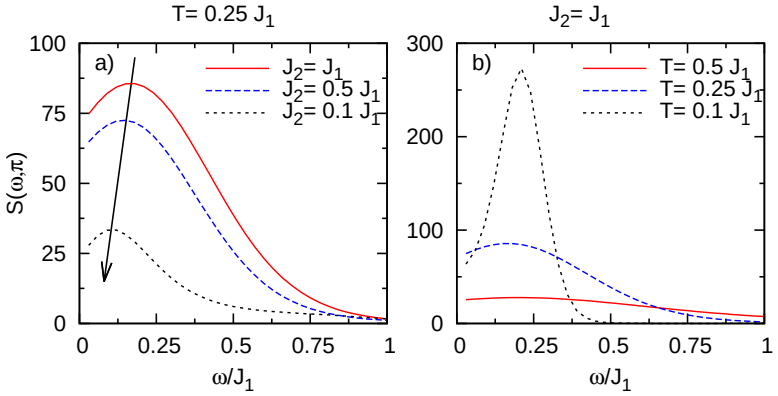

Figure 5.7.: Panel a) inset: $(\pi, 0)$-cut of $S(\mathbf{Q}, \omega)$ with labels referring to panels a)-c). $(\pi, 0)$-cut of $S(\mathbf{Q}, \omega)$ with labels referring to panels d)-f).

finite-size level-spacing. Furthermore, panel b) of Fig 5.7 collects cuts at $Q_x = \pi$, which demonstrate a rather strong temperature dependence of the zone-boundary modes of the FFST for $J_1 \approx J_2 \gg J_0$. This might be of interest in the context of similar observations [31] for four-spin tube compound $Cu_2Cl_4{\cdot}D_8C_4SO_2$.

5.4. Summary

To summarize, we have discussed the quantum phase diagram of a frustrated spin-1/2 four-leg spin tube and contrasted that against the classical picture of the phase diagram. The tube is comprised of a series of 4-leg plaquettes with interleg couplings, J_0, connected via couplings, J_1, and next nearest neighbor couplings, J_2. By setting $J_0 = 1$, we have described the quantum phase diagram of the tube in terms of varying couplings $J_{1,2}$. It consists of a plaquette phase, two strips of weakly coupled plaquettes, an incommensurate phase, and a gapped commensurate phase. We briefly discussed these quantum phases and the transitions between them.

For $J_{1,2} \gg J_0$ (the gapped commensurate phase) , the system can be considered as approximately unfrustrated. We have investigated this regime by quantum Monte-Carlo along the line $0 < J_2/J_1 \leq 1$, setting $J_0 = 0$. Here, calculations of the uniform susceptibility show the tube to have a gap very close to that of AFM spin-2 chains at $J_1 = J_2$,

while for $J_2/J_1 \to 0$ the gap decreases to zero as expected for approaching the Luttinger liquid state. Evaluating the dynamic structure factor, and consistent with a crossover from a 'Haldane-like AFM spin-2 chain' behavior at $J_1 \sim J_2$ to a LLQ at $J_2 = 0$, we observed a deconfinement of the excitations turning from sharp magnon modes into a spinon continuum as $J_2/J_1 \to 0$.

6. N-leg spin-$1/2$ ladders

N-Leg spin ladders are systems consisting of N parallel spin chains which are connected via rung interactions (see Fig. 6.1). Ladders can be regarded as intermediate systems between chains and planes. However their physical properties can not be guessed on the basis of the behaviors of one or two dimensional systems and indeed on the way from one- to two-dimensional quantum magnets, there have been many surprises [193]. Even-leg ladders have a spin gap and short range correlations, whereas odd-leg ladders have no gap and their spin-spin correlations decay as a power law. It is even more surprising, since both limits of ladders, i.e single chains and also two dimensional lattices are gapless. This dramatic difference between odd- and even-leg ladders has been established both theoretically [35, 194] and experimentally [195, 196].

The Hamiltonian of spin ladders can be described by the Heisenberg Hamiltonian,

$$H = J_{\parallel} \sum_{i=1}^{L} \sum_{j=1}^{N} \mathbf{S}_{i,j} \cdot \mathbf{S}_{i+1,j} + J_{\perp} \sum_{i=1}^{L} \sum_{j=1}^{N-1} \mathbf{S}_{i,j} \cdot \mathbf{S}_{i,j+1}, \tag{6.1}$$

where periodic boundary conditions apply along the chains, i.e. $\mathbf{S}_{L+1,j} \equiv \mathbf{S}_{1,j}$. To simplify our analysis, throughout this chapter, we have only considered nearest neighbor exchange interactions and have used equally strong leg and rung couplings, $J_{\parallel} = J_{\perp} = J$.

Thermodynamic properties such as magnetization, specific heat and magnetic susceptibility of ladders have been well studied in the literature. However, less is known about dynamical properties and low-lying excitations of ladders though these are highly desirable to obtain a more complete picture. Therefore in this chapter, we study dynamical structure factor (DSF) of N-leg ladders to address these excitations.

In section 6.1 of this chapter we first give a brief review on the thermodynamic properties of ladders. This is mainly devoted to the temperature dependence of the static susceptibility. Then we present our first calculations on dynamic structure factor of odd- and even-leg ladders in section 6.2 and discuss them in the context of crossover from one to two dimensional spin systems. We compare the dynamic structure factor of the five-leg ladder calculated from QMC to the very recent RIXS data carried on $La_8Cu_7O_{19}$ and finally give a short summary of our findings in section 6.3

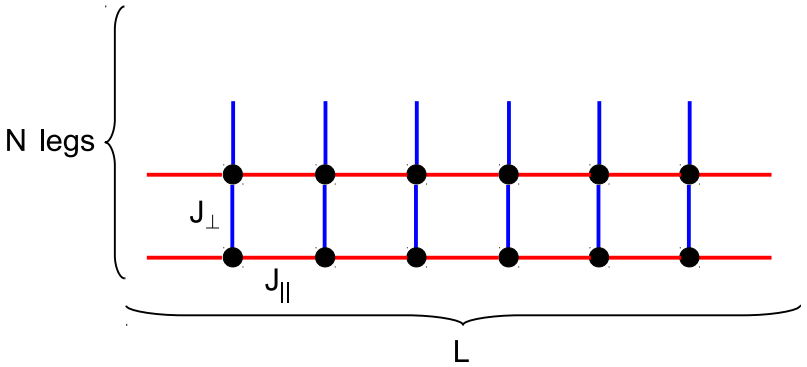

Figure 6.1.: The N-leg spin-1/2 model.

6.1. Magnetic susceptibility of N-leg ladders

The low-temperature thermodynamics of spin-1/2 ladders has been studied using a QMC algorithm in Ref. [35], where the ground state energy as well as magnetic susceptibility of ladders with up to six legs have been investigated. Fig. 6.2 which is reprinted from Ref. [35] shows the susceptibility per rung of isotropic ($J_\perp = J_\parallel = J$) N-leg ladders (N up to six). Ladders of even legs show an exponential drop of susceptibility indicating a spin gap while the susceptibilities of odd-leg ladders remain finite in the zero temperature limit signifying no spin gap. This means that even-leg ladders belong to the universality class of resonance valence bond states (nearest neighbor dimers) while odd-leg ladders remain in the class of single spin-1/2 chain. The value of spin gaps for even-leg ladders has been estimated using various methods [35, 194, 197, 198]. There is a decreasing tendency of the spin gap as the number of legs increases. This is due to the fact that by increasing the number of legs, delocalization of resonance bond singlet states becomes not only along but more and more across the ladder.

6.2. Dynamic structure factor

An interesting issue regarding the crossover from one- to two dimensional systems is the evolution of low-lying excitations with respect to the number of legs. This hasn't been well studied yet mainly because of the numerical difficulties of calculating dynamical properties. The main point of this analysis is the difference between ladders with an even number

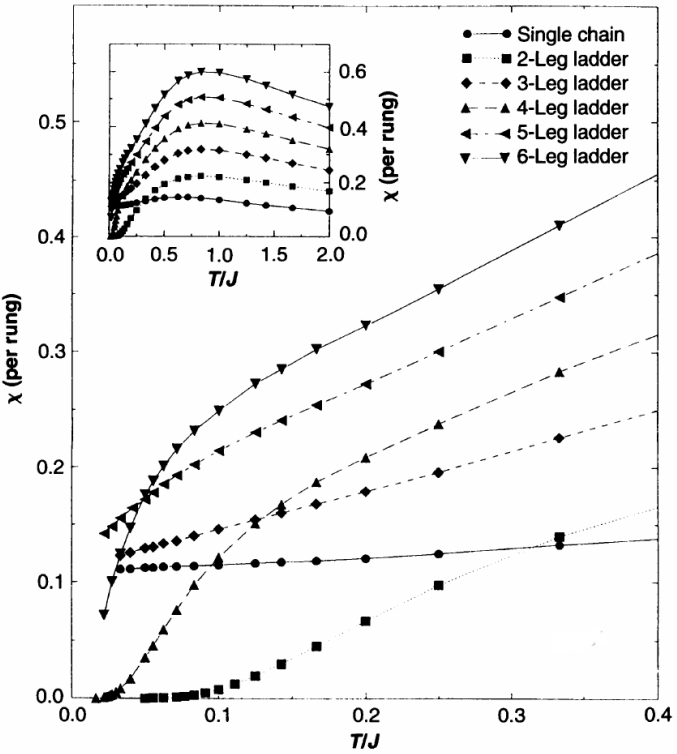

Figure 6.2.: Magnetic susceptibility of a single chain, and isotropic ($J_\perp = J_\parallel = J$) N-leg spin-1/2 ladders reprinted from [35].

of legs versus such with an odd number. For the former magnon-like excitations with a zone-boundary gap scaling inversely exponential in the number of legs is expected, while for the latter, gapless excitations should occur which exhibits signatures of deconfinement for small numbers of legs.

Here we have performed the QMC calculations for the DSF of N-leg ladders with $N = 1, ..., 5$ where $N = 1$ corresponds to a single spin-1/2 chain. This is shown in Fig. 6.3 for isotropic ladders ($J_\perp = J_\parallel = J$) with $N \times 32$ sites and at temperature $T = 0.1J$. All DSF's in this figure are plotted in terms of the longitudinal momentum, Q_x, while the transverse momentum is fixed to zero, $Q_y = 0$. The DSF of the single chain shows clearly

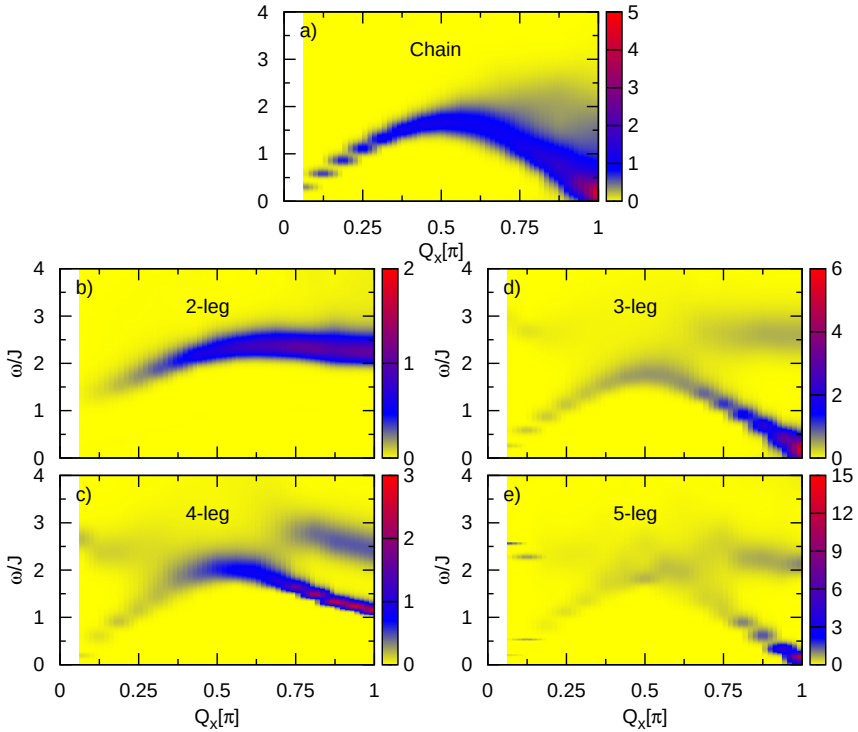

Figure 6.3.: Dynamical structure factor of spin-1/2 chain and ladders with $N \times 32$ sites with $N = 1, 2, 3, 4, 5$ being the number of chains (legs). The spectra are shown in terms of longitudinal momentum Q_x, while the transverse momentum is set to zero, $Q_y = 0$.

the two spinon spectrum. The contribution of the continuum has been exactly calculated in Refs. [183, 199]. At finite temperature, numerical methods such as t-DMRG and QMC have evaluated the DSF for spin-1/2 chains of large sizes [191, 200]. Here, however, we don't want to comment on the quantitative evaluation of the spectrum but rather to make a qualitative comparison between the spectrum of a single chain and that of the coupled chains and study the evolution of excitations as the number of coupled chains increases.

Among ladders, the two-leg ladders are the best studied systems. The DSF of two-leg ladders has been theoretically studied in Refs. [201–206]. Rather similar to the excitations

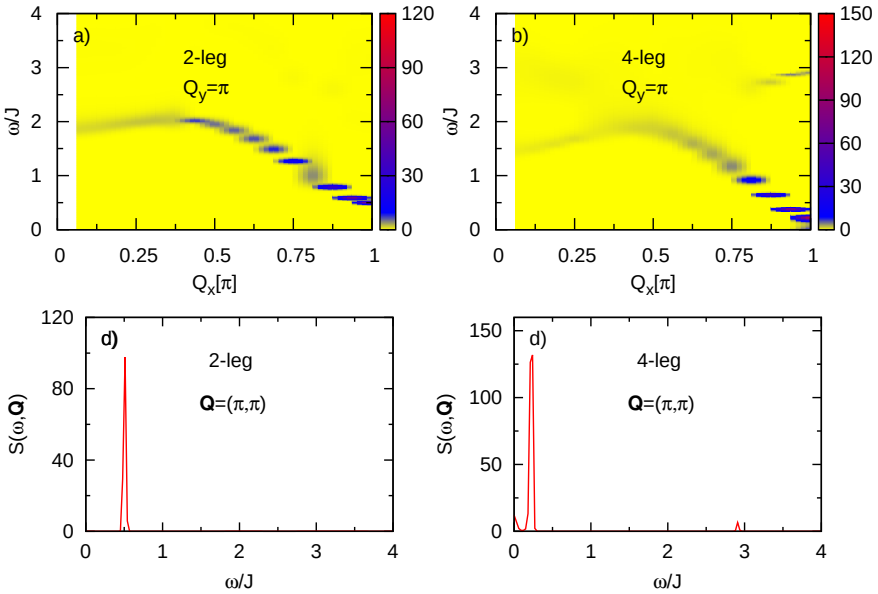

Figure 6.4.: Dynamical structure factor of two- and four-leg ladder systems with 2×32 and 4×32 sites. Panels (a) and (b) show the spectrum with respect to Q_x. In panels (c) and (d), frequency dependence of the spectrum at $\mathbf{Q} = (\pi, \pi)$ is illustrated.

of the spin-1 chain, the first low lying excitation of a two-leg ladder is a single magnon mode and its second excitation is a two-magnon continuum [201–206]. The former one is shaped at the transverse momentum $Q_y = \pi$, while the latter one occurs at $Q_y = 0$. It is also believed that the same characteristics should be identified in large even-leg ladders. In panel (b) and (c) of Fig. 6.3, the $Q_y = 0$ sectors of the spectra for two- and four-leg ladders are plotted. The $Q_y = \pi$ sectors which characterize single-magnon modes are shown in Fig. 6.4. Moving from $Q_y = 0$ to $Q_y = \pi$ is accompanied by changing the wave vector of the lowest energy levels from $Q_x = 0$ to $Q_x = \pi$. As a result of both sectors, the spectrum of the four-leg ladder has similar features as that of the two-leg one, regarding the existence of the single magnon modes and higher energy excitations. Nevertheless, spectral weights and boundaries of these excitations are different. The frequency dependence of the spectrum for even-leg ladders at momentum $\mathbf{Q} = (\pi, \pi)$ is

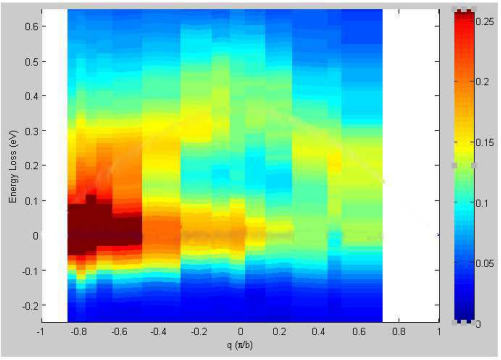

Figure 6.5.: Experimental RIXS spectrum of $La_8Cu_7O_{19}$. Here longitudinal momentum Q_x is shown by q and the transverse one is set to zero, $Q_y = 0$.

plotted in panel (c) and (d) of Fig. 6.4 where most of the spectral weight is collected as a sharp peak. The position of these peaks can be interpreted as an estimate of the spin gap. For two leg ladder, the peak is at $\omega = 0.51$ and in the case of four-leg ladder, it locates at $\omega = 0.22$. Although our system size is a finite one and we are not at the zero temperature limit, these estimations of the gaps are quite similar to those proposed in the thermodynamic limit and at zero temperature [35, 194, 197, 198].

In contrast to two- and four-leg ladders, the lowest excitations of three- and five-leg ladders are gapless (see panel (c) and (e)). It must be noted that the small gap seen in the spectra is a finite size artifact. For our choice of couplings ($J_\perp = J_\parallel = J$), the lower boundary of both spectra almost matches that of the single chain. Additionally, there are clear evidences for higher excitations in the spectra. We assume that the actual weight and boundaries of these excitations depend on the ratio between the two couplings. A proof of this assumption needs further investigation of ladders.

6.2.1. Experimental data on a 5-leg ladder spin system

To classify the recently synthesized transition metal oxide, $La_8Cu_7O_{19}$, regarding its potential similarity to 5-leg ladders, we have compared our QMC calculations to the very recent RIXS experiments carried out on this compound which indeed had been suggested

to be a five-leg ladder system. RIXS is the abbreviation of *Resonant Inelastic X-ray Scattering*. It is a photon-in/photon-out spectroscopy technique where one measures the energy and momentum change of the scattered photons. The difference between the energy and momentum of incident and scattered photons is related to the excitations of the material under study. The RIXS data of $La_8Cu_7O_{19}$ obtained by an experimental group in Dresden [36] are shown in Fig. 6.5. Unfortunately, while there may be some first promising qualitative similarities of our QMC spectra with the experimental data, a direct comparison requires additional information on the actual exchange constants.

6.3. Summary

This chapter was devoted to the spin dynamics of N-leg spin-1/2 ladder systems. First we gave an overview of static properties of such systems based on a QMC study represented in Ref. [35], where temperature dependence of magnetic susceptibility for ladders up to six legs was demonstrated. We discussed the main differences of odd- and even-leg ladders in the thermodynamic limit and addressed the low-lying excitations of ladders and their evolution with respect to the number of legs. To this end, we performed calculations of dynamic structure factor on systems with $N \times 32$ sites with $N = 2, 3, 4, 5$ being the number of legs. Moreover, we compared the excitation spectrum obtained from QMC&MaxEnt with that obtained from the recent RIXS experiment on $La_8Cu_7O_{19}$ suggested to be a five-leg ladder compound.

7. Summary and conclusion

In this thesis, we studied transport, quantum phase diagrams and dynamics of low-dimensional spin systems. The main method used to obtain physical quantities was a quantum Monte Carlo (QMC) method based on the stochastic series expansion (SEE). We explained this method and the maximum entropy (MaxEnt) technique used for analytical continuation of the imaginary time QMC data in chapter 2 of this thesis. The low-dimensional spin systems considered in the thesis consist of the two fundamental spin chains, i.e. the antiferromagnetic spin-1/2 and spin-1 chains together with two more complicated quasi one-dimensional spin systems, namely a frustrated four-leg spin tube and N-leg spin-1/2 ladders. Here, we will briefly outline our main results and conclusions regarding each of these spin systems.

In chapter 3, we studied spin transport of the antiferromagnetic spin-1/2 Heisenberg chain at finite temperatures. An open question in this context is the regime of transport, that is, if spin transport at finite temperatures is diffusive or ballistic. In the case of zero temperature, an exact Bethe ansatz method has given a finite Drude weight, implying a ballistic regime. At finite temperature however, different calculations of Bethe ansatz as well as various numerical and analytical approaches have led to contradicting results. We addressed this question by studying the long-wavelength and finite frequency spectrum of the chain and following the recent proposal for transport in the spin-1/2 chain, namely the coexistence of diffusive and ballistic transport channels at finite temperatures [26]. We used a method described in Ref. [28] to approve the existence of the diffusive channel and obtain the extent of diffusivity. This method is a combination of the QMC method and results from a perturbation theory based on bosonization. Through this combination, one can access the spin current relaxation rate of the system. We went beyond the confinements of Ref. [28], i.e. no anisotropy, no magnetic field and only one system-size, by doing a finite size scaling and studying field and anisotropy dependence of the spin current relaxation rate. As a result of a finite-size scaling, we showed that the current relaxation rate for the isotropic chain is independent of the system size and proved that the corresponding diffusion kernel has no frequency dependence. The method is designed such that one can reproduce the dynamical structure factor (DSF) of the system using the calculated spin current relaxation rate without involving the analytical continuation problem. We compared this DSF with the exact spectrum calculated using a full diagonalization of the Hamiltonian for a finite system-size $L = 18$ at some intermediate

temperatures, $T = J/[1, 2, 3]$ and found good agreement between these two spectra, as temperature decreases down to the valid limit of bosonization. This can be regarded as a consistency check on our method.

We also studied the role of an external magnetic field on the spin current of the system in this chapter and found that the dissipation of the spin current or identically the spin current relaxation rate is decreasing as the magnetic field increases so that it is nearly zero close to the saturation field ($h_c = 2J$). Our findings do not contradict the Mazur's inequality which determines a finite lower bound for the Drude weight at finite magnetic fields, but rather suggest the possibility of a diffusive transport living together with a finite Drude weight. We went further by applying our approach to the spin-1/2 chain with anisotropy, $0 < \Delta < 1$. As a result, we found that there exists a finite relaxation rate which decreases continuously, as Δ moves away from the isotropic point. and it becomes zero at $\Delta = 0$, where the system can be described by non-interacting spinless fermions corresponded to a pure ballistic regime. These results are consistent with the recent results from bosonization and time-dependent density matrix renormalization group (tDMRG).

In chapter 4, we studied our second example of one dimensional systems, namely the antiferromagnetic spin-1 Heisenberg chain. As the central new ingredient, we allowed for simultaneous single-ion anisotropy and longitudinal magnetic field in the model. The main goal in this chapter was to study the low-lying magnetic excitations of the chain and specially the evolution of these excitations in terms of single-ion anisotropies and magnetic fields. First, we revealed the quantum phase diagram of the chain with respect to the anisotropy and the magnetic field, which comprises the Néel, Haldane, Luttinger Liquid, and Large-D phase. The transitions between these phases were obtained by analyzing the spin gap together with the correlation functions of the system. Then, we discussed the spin dynamics of the chain in the context of the corresponding quantum phases. To this end, we obtained the transverse dynamic structure factor of the chain using the QMC method and the MaxEnt technique. As a result, we showed a very pronounced single-magnon mode with a maximum spectral weight at momentum $q = \pi$ in the excitation spectrum. We also showed how this magnon mode changes as a function of magnetic field and anisotropy. The overall effect of magnetic field on the magnon mode can be described as follows. By increasing magnetic field, the magnon mode splits into two branches due to the Zeeman effect. As the magnetic field exceeds the Haldane gap, the lower energy branch of the mode at $q = \pi$ crosses the ground state and starts to own the maximum extent of the spectral weight, while the other branch is smearing. The impact of anisotropy on the other hand is so that, as one transfers from a finite easy-axis anisotropy to a finite easy-plane one, the magnon mode at $q = \pi$ moves from larger frequencies to small ones. This corresponds to the change of spin gap in the Haldane phase.

In addition to the single magnon mode, we have established the existence of multi-particle

excitations in the spectrum. One of these excitations is the two-magnon continuum which can be regarded as the second lowest lying type of excitation of the chain, forming at low momenta of the spectrum. At zero magnetic field and in the isotropic point, the lower energy boundary of the two-magnon continuum in the limit $q \to 0$ lies at 2Δ, where Δ is the Haldane gap. However, boundaries and weights of this continuum changes non-monotonously as a function of magnetic field and anisotropy. Another low-lying excitation of the spectrum is a continuum which forms at $q = \pi$ and is most likely a three-magnon continuum. The spectral weight of this continuum is much smaller than that of the single-magnon mode and probably that is the reason that many numerical calculations and experiments have not been able to observe it. We also compared our spectra with that calculated from other theoretical and numerical methods including the NLσ model, free boson and tDMRG methods at the isotropic point and zero magnetic field. Despite the fact that QMC calculations were done at finite temperature ($T = 0.1J$) while the other methods have been performed at zero temperature, we found good agreement between their spectra of the spin-1 chain.

An experimental quantity which can be calculated by a summation of DSF's over all wave vectors, is the NMR rate. We checked the field dependence of the NMR rates for various values of anisotropy against those predicted by two other results based on field theoretical approaches and spin-wave theory. Consistency was established in the regime of fields small compared to the spin gap.

We devoted chapter 5 of the thesis to the study of the quantum phases and dynamics of a frustrated four-leg spin-1/2 tube, where spins are all antiferromagnetically coupled. The tube consists of a series of 4-leg plaquettes with interleg couplings J_0, which are connected to each other via couplings J_1. A next nearest neighbor coupling J_2 (connecting legs l of plaquettes n to legs $l+1$ of plaquettes $n+1$) makes the tube geometrically frustrated. By setting $J_0 = 1$, the quantum phase diagram of the model as a function of the exchange couplings $J_{1,2}$ has been obtained [34] and the main similarities and discrepancies between that and the tube's phase diagram in the classical limit have been discussed. The point $J_{1,2} = 0$ in the quantum phase diagram is a gapped phase of decoupled plaquettes. This plaquette phase (PQ) is adiabatically connected to two strips of weakly coupled plaquettes parallel to each of $J_{1(2)}$-axis. Along the line of $J_1 = J_2$ and at the point of maximum frustration, $J_{1,2} = 1$, there is a first order transition from PQ into an incommensurate phase which survives up to $J_{1,2} \sim 1.3$, where there is a weak first order transition into a gapped commensurate phase, $J_{1,2} > 1.3$. This incommensurate phase is separated form the two strips with straight lines (of first order transition) along $J_{1(2)} = 1$. The overall extent of the incommensurate phase in the quantum phase is strongly reduced as compared to that of the classical one.

In the strong leg coupling regime, we used the QMC method to investigate an unfrustrated phase of the tube, where the on-plaquette exchange coupling is too weak, $J_0 \ll J_{1,2}$. By

setting $J_0 = 0$, we studied the evolution of the spin gap and spin dynamics of the system along the line $0 < J_2/J_1 \leq 1$. Regarding the spin gap, calculations of the uniform susceptibility showed that the tube at $J_2 = J_1$ has a gap very close to that of AFM spin-2 chains, and this gap decreases to zero as $J_2/J_1 \to 0$, where the tube is reduced to decoupled spin-1/2 chains. In other words, there exists a crossover from a gapped Haldane phase to a gapless Luttinger liquid phase, as J_2/J_1 ranges from 1 to 0. This crossover was also shown in the DSF of the tube evaluated using QMC plus MaxEnt. The excitation spectrum has a sharp magnon-like mode at $J_2/J_1 = 1$ while it becomes more and more similar to a two-spinon continuum as $J_2/J_1 \to 0$. Moreover, we obtained the temperature dependence of the DSF at $J_1 = J_2$ and showed a broadening of the spectrum as a result of temperature increase. A similar type of behavior has been observed in the neutron scattering results of a four-leg spin tube compound $Cu_2Cl_4{\cdot}D_8C_4SO_2$ [31].

Finally, we investigated the dynamics of N-leg spin-1/2 ladder systems in chapter 6 of this thesis. We confined ourselves to ladders of isotropic interactions, where leg and rung interactions are equal. The main purpose of this chapter was to study the low-lying excitations of N-leg ladders and their evolution with respect to the number of legs. To this end, we performed QMC calculations on systems with $N \times 32$ sites with $N = 2, 3, 4, 5$ being the number of legs, and obtained their DSF's using the MaxEnt technique. The DSF of a single spin-1/2 chain with 32 sites was also calculated in order to make a comparison between magnetic excitations of chains and ladders. As a result, we showed that the excitation spectrum of two- and four-leg ladders have similar features, namely the existence of sharp magnon modes as well as high energy excitations. However, the spectral weights and boundaries of these excitations are different. In contrast to two- and four-leg ladders, the lowest excitations of three- and five-leg ladders were found to be gapless similar to that of the single chain. Signatures of high energy excitations are also evident in the spectrum of these ladders. Moreover, we made a preliminary comparison between the QMC spectrum of the five-leg ladder and the excitation spectrum calculated recently by RIXS experiment on $La_8Cu_7O_{19}$ which has been suggested to be a five-leg ladder compound. Nevertheless, in order to make a conclusive statement about this comparison, further investigations are required.

A. Appendix to chapter 5

A.1. Methods

A.1.1. Series expansion

Our Series expansion (SE) calculations start from the limit of isolated plaquettes. To this end, we decompose the Hamiltonian of the FFST into

$$H = H_0 + V(J_1, J_2), \tag{A.1}$$

where H_0 represents decoupled plaquettes and $V(J_1, J_2)$ is the part of Hamiltonian that connects plaquettes via J_1, J_2 couplings.

It is simple to show that each plaquette has four equally spaced energy levels which in turn renders the levels structure of H_0 to be equidistant. This allows to sort the spectrum of H_0 in a block-diagonal form, where each block is labeled by an energy quantum-number Q. In this way, Q=0 represents the ground state (*vacuum*), i.e. all plaquettes are in the state of minimum energy. Q=1 sector is composed by states obtained by creating (from vacuum state) one-elementary excitation (*particle*) on a given plaquette, and so on. It is clear that $Q \geq 2$ will be of multiparticle nature.

In general, the action of $V(J_1, J_2)$ mixes different Q-sectors, so that the block-diagonal form of H_0 is not conserved in H. However, it has been shown [207] that for the present type of Hamiltonians, it is possible to restore block-diagonal form by the application of continuous unitary transformations, using the flow equation method of Wegner [208]. It basically consists in transforming H onto an effective Hamiltonian H_{eff} which is block-diagonal in the quantum number Q. This transformation can be achieved exactly in terms of a SE in $J_{1,2}$ leading to

$$H_{\text{eff}} = H_0 + \sum_{n,0\leq m\leq n} J_1^{n-m} J_2^m C_{n,m}\,. \tag{A.2}$$

Here, $C_{n,m}$ are weighted products of terms in $V(J_1, J_2)$ which conserve the Q-number, with weights determined by recursive differential equations (see Ref. [207] for details).

Due to Q-number conservation, several observables can be calculated directly from $H_{\rm eff}$ in terms of a SE in $J_{1,2}$. For systems with coupled spin-plaquettes continuous unitary transformations SE has been used for one [209], two [210–213] and three [214] dimensions. For the present model we have performed $O(7)$ and $O(6)$ SE in $J_{1,2}$ for ground state energy ($Q = 0$) and for $Q = 1, 2$ sectors, respectively. We refer for technical details about the calculation to Ref. [33].

A.1.2. Schwinger bosons

Schwinger bosons [215] are used to represent spins at site l via spinfull bosons $b_{l\sigma}^{(\dagger)}$, with $\sigma = \uparrow\downarrow$ or ± 1, through $S_l^\alpha = \frac{1}{2}\sum_{\mu\nu} b_{l\mu}^\dagger \sigma_{\mu\nu}^\alpha b_{l\nu}$, where $\sigma_{\mu\nu}^\alpha$ are the Pauli matrices and $\alpha = x, y, z$. The Hilbert space dimension of spin-S multiplets is enforced through the constraint $\sum_\sigma b_{l\sigma}^\dagger b_{l\sigma} = 2S$. In terms of Schwinger bosons, the exchange interaction can be written as [215, 216]

$$\mathbf{S}_l \cdot \mathbf{S}_m = : \hat{B}_{lm}^\dagger \hat{B}_{lm} : - \hat{A}_{lm}^\dagger \hat{A}_{lm} \,, \tag{A.3}$$

with the bond operators $\hat{B}_{lm}^\dagger = \frac{1}{2}\sum_\sigma b_{l\sigma}^\dagger b_{m\sigma}$ and $\hat{A}_{lm} = \frac{1}{2}\sum_\sigma \sigma b_{l\sigma} b_{m-\sigma}$ and normal ordering ::. Eqn. (A.3) has been used for various $SU(2)$ invariant and large N factorization schemes [216–221]. We follow [219–221] and introduce the *bond mean fields* $B_{lm} = \langle \hat{B}_{lm} \rangle$ and $A_{lm} = \langle \hat{A}_{lm} \rangle$, accounting for ferromagnetic (FM) and AFM correlations on equal footing. For the FFST, we focus on homogeneous mean fields, implying *six* parameters:

$$B_{n=0,1,2} \qquad A_{n=0,1,2} \,, \tag{A.4}$$

where $n = 0, 1, 2$ corresponds to the three exchange links $\mathbf{r}_l - \mathbf{r}_m = \mathbf{r}_n = \mathbf{R}_y$, $\mathbf{R}_x$, $\mathbf{R}_x + \mathbf{R}_y$. Fourier transformation, $b_{l\sigma} = \sum_{\mathbf{k}} e^{i\mathbf{k}\cdot\mathbf{r}_l} b_{\mathbf{k}\sigma}/\sqrt{N}$, leads to a bilinear mean field Hamiltonian, which can be diagonalized by standard Bogoliubov transformation, i.e. $b_{\mathbf{k}\sigma} = u_{\mathbf{k}} a_{\mathbf{k}\sigma} + i\, v_{\mathbf{k}} a_{-\mathbf{k}-\sigma}^\dagger$, with $u_{\mathbf{k}}^2 - v_{\mathbf{k}}^2 = 1$ yielding

$$\begin{aligned} H_{\rm MFT} &= \sum_{\mathbf{k}\sigma} E_{\mathbf{k}} \left(a_{\mathbf{k}\sigma}^\dagger a_{\mathbf{k}\sigma} + \frac{1}{2} \right) + \sum_n J_n \left(|A_n|^2 - \right. \\ &\quad \left. |B_n|^2 \right) + 2N\lambda(S + \frac{1}{2}) \,, \end{aligned} \tag{A.5}$$

where $E_{\mathbf{k}} = [\gamma_B(\mathbf{k})^2 - \gamma_A(\mathbf{k})^2]^{1/2}$ is the quasiparticle dispersion with $\gamma_A(\mathbf{k}) = \sum_n J_n A_n \sin(\mathbf{k}\cdot\mathbf{r}_n)$ and $\gamma_B(\mathbf{k}) = \sum_n J_n B_n \cos(\mathbf{k}\cdot\mathbf{r}_n) - \lambda$. We assume B_n, A_n to be real. λ is a Lagrange parameter to enforce the constraint on the *average*. Selfconsistency, i.e. $\partial\langle H_{\rm MFT}\rangle/\partial x = 0$,

with $x{=}A_n, B_n$, and λ leads to

$$A[B]_n = \frac{1}{2N}\sum_{\mathbf{k}} \frac{\gamma_{A[B]}(\mathbf{k})\,\sin[\cos](\mathbf{k}\cdot\mathbf{r}_n)}{E_{\mathbf{k}}} \tag{A.6}$$

$$(S+\frac{1}{2}) = \frac{1}{2N}\sum_{\mathbf{k}} \frac{\gamma_B(\mathbf{k})}{E_{\mathbf{k}}}, \tag{A.7}$$

where eqn. (A.6) yields six equations for A_n and B_n, by replacing terms with their square bracketed successors.

To obtain A_n, B_n, and λ we use two numerical approaches: (i) we solve eqn. (A.6, A.7) in the thermodynamic limit, and (ii) we minimize the vacuum energy of eqn. (A.5) with respect to A_n, B_n, and λ on large finite lattices with $N \leqslant 10^4$ sites and periodic boundary conditions. The results from both approaches agree.

In the present work we set $S = 1/2$ and study the ground state energy, the quantum phases, and the spin correlation functions arising from A_n, B_n, and λ.

A.1.3. Exact diagonalization and density matrix renormalization group

All DMRG and ED calculations employ the open source packages ALPS [222] and SPINPACK [223]. We refer to their documentation. In DMRG specifications, m refers to the number of states kept during sweeps.

A.2. Quantum phase diagram

In the following, we gather information from various complementary methods to develop a quantum version of the phase diagram of the FFST. The discussion focuses on the strong and intermediate on-plaquette exchange and comprises an analysis of the ground state energy using DMRG, SE, SBMFT, and ED, followed by an evaluation of the phase diagram from SBMFT, and finally a DMRG study of correlation functions and structure factors.

To begin, we note that in the quantum case and at the points $J_{1(2)} \to \infty$, $J_{2(1)} = 0$ the FFST is in a Luttinger liquid (LLQ) state. Staying on either of the two axes ($J_{1(2)} \neq \infty, J_{2(1)} = 0$) , the system is unfrustrated, the interleg coupling is relevant, and the FFST

opens a spin gap. This gapped phase is adiabatically connected to that of unfrustrated weakly coupled plaquettes ($J_{1(2)} \ll 1, J_{2(1)} = 0$) which has been studied extensively in Refs. [224, 225]. The frustrated weakly coupled plaquette regime shows no transition between a (π, π) and $(0, \pi)$ phase, rendering the diagonal line in the lower left corner of Fig. 5.2 a classical-only effect.

A.2.1. Ground state energy

A natural question arising is, how far the weakly coupled plaquette phase extends away from the $J_{1(2)}$ axes lines and if its break down is of first or second order. We check this in two ways, considering the ground state energy e_0 versus $J_{1,2}$ and the static structure factor. The results for e_0 are summarized in Fig. A.1. It depicts the results from different techniques, along two paths in parameter space. Panel (a) is along the J_1-axis, while panel (b) diagonal path $J_1 = J_2$ of maximum frustration.

Along the J_1-axis, panel (a) the energy is a smooth function. All methods are in satisfactory agreement up to $J_1 \approx 0.7$. At this point the bare SE shown, which has been obtained up to $O(7)$ (section A.1.1), loses convergence, while the other techniques continue to agree throughout the range shown. We note that finite size effects on the DMRG and ED are expected to be small since the system is gapped.

Along the line of maximum frustration, Fig. A.1 (b), the energy as obtained from DMRG and ED shows an obvious discontinuity in its first derivative at $J_1 \approx 1$. This signals a first order quantum phase transition. Remarkably this point is rather close to the classical tricritical point, separating (π, π), $(0, \pi)$ and spiral classical phases of Fig. 5.2. By construction, SE based on a single unperturbed starting state is unable to detect this transition, which is consistent with Fig. A.1 (b), where the SE agrees perfectly with DMRG and ED exactly up to the kink in e_0. Finally SBMFT is very close to DMRG and ED in this panel beyond the transition, however it underestimates the energy severely at smaller $J_1 = J_2$. We will return to this later.

Using DMRG ground state energies, we follow the first order transition in the $J_{1,2}$-plane. This is shown in the inset of Fig. A.1 (b). Apart from a very small curvature in the immediate vicinity of the transition point on the diagonal $J_1 = J_2$, the plaquette phase border is composed of almost straight lines: $J^c_{2(1)}(J_{1(2)}) \approx 1$ for $1 \lesssim J_{1(2)} \lesssim 1.5$. For values of $J_{1(2)} \gtrsim 1.5$, the error on the detection of the kink from our numerical data is too large to make definite conclusions. While this is identical to previous findings in Ref. [33], our evaluation of the static structure factor shows (later on) that the first order transition is very likely to extend at least up to $J_{1(2)} \approx 5$.

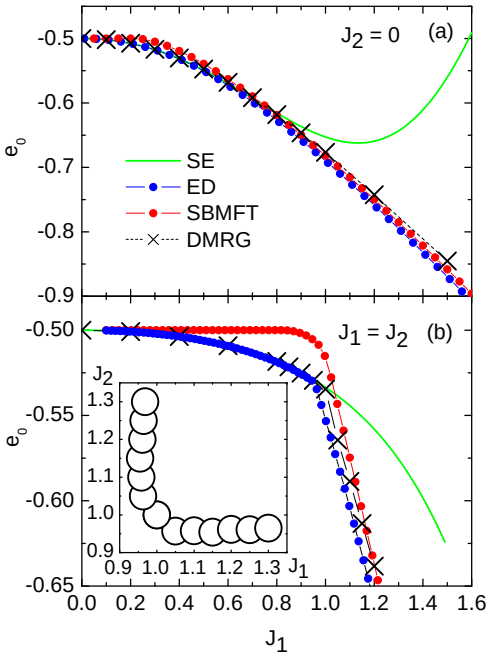

Figure A.1.: Ground state energy per site e_0 for $J_0 = 1$. Panel (a) e_0 vs. J_1 at $J_2 = 0$. Panel (b) e_0 vs. $J_2 = J_1$. Green solid: plaquette SE at $O(7)$. Dotted blue (red): ED with L=6 and PBC (SBMFT with L=400 and PBC). Large crosses: DMRG with L=20, m=300, and OBC. Inset in (b): first order transition line in the $J_{1,2}$-plane.

In summary, ground state energy calculations seem consistent with a plaquette phase extending throughout two strips of width of order unity parallel to each of the $J_{1(2)}$-axis, at least up to intermediate $J_{1(2)}$. Finally, there are *no* signatures of additional first order transitions, separating a putative incommensurate and $(\pi, 0)$-phase. In view of this 'missing' second incommensurate-to-commensurate transition, we will consider also real space correlation functions and static structure factors later on.

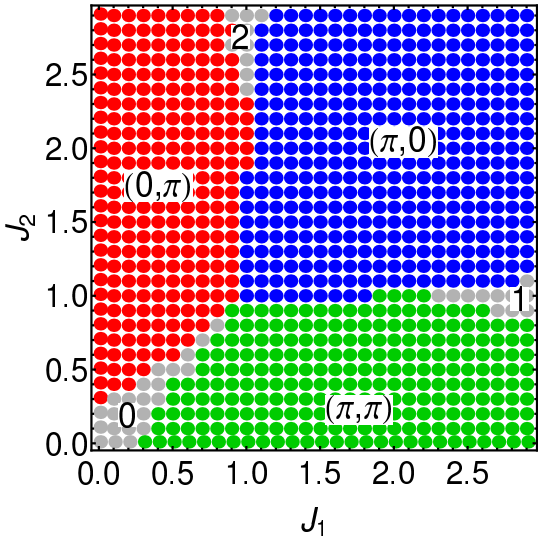

Figure A.2.: SBMFT phase diagram. Pitch vectors label short range spin correlations. Grey regions correspond to unphysical 'decoupled chain' phases

A.2.2. SBMFT phase diagram

Next we turn to the phase diagram as obtained from SBMFT. We use an $SU(2)$ invariant decoupling scheme described in section A.1.2 focusing on solutions with homogeneous mean fields. Apart from one Lagrange multiplier to fix the local spin, this leads to *six* bond parameters $B_{n=0,1,2}$ and $A_{n=0,1,2}$, one B_n and one A_n for each of the three non-equivalent exchange links in Fig. 5.1. B_n refer to triplet, and A_n to singlet spin correlations. Solving the self consistency Eqs. (A.6,A.7) either in the continuum limit, or, equivalently minimizing the energy of Hamiltonian (A.5) on sufficiently large finite FFSTs, we find the quantum phase diagram shown in Fig. A.2 for $0 \leqslant J_{1,2} \leqslant 3$.

First, we emphasize, that the SBMFT solutions in all of the parameter space investigated remains gapped. That is, there is no condensation of Schwinger bosons, and correspondingly no long-range magnetic order (LRO). This is to be expected in 1D. The 'pitch' vector labels in Fig. A.2 refer to short range correlations as depicted in Fig. A.3, which shows a vertical cut through the phase diagram of Fig. A.2 close to $J_1 = 0$. In the 'red' phase the AFM bond mean fields along the plaquette rungs and the diagonal J_2-links are finite, while there are ferromagnetic correlations along the J_1-links. In this sense this is a

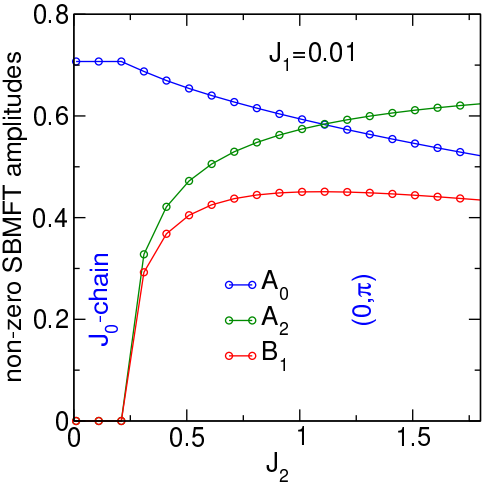

Figure A.3.: Non-zero bond mean field parameters within the phases of Fig. A.2 versus J_2 for $J_1 = 0.01$.

$(0, \pi)$-phase, similar to Fig. 5.2. The same notion applies to the $(\pi, 0)$- and (π, π)-phase. All transitions between red, green, and blue phases in Fig. A.2 are of first order.

Fig. A.3 clearly shows, that upon lowering J_2 the FFST continuously evolves into a weakly coupled plaquette regime in the red phase. That is, for $J_2 \lesssim 1$, the singlet amplitudes A_0 on the plaquette rungs increase up to their maximum possible value of $1/\sqrt{2}$ at $J_2 \approx 0.25$, while the inter-plaquette coupling amplitudes jointly decrease to zero. Qualitatively similar behavior applies to J_1 values other than that chosen in Fig. A.3 within the red phase and within the green phase by interchanging $J_1 \leftrightarrow J_2$ and $A_2, B_1 \leftrightarrow B_2, A_1$.

However, as signaled by the grey phases in Fig. A.2, and from Fig. A.3, the SBMFT overestimates the stability of decoupled singlet sub-units within the FFST - such as the four-spin-plaquette. These grey phases are artifacts of the SBMFT which are reached through second order transitions. As Fig. A.3 shows, SBMFT allows for small but finite parameter ranges with only one non-zero and maximized AFM bond mean field, implying that the FFST decomposes into a collection of completely decoupled J_0-, J_1-, or J_2-chains. That is, in the grey regions, the SBMFT is incapable to lower the system energy by quantum fluctuations between the latter decoupled chains. This is the reason for the poor SBMFT ground state energy in Fig. A.1(b).

To conclude, also the SBMFT phase diagram is consistent with a gapped plaquette phase

extending throughout two strips of width of order unity parallel to each of the $J_{1(2)}$-axis, and at least up to intermediate $J_{1(2)}$. Within this plaquette phase $(\pi,\pi)((0,\pi))$-correlations increase, as $J_1(J_2)$ increase. Moreover SBMFT shows a $(\pi,0)$-phase, similar to the classical case, however with a spin gap and without long range order. Finally, SBMFT shows no incommensurate phase.

A.2.3. Correlation functions and static structure factor

In this section, we turn to the question of a potentially incommensurate phase in the quantum case. To this end, we first look at static real-space correlation functions:

$$C(\mathbf{r}) = \langle \mathbf{S}(\mathbf{r}) \cdot \mathbf{S}(\mathbf{0}) \rangle, \tag{A.8}$$

where $\mathbf{r}$ is a site on the lattice and $\langle \ldots \rangle$ the ground-state expectation value. Due to the $SU(2)$ invariance of the model, only the correlation function $C_z(\mathbf{r}) = \langle S_z(\mathbf{r}) S_z(\mathbf{0}) \rangle$ needs to be considered, which satisfies $C_z(\mathbf{r}) = C(\mathbf{r})/3$. We will contrast results from DMRG against those from SBMFT.

SBMFT results are obtained with periodic boundary conditions (PBC). For best convergence, DMRG employs open boundary conditions (OBC) along the chain. That is, correlations depend on the reference site. To minimize edge effects, we have chosen a reference site $\mathbf{0} = (L/2, y)$ in the middle of any of the $y = (1, \ldots, 4)$ equivalent chains of the tube. Panels (b), (c) of Fig. A.4 show $C(x)$ along one of those equivalent chains, say $\mathbf{r} = (L/2 - 1 + x, 1)$ and $\mathbf{0} = (L/2, 1)$.

We have focused on three particular values of $J_{1,2}$ as shown in the schematic phase diagram in panel (a). Two of them lie regions where both, the classical and the SBMFT suggest strongly commensurate correlations, and one is shortly *above* the first order transition of Fig. A.1, where the classical state is incommensurate.

Fig. A.4(b) evidences clearly commensurate correlations along the tube's legs for the regions of the black and red open circles in Fig. A.4(a) and obviously a remarkably good agreement between DMRG and SBMFT. Small deviations between DMRG and SBMFT at the ends of the chain are to be expected from the difference in boundary conditions. We have checked, that the wave vector of the commensuration is $(\pi,\pi)((\pi,0))$ for the black (red) circles of A.4(a) by also scanning along other real-space directions on the FFST. Clearly $C(x)$ decays as a function of x. While the system sizes for the DMRG are too small to extract the functional form of this decay, $C(x) \sim \exp(-x/\xi)$ is found in the SBMFT, where ξ is a finite correlation length related with the inverse of the energy gap. This is consistent with gapped phases and no LRO, as has already been alluded to in SBMFT study.

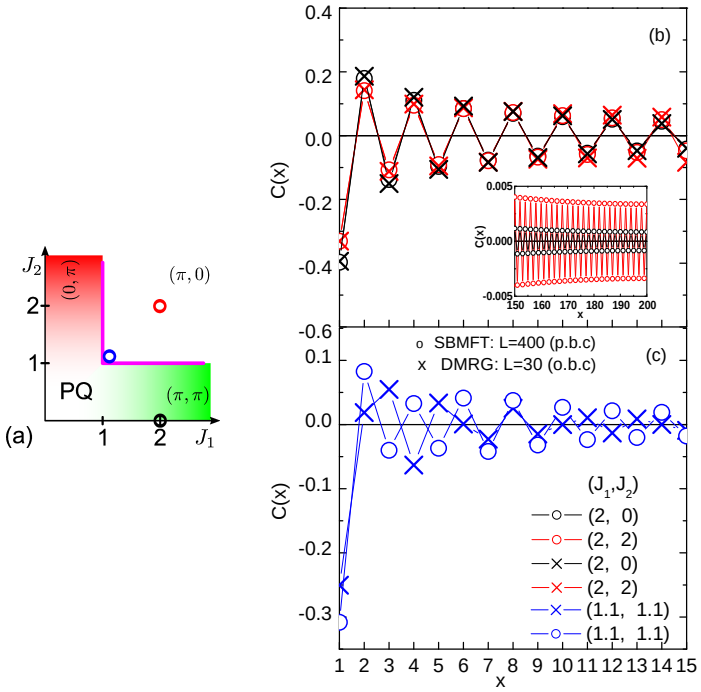

Figure A.4.: (a) Open colored circles: $J_{1,2}$ values chosen for panels (b), (c). PQ refers to weakly coupled plaquette phase, with predominant (π,π) (green gradient) or $(0,\pi)$ (red gradient) correlations. Magenta line: first order transition evidenced from DMRG in Fig. A.1(b, inset) and SBMFT in Fig. A.2. (b) and (c) $C(x) = \langle \mathbf{S}(x,1)\cdot\mathbf{S}(L/2,1)\rangle$ vs x. Curve colors correspond to choices in (a). Crosses: DMRG for L=30, m=300, and OBC. Circles: SBMFT for L=400 and PBC. Inset in (b): SBMFT at large distance.

The situation changes drastically at the blue open circle in fig. A.4(a). Here, DMRG evidences a strongly decaying, *incommensurate* x-dependence in Fig. A.4(c), while SBMFT continues to display commensurate $(\pi,0)$-correlations, as to be expected from the phase diagram, Fig. A.2. This proves, that SBMFT fails to produce the proper spin-correlations shortly above the first order transition out of the plaquette phase and suggests the presence of an incommensurate region also in the quantum version of the FFST.

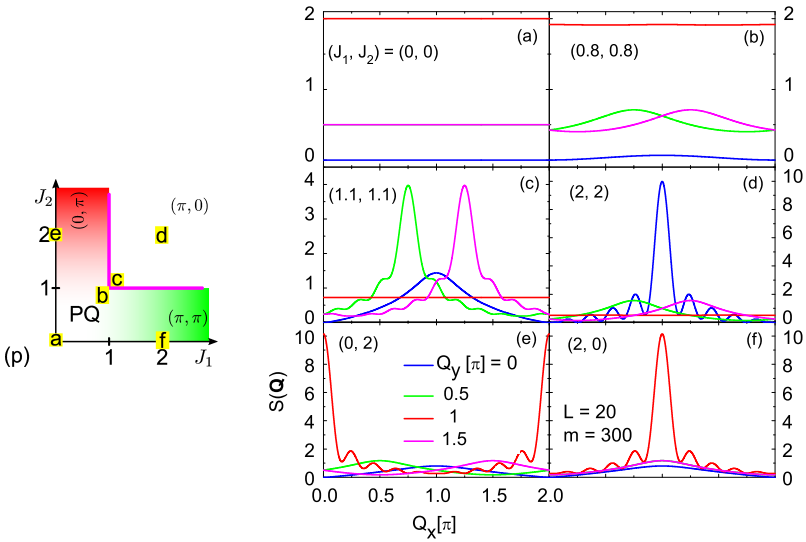

Figure A.5.: (p) Letters on yellow background: $J_{1,2}$ choices for panels (a)-(f). PQ refers to weakly coupled plaquette phase, with predominant (π,π) (green gradient) or $(0,\pi)$ (red gradient) correlations. Magenta line: first order transition evidenced from DMRG, Fig. A.1(b, inset) and SBMFT Fig. A.2. Panels (a)-(f): structure factor $S(\mathbf{Q})$ from DMRG (L=20, m=300, OBC) for $J_{1,2}$ as in (p). Blue, green, red, and magenta lines refer to $Q_y = (0,1,2,3)\pi/2$.

To further corroborate this, we now calculate the static structure factor

$$S(\mathbf{Q}) = \frac{1}{4L}\sum_{\mathbf{r}} e^{i\mathbf{Q}\cdot\mathbf{r}}\langle \mathbf{S}(\mathbf{r})\cdot\mathbf{S}(\mathbf{0})\rangle, \tag{A.9}$$

versus wave vector $\mathbf{Q} = (Q_x, Q_y)$ from our DMRG data where $\mathbf{0} = (L/2, 1)$. First we consider a coarse grained set of $J_{1,2}$. The results are shown in Fig. A.5. As labeled in panel (a) four values of $J_{1,2}$ are taken from regions where commensurate correlations are to be expected and two out of the vicinity of the first order transition as observed in DMRG, Fig. A.1(b, inset) and SBMFT Fig. A.2. Since the transverse momentum space of the tube is confined to $Q_y = (0,1,2,3)\pi/2$ there are four $S(Q_x, Q_y)$-lines for each value of $J_{1,2}$.

Fig. A.5(a) exhibits a flat structure for all Q_y modes vs. Q_x, which reflects the decoupling of the plaquettes. Moreover $S(\mathbf{Q})$ is maximum at $Q_{y,max} = \pi$ consistent with the singlet

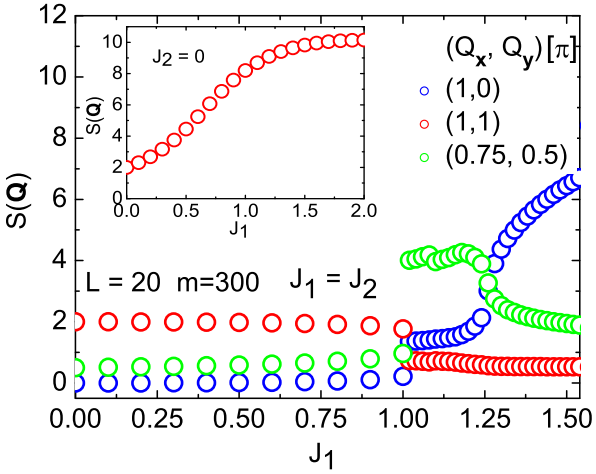

Figure A.6.: $S(\mathbf{Q})$ from DMRG, L=30, m=300, and OBC versus $J_1 = J_2$ at $\mathbf{Q} = (\pi, 0)$ (blue circles), (π, π) (red circles) and for the incommensurate $\mathbf{Q}_{max} = \pm(3\pi/4, \pi/2)$ (green circles). Inset: $S(\pi, \pi)$ versus J_1 at $J_2 = 0$.

ground state on the decoupled plaquettes. Figs. A.5(d,e,f) show maxima in $S(\mathbf{Q})$ at $\mathbf{Q}_{max} = (\pi, 0)$, $(0, \pi)$, and (π, π) respectively. This is consistent with SBMFT in Fig. A.2 and also with the classical phase diagram in Fig. 5.2. The small oscillations around the maxima are finite size effects. On the *finite* system used for the DMRG calculations, the amplitude of the structure factor remains finite at $\mathbf{Q}_{max}$. From the analysis up to now, we expect no LRO on the quantum FFST, i.e. a finite value of $S(\mathbf{Q}_{max})$ for $L \to \infty$. A proof of the latter would require finite size scaling analysis, which is beyond our computational reach.

Figs. A.5(b,c) describe $J_{1,2}$ values shortly below and above the first order transition of Fig. A.1(b, inset), along the line of maximum frustration. Panel (b) contains a small modulation in all modes, although the plaquette phase is still evident from $Q_{y,max} = \pi$. Panel (c) however shows two-symmetric maxima at *incommensurate* vectors with $\mathbf{Q}_{max} = (3\pi/4, \pi/2)$, $(5\pi/4, 3\pi/2)$. While the y-component of these pitch vectors are set by the transverse quantization of the momentum space, the x-components are set by the quantum correlations in the FFST. Very remarkably, these x-components are, up to our numerical precision (10^{-4}), identical to the corresponding classical pitch-vectors, listed in the enumeration point 4) in section 5.1.

Next, we discuss the DMRG structure factor in a finer grained analysis of the $J_{1,2}$ plane,

along the diagonal line of maximum frustration. We have observed the occurrence of $Q_{y,max} = \pi$ with flat Q_x dependence, characteristic of the plaquette phase, for $J_1 = J_2 \lesssim 0.7$ and $\mathbf{Q}_{max} = (\pi, \pi)$), still with very flat Q_x dependence, for $0.8 \lesssim J_1 = J_2 \lesssim 1$ (cf. Figs. A.1(a,b)). We also find $\mathbf{Q}_{max} = (\pi, 0)$, signaling a commensurate classical-like $(\pi, 0)$ phase for $J_1 = J_2 \gtrsim 1.3$ (cf. Fig. A.1(d)). An incommensurate phase is observed for $1 \lesssim J_1 = J_2 \lesssim 1.3$, with $\mathbf{Q}_{max} = (3\pi/4, \pi/2), (5\pi/4, 3\pi/2)$.

In order to describe the extent of such incommensurate region, we show in Fig. A.6, $S(\mathbf{Q})$ for representative momenta $\mathbf{Q} = (\pi, \pi)$, $(3\pi/4, \pi/2), (\pi, 0)$ in the range $J_1 = J_2 \in [0, 1.5]$. Clearly, $S(\pi, \pi)$ is maximum and shows only a small variation in the range $J_1 = J_2 \in [0, 1]$ (plaquette phase). At $J_1 = J_2 = 1$, the structure factor is discontinuous. Following that, and in a small window of $1 \lesssim J_1 = J_2 \lesssim 1.25$, $S(\mathbf{Q})$ is maximum at the incommensurate wave vector. In the vicinity of $J_1 = J_2 \approx 1.25$, there is a crossover from incommensurate to commensurate $(\pi, 0)$ correlations. These results can be interpreted in terms of a small window of an incommensurate phase with a weak first order transition into the $(\pi, 0)$-phase and a kink in the energy which is too small to be detected from the DMRG calculations in Fig. A.1.

For reference, the inset in Fig. A.6 reports $S(\pi, \pi)$ along the J_1-axis, i.e. $J_2 = 0$, where the structure factor is maximum for any $J_1 > 0$. This plot shows a continuous increase and no signs of phase transitions in this part of parameters space. An identical observation applies to $S(0, \pi)$ along the J_2-axis, i.e. $J_1 = 0$, for all $J_2 > 0$. This is consistent with the plaquette phase being adiabatically connected with the limit of decoupled chains.

While the discussion in Fig. A.6 is confined to the line of maximum frustration, we have performed similar analysis along additional lines in the $J_{1,2}$ plane. These agree with a plaquette phase in strips of width one, both, along the J_1-, and J_2-axis, as in Fig. A.2, up to values of $J_{1,2} \approx 5$. This extends the range obtained from the kink in the ground state energy in Fig. A.1 and Ref. [33]. Moreover, incommensurate correlations are observed beyond these strips, with $\mathbf{Q}_{max}$ slightly renormalized by quantum fluctuations with respect to the classical spiral pitch-vectors in the enumeration point 4) in section 5.1. Unfortunately, the width of the incommensurate region decreases rapidly off from the line of maximum frustration and cannot be determined accurately enough.

To summarize, static structure factor calculations suggest that at least close to line of maximum frustration, the plaquette phase-strips undergo a first order transition into an incommensurate phase, the extent of which is strongly decreased by quantum fluctuations with respect to the classical spiral phase. The transition between the incommensurate and the $(\pi, 0)$ phase appears to be very weakly first order.

Bibliography

[1] L. Faddeev and L. Takhtajan, Physics Letters A **85**, 375 (1981).

[2] D. A. Tennant, T. G. Perring, and R. A. Cowley, Physical Review Letters **70**, 4003 (1993).

[3] D. A. Tennant, R. A. Cowley, and A. M. Tsvelik, Physical Review B **52**, 13368 (1995).

[4] W. J. L. Buyers *et al.*, Physical Review Letters **56**, 371 (1986).

[5] R. Morra, W. Buyers, R. Armstrong, and K. Hirakawa, Physical Review B **38**, 543 (1988).

[6] F. D. M. Haldane, Phys. Rev. Lett. **50**, 1153 (1983).

[7] J. Hubbard, Proceedings of the Royal Society A: Mathematical, Physical and Engineering Sciences **276**, 238 (1963).

[8] W. Heisenberg, Zeitschrift für Physik **49**, 619 (1928).

[9] S. Satija *et al.*, Physical Review B **21**, 2001 (1980).

[10] A. Keren *et al.*, Physical Review B **48**, 12926 (1993).

[11] J. P. Renard *et al.*, Europhysics Letters (EPL) **3**, 945 (1987).

[12] V. Garlea *et al.*, Physical Review Letters **100**, 037206 (2008).

[13] Z. Hiroi, M. Azuma, M. Takano, and Y. Bando, Journal of Solid State Chemistry **95**, 230 (1991).

[14] H. Bethe, Z. Phys. **71**, 205 (1931).

[15] S.-i. Tomonaga, Progress of Theoretical Physics **5**, 544 (1950).

[16] J. M. Luttinger, Journal of Mathematical Physics **4**, 1154 (1963).

[17] F. D. M. Haldane, Journal of Physics C: Solid State Physics **14**, 2585 (1981).

[18] V. E. Korepin and F. H. L. Essler, *Exactly Solvable Models of Strongly Correlated Electrons* (World Scientific, 1994).

[19] E. Fradkin, *Field Theories of Condensed Matter Physics* (Cambridge University Press, 2013).

[20] M. P. Gelfand and R. R. P. Singh, Advances in Physics **49**, 93 (2000).

[21] S. R. White, Physical Review Letters **69**, 2863 (1992).

[22] O. F. Syljuasen and A. W. Sandvik, Physical Review E **66**, 046701 (2002).

[23] H. G. Evertz, Advances in Physics **52**, 1 (2003).

[24] T. Giamarchi, *Quantum Physicsin One Dimension* (Oxford University Press, 2003).

[25] R. K. B. J. Skilling, Mon. Not. R. Astrn. Soc. **211**, 111 (1984).

[26] J. Sirker, R. G. Pereira, and I. Affleck, Physical Review Letters **103**, 216602 (2009).

[27] J. Sirker, R. G. Pereira, and I. Affleck, Physical Review B **83**, 035115 (2011).

[28] S. Grossjohann and W. Brenig, Physical Review B **81**, 012404 (2010).

[29] S. White and D. Huse, Physical Review B **48**, 3844 (1993).

[30] S. White and I. Affleck, Phys. Rev. B **77**, 134437 (2008).

[31] A. Zheludev *et al.*, Physical Review Letters **100**, 157204 (2008).

[32] V. Garlea *et al.*, Physical Review B **79**, 060404 (2009).

[33] M. Arlego and W. Brenig, Physical Review B **84**, 134426 (2011).

[34] M. Arlego *et al.*, Physical Review B **87**, 014412 (2013).

[35] B. Frischmuth, B. Ammon, and M. Troyer, Physical Review B **54**, R3714 (1996).

[36] V. Bisogni and G. Jochen, RIXS data.

[37] D. C. Handscomb, Mathematical Proceedings of the Cambridge Philosophical Society **58**, 594 (1962).

[38] A. Sandvik and J. Kurkijärvi, Physical Review B **43**, 5950 (1991).

[39] A. Sandvik, Physical Review B **59**, R14157 (1999).

[40] A. W. Sandvik, Phys. Rev. B **56**, 11678 (1997).

[41] M. E. J. Newman and G. T. Barkema, *Monte Carlo Methods in Statistical Physics* (Clarendon Press, 1999).

[42] K. Binder and D. W. Heermann, *Monte Carlo simulation in statistical physics*, 5th ed. (Springer-verlag Berlin Heidelberg, 2010).

[43] N. Metropolis *et al.*, The Journal of Chemical Physics **21**, 1087 (1953).

[44] S. Chandrasekharan and U.-J. Wiese, Physical Review Letters **83**, 3116 (1999).

[45] P. Henelius and A. Sandvik, Physical Review B **62**, 1102 (2000).

[46] J. Wojtkiewicz, Physical Review B **75**, 174421 (2007).

[47] B. Ammon *et al.*, Physical Review B **58**, 4304 (1998).

[48] A. W. Sandvik, Journal of Physics A: Mathematical and General **25**, 3667 (1992).

[49] O. A. Starykh and R. R. P. Singh, Physical Review B **55**, 14953 (1997).

[50] S. Grossjohann, Ph.D. thesis, TU Braunschweig, 2010.

[51] B. Willenberg, Master thesis, TU Braunschweig, 2009.

[52] T. W. Anderson, *The statistical analysis of time series* (Wiley, 1971).

[53] M. B. Priestley, *Spectral analysis and time series* (Academic Press, 1983).

[54] W. Janke, in *Statistical Analysis of Simulations: Data Correlations and Error Estimation*, edited by J. Grotendorst, D. Marx, and A. Muramatsu (Rolduc Conference Centre, 2002).

[55] R. G. Miller, Biometrika **61**, 1 (1974).

[56] B. Efron, *The Jackknife, the Bootstrap, and Other Resampling Plans* (SIAM, 1982).

[57] H. Schüttler and D. Scalapino, Physical Review Letters **55**, 1204 (1985).

[58] H. Schüttler and D. Scalapino, Physical Review B **34**, 4744 (1986).

[59] H. J. Vidberg and J. W. Serene, Journal of Low Temperature Physics **29**, 179 (1977).

[60] G. Wahba, SIAM Journal on Numerical Analysis **14**, 651 (1977).

[61] S. White, D. Scalapino, R. Sugar, and N. Bickers, Physical Review Letters **63**, 1523 (1989).

[62] M. Jarrell and O. Biham, Physical Review Letters **63**, 2504 (1989).

[63] J. Skilling, *Maximum Entropy and Bayesian Methods* (Kluwer Academic, 1989).

[64] M. Jarrell and J. Gubernatis, Physics Reports **269**, 133 (1996).

[65] J. S. Bryan and R. K., Mon. Not. R. astr. **211**, 111 (1984).

[66] S. Gull and G. Daniell, Nature **272**, 686 (1978).

[67] J. Gubernatis, M. Jarrell, R. Silver, and D. Sivia, Physical Review B **44**, 6011 (1991).

[68] S. H. Jeffreys, *The Theory of Probability* (Oxford University Press, 1998).

[69] R. K. Bryan, European Biophysics Journal **18**, 165 (1990).

[70] S. Meshkov and D. Berkov, International Journal of Modern Physics C **05**, 987 (1994).

[71] H. B. Flensberg and K., *Introduction to Many-body Quantum Theory In Condensed Mathher Physics* (Oxford University Press, 2004).

[72] G. D. Mahan, *Many-Particle Physics* (Springer, 2000).

[73] X. Zotos and P. Prelovšek, in *Strong Interactions in Low Dimensions*, edited by D. Baeriswyl and L. Degiorigi (Kluwer Academic Publishers, 2004).

[74] J. Luttinger, Physical Review **135**, A1505 (1964).

[75] X. Zotos and P. Prelovšek, Physical Review B **53**, 983 (1996).

[76] F. Naef and X. Zotos, Journal of Physics: Condensed Matter **10**, L183 (1998).

[77] B. S. Shastry, Physical Review Letters **65**, 243 (1990).

[78] P. Maldague, Physical Review B **16**, 2437 (1977).

[79] D. Baeriswyl, C. Gros, and T. Rice, Physical Review B **35**, 8391 (1987).

[80] W. Kohn, Physical Review **133**, A171 (1964).

[81] H. Castella, X. Zotos, and P. Prelovšek, Physical Review Letters **74**, 972 (1995).

[82] T. Giamarchi and B. Shastry, Physical Review B **51**, 10915 (1995).

[83] P. Mazur, Physica **43**, 533 (1969).

[84] M. Suzuki, Physica **51**, 277 (1971).

[85] O. Babelon, D. Bernard, and M. Talon, *Introduction to classical integrable systems* (Cambridge University Press, 1998).

[86] J. Benz, T. Fukui, A. Klümper, and C. Scheeren, Journal of the Physical Society of Japan **74**, 181 (2005).

[87] F. Heidrich-Meisner, A. Honecker, D. Cabra, and W. Brenig, Physical Review B **68**, 134436 (2003).

[88] F. Heidrich-Meisner, A. Honecker, and W. Brenig, Physical Review B **71**, 184415 (2005).

[89] F. Heidrich-Meisner, A. Honecker, and W. Brenig, The European Physical Journal Special Topics **151**, 135 (2007).

[90] M. Žnidarič, Physical Review Letters **106**, 220601 (2011).

[91] K. Fabricius, Physical Review B **57**, 8340 (1998).

[92] B. Narozhny, Physical Review B **54**, 3311 (1996).

[93] B. N. Narozhny and N. Andrei, Physical Review B **58**, R2921 (1998).

[94] N. Peres, P. Sacramento, D. Campbell, and J. Carmelo, Physical Review B **59**, 7382 (1999).

[95] K. Saito, S. Takesue, and S. Miyashita, Physical Review E **54**, 2404 (1996).

[96] P. Jung and A. Rosch, Physical Review B **76**, 245108 (2007).

[97] J. V. Alvarez and C. Gros, Physical Review Letters **88**, 077203 (2002).

[98] J. Alvarez and C. Gros, Physical Review B **66**, 094403 (2002).

[99] D. Heidarian and S. Sorella, Physical Review B **75**, 241104 (2007).

[100] P. Prelovšek, S. Shawish, X. Zotos, and M. Long, Physical Review B **70**, 205129 (2004).

[101] J. Herbrych, R. Steinigeweg, and P. Prelovšek, Physical Review B **86**, 115106 (2012).

[102] T. Prosen and M. Žnidarič, Journal of Statistical Mechanics: Theory and Experiment **2009**, P02035 (2009).

[103] M. Michel, O. Hess, H. Wichterich, and J. Gemmer, Physical Review B **77**, 104303 (2008).

[104] K. R. Thurber, A. W. Hunt, T. Imai, and F. C. Chou, Physical Review Letters **87**, 247202 (2001).

[105] J. Kikuchi *et al.*, Journal of the Physical Society of Japan **70**, 2765 (2001).

[106] F. L. Pratt *et al.*, Physical Review Letters **96**, 247203 (2006).

[107] A. Rosch and N. Andrei, Physical Review Letters **85**, 1092 (2000).

[108] M. Žnidarič, Physical Review Letters **110**, 070602 (2013).

[109] M. Oshikawa and I. Affleck, Physical Review Letters **79**, 2883 (1997).

[110] S. Lukyanov, Nuclear Physics B **522**, 533 (1998).

[111] H. J. Schulz, Physical Review B **34**, 6372 (1986).

[112] R. Steinigeweg, exact diagonalization data, private communication.

[113] X. Zotos, F. Naef, and P. Prelovsek, Physical Review B **55**, 11029 (1997).

[114] N. Bogoliubov, A. Izergin, and V. Korepin, Nuclear Physics B **275**, 687 (1986).

[115] M. Horton and I. Affleck, Phys. Rev. B **60**, 11891 (1999).

[116] R. Steinigeweg and W. Brenig, Physical Review Letters **107**, 250602 (2011).

[117] M. Takahashi, Physical Review Letters **62**, 2313 (1989).

[118] G. Gómez-Santos, Physical Review Letters **63**, 790 (1989).

[119] S. Meshkov, Physical Review B **48**, 6167 (1993).

[120] L. Regnault, Journal of Physics: ... **5**, L677 (1993).

[121] S. Yamamoto and S. Miyashita, Physics Letters A (1997).

[122] I. Affleck and R. Weston, Physical Review B **45**, 4667 (1992).

[123] S. Ma *et al.*, Physical Review Letters **69**, 3571 (1992).

[124] I. Zaliznyak, S.-H. Lee, and S. Petrov, Physical Review Letters **87**, 017202 (2001).

[125] M. Kenzelmann *et al.*, Phys. Rev. Lett. **87**, 017201 (2001).

[126] R. Facility, **50**, (1994).

[127] A. Zheludev, S. Shapiro, and Z. Honda, Physical Review B **69**, 054414 (2004).

[128] M. Sieling *et al.*, Physical Review B **61**, 88 (2000).

[129] S. Zvyagin *et al.*, Physical Review B **77**, 092413 (2008).

[130] M. Chiba *et al.*, Physical Review B **44**, 2838 (1991).

[131] M. Takigawa *et al.*, Physical Review Letters **76**, 2173 (1996).

[132] N. Haga and S.-i. Suga, Journal of the Physics Society Japan **69**, 2431 (2000).

[133] A. Sologubenko *et al.*, Physical Review Letters **100**, 137202 (2008).

[134] M. den Nijs and K. Rommelse, Physical Review B **40**, 4709 (1989).

[135] T. Kennedy and H. Tasaki, Communications in mathematical physics **484**, 431 (1992).

[136] W. Chen, K. Hida, and B. Sanctuary, Physical Review B **67**, 104401 (2003).

[137] C. Degli Esposti Boschi, E. Ercolessi, F. Ortolani, and M. Roncaglia, The European Physical Journal B - Condensed Matter **35**, 465 (2003).

[138] Y.-C. Tzeng and M.-F. Yang, Physical Review A **77**, 012311 (2008).

[139] A. F. Albuquerque, C. Hamer, and J. Oitmaa, Physical Review B **79**, 054412 (2009).

[140] S. Hu, B. Normand, X. Wang, and L. Yu, Physical Review B **84**, 220402 (2011).

[141] S. C. Furuya *et al.*, Physical Review B **84**, 180410 (2011).

[142] I. Affleck, Physical Review B **43**, 3215 (1991).

[143] O. Golinelli, T. Jolicoeur, and R. Lacaze, Physical Review B **45**, 9798 (1992).

[144] R. Konik and P. Fendley, Physical Review B **66**, 144416 (2002).

[145] M. Gell-Mann and M. Lévy, Il Nuovo Cimento **16**, 705 (1960).

[146] A. M. Polyakov, *Gauge Fields ans Strings* (Harwood Academic publishers, 1987).

[147] U. Schollwöck, J. Richter, D. J. J. Farnell, and R. F. Bishop, *Quantum Magnetism*, Vol. 645 of *Lecture Notes in Physics* (Springer, 2004).

[148] H.-J. Mikeska and A. K. Kolezhuk, *Quantum magnetism* (PUBLISHER, 2004), Vol. 83, pp. 1–83.

[149] A. Belavin, A. Polyakov, A. Schwartz, and Y. Tyupkin, Physics Letters B **59**, 85 (1975).

[150] E. Brézin and J. Zinn-Justin, Physical Review B **14**, 3110 (1976).

[151] E. Lieb, T. Schultz, and D. Mattis, Annals of Physics **16**, 407 (1961).

[152] I. Affleck, Journal of Physics: Condensed Matter **1**, 3047 (1989).

[153] I. Affleck, T. Kennedy, E. H. Lieb, and H. Tasaki, Physical Review Letters **59**, 799 (1987).

[154] I. Affleck, T. Kennedy, E. H. Lieb, and H. Tasaki, Communications in Mathematical Physics **115**, 477 (1988).

[155] T. Kennedy, Journal of Physics: Condensed Matter **2**, 5737 (1990).

[156] S. R. White, Physical Review Letters **69**, 2863 (1992).

[157] M. Fannes, B. Nachtergaele, and R. F. Werner, Europhysics Letters (EPL) **10**, 633 (1989).

[158] A. Klumper, A. Schadschneider, and J. Zittartz, Journal of Physics A: Mathematical and General **24**, L955 (1991).

[159] A. Kolezhuk and U. Schollwöck, Physical Review B **65**, 100401 (2002).

[160] D. P. Arovas and A. Auerbach, Physical Review Letters **60**, 531 (1988).

[161] U. Neugebauer and H. J. Mikeska, Zeitschrift für Physik B Condensed Matter **99**, 151 (1995).

[162] M. Steiner *et al.*, Journal of Applied Physics **61**, 3953 (1987).

[163] H. Arugakatori, Y. Ajiro, T. Asano, and T. Goto, Journal of the Physical Society of Japan **64**, 3038 (1995).

[164] M. Monfort, J. Ribas, X. Solans, and M. Font-Bardía, Inorganic Chemistry **35**, 7633 (1996).

[165] Z. Honda, H. Asakawa, and K. Katsumata, Physical Review Letters **81**, 2566 (1998).

[166] A. Zheludev *et al.*, Physical Review B **63**, 104410 (2001).

[167] Z. Honda *et al.*, Journal of Physics: Condensed Matter **9**, L83 (1997).

[168] A. Zheludev *et al.*, Europhysics Letters (EPL) **55**, 868 (2001).

[169] J. Renard, V. Gadet, L. Regnault, and M. Verdaguer, Journal of Magnetism and Magnetic Materials **90-91**, 213 (1990).

[170] H. Mutka *et al.*, Physical Review Letters **67**, 497 (1991).

[171] J. Darriet and L. Regnault, Solid State Communications **86**, 409 (1993).

[172] Y. Ajiro *et al.*, Physical Review Letters **63**, 1424 (1989).

[173] K. Katsumata *et al.*, Physical Review Letters **63**, 86 (1989).

[174] H. Tsujii *et al.*, Physical Review B **71**, 014426 (2005).

[175] T. Kobayashi *et al.*, Journal of the Physical Society of Japan **70**, 813 (2001).

[176] F. Anfuso and A. Rosch, Physical Review B **76**, 085124 (2007).

[177] Z.-C. Gu and X.-G. Wen, Physical Review B **80**, 155131 (2009).

[178] F. Pollmann, A. M. Turner, E. Berg, and M. Oshikawa, Physical Review B **81**, 064439 (2010).

[179] M. N. Barber, *Phase Transitions and Critical Phenomena* (Academic Press, 1983).

[180] Y. Kim, M. Greven, U.-J. Wiese, and R. Birgeneau, The European Physical Journal B **4**, 291 (1998).

[181] D. Charrier, S. Capponi, M. Oshikawa, and P. Pujol, Physical Review B **82**, 075108 (2010).

[182] Y. Su *et al.*, J. Phys. Soc. Jpn. **81**, 074003 (2012).

[183] M. Karbach, G. Müller, A. Fledderjohann, and K.-H. Mütter, Physical Review B **55**, 12510 (1997).

[184] B. Si-Lakhal and A. Abada, Journal of Physics A: Mathematical and General **37**, 497 (2004).

[185] J.-S. Caux and R. Hagemans, Journal of Statistical Mechanics: Theory and Experiment **2006**, P12013 (2006).

[186] P. Hohenberg and W. Brinkman, Physical Review B **10**, 128 (1974).

[187] O. A. Starykh, A. W. Sandvik, and R. R. P. Singh, Phys. Rev. B **55**, 14953 (1997).

[188] J. Sagi and I. Affleck, Physical review. B, Condensed matter **53**, 9188 (1996).

[189] S. Yamamoto and H. Hori, Journal of the Physics Society Japan **73**, 822 (2004).

[190] Y. Rahnavard and W. Brenig, "Statics and dynamics of anisotropic spin=1 chain in magnetic fields", in preparation.

[191] S. Grossjohann and W. Brenig, Physical Review B **79**, 094409 (2009).

[192] J.-S. Caux, H. Konno, M. Sorrell, and R. Weston, Physical Review Letters **106**, 217203 (2011).

[193] E. Dagotto and T. M. Rice, Science **271**, 618 (1996).

[194] S. White, R. Noack, and D. Scalapino, Physical review letters **73**, 886 (1994).

[195] D. Johnston, J. Johnson, D. Goshorn, and A. Jacobson, Physical Review B **35**, 219 (1987).

[196] M. Azuma *et al.*, Phys. Rev. Lett. **73**, 3463 (1994).

[197] T. Barnes, E. Dagotto, J. Riera, and E. Swanson, Physical Review B **47**, 3196 (1993).

[198] M. Troyer, H. Tsunetsugu, and D. Würtz, Physical Review B **50**, 13515 (1994).

[199] A. Bougourzi, M. Couture, and M. Kacir, Physical review. B **54**, R12669 (1996).

[200] T. Barthel, U. Schollwöck, and S. White, Physical Review B **79**, 245101 (2009).

[201] K. Damle and S. Sachdev, Physical Review B **57**, 8307 (1998).

[202] D. Yang and W. Haxton, Physical Review B **57**, 10603 (1998).

[203] R. Eder, Physical Review B **57**, 12832 (1998).

[204] V. Kotov, O. Sushkov, and R. Eder, Physical Review B **59**, 6266 (1999).

[205] F. Naef and X. Wang, Physical review letters **84**, 1320 (2000).

[206] N. Haga and S.-i. Suga, Physical Review B **66**, 132415 (2002).

[207] C. Knetter and G. S. Uhrig, Eur. Phys. J. B **13**, 209 (2000).

[208] F. Wegner, Annalen der Physik **506**, 77 (1994).

[209] M. Arlego and W. Brenig, The European Physical Journal B **53**, 193 (2006).

[210] M. Arlego and W. Brenig, Physical Review B **78**, 224415 (2008).

[211] M. Arlego and W. Brenig, Physical Review B **75**, 024409 (2007).

[212] W. Brenig and M. Grzeschik, Physical Review B **69**, 064420 (2004).

[213] W. Brenig and A. Honecker, Physical Review B **65**, 140407 (2002).

[214] W. Brenig, Physical Review B **67**, 064402 (2003).

[215] A. Auerbach, *Interacting Electrons and Quantum Magnetism* (Springer-Verlag, 1994).

[216] A. Auerbach and D. Arovas, Physical Review Letters **61**, 617 (1988).

[217] N. Read and S. Sachdev, Physical Review Letters **66**, 1773 (1991).

[218] S. Sachdev, Physical Review B **45**, 12377 (1992).

[219] H. Ceccatto, C. Gazza, and A. Trumper, Physical Review B **47**, 12329 (1993).

[220] A. E. Trumper, L. O. Manuel, C. J. Gazza, and H. A. Ceccatto, Physical Review Letters **78**, 2216 (1997).

[221] R. Flint and P. Coleman, Physical Review B **79**, 014424 (2009).

[222] A. Albuquerque *et al.*, Journal of Magnetism and Magnetic Materials **310**, 1187 (2007).

[223] J. Schulenburg, Program package SPINPACK.

[224] D. C. Cabra, Physical Review B **58**, 6241 (1998).

[225] E. Kim and J. Sólyom, Physical Review B **60**, 15230 (1999).

Acknowledgements

At the end of a long and intense experience like a PhD in physics, there is normally a long list of people to thank.

My first and special thanks go to my supervisor, Prof. Dr. Wolfram Brenig, for giving me this chance to work in his group, for guiding and motivating me through interesting and challenging projects, and for his extreme patience when answering my not-always-good questions.

I would like to thank other members of our group, Dr. R. Steinigeweg, Dr. R. Darradi, Dr. C. Bartsch, B. Willenberg, and B. Celan, for their very fruitful discussions and constructive criticisms. I'm specially indebted to B. Willenberg and Dr. R. Steinigeweg who have helped and supported me in any stages of my PhD. If there were not the very long discussions I had with B. Willenberg, I wouldn't have been able to understand the very complicated QMC code. I'm grateful to Dr. R. Steinigeweg, not only for sharing his scientific knowledge and smart advices with me but also for his considerable help with non-scientific issues. I thank Prof. Dr. Recher and Prof. Dr. S. Süllow who have kindly accepted to review my PhD thesis. I also thank all members of Prof. Dr. U. Motschmann's group, Prof. Dr. P. Recher's group, and Prof. Dr. G. Zwicknagl's group who have made a very delightful and friendly environment in the institute and during the lunch time and other entertainments. I'm thankful to R. Strassek, our former secretory, M. Baron, our current secretory, and C. Schmidt, the secretory of the institute for mathematical physics, who have helped me a lot in official paper work.

I also thank all members of the LOTHERM group, for hosting the very valuable meetings, workshops, summer schools, seminars and conferences. The group has been a source of friendships as well as good ideas and collaborations. In particular, I would like to thank Dr. C. Hess and A. Mohan who have provided me with the experimental knowledge and data. In addition, I want to express my gratitude to Prof. Dr. Prelovsek and J. Herbrych, for their hospitality during my visit in Ljubljana.

Finally, I thank all my non-physicist friends (too many to be listed here), my lovely wife, my mother, my sister, and my two funny brothers who have been always supportive and helpful. Indeed, without their help and support, I would not have been able to finish my PhD.